NOISE PROPERTIES OF REGULARIZED IMAGE RECONSTRUCTION IN X-RAY COMPUTED TOMOGRAPHY

by

Yingying Zhang-O'Connor

A dissertation submitted in partial fulfillment
of the requirements for the degree of
Doctor of Philosophy
(Electrical Engineering: Systems)
in The University of Michigan
2007

Doctoral Committee:

Professor Jeffrey A. Fessler, Chair
Professor Mitchell M. Goodsitt
Professor Alfred O. Hero III
Professor David C. Munson Jr.
Research Professor Neal H. Clinthorne

To my parents, Yu Zhang and Yuping Gao, and my husband, Stephen O'Connor.

ACKNOWLEDGEMENTS

This thesis is the end-of-journey harvest of my five and half years of hard work whereby I have been inspired and encouraged by many people. It is my greatest pleasure to express my deepest and sincerest gratitude for all of them.

This thesis would not exist without my advisor, Professor Jeffrey A. Fessler. His enlightening guidance, colossal support and sincere friendship helped me from day one and throughout my graduate study. I would also like to express my gratitude to Professor Neal H. Clinthorne, Professor Mitchell M. Goodsitt, Professor Alfred O. Hero, and Professor David C. Munson for their expertise and valuable feedbacks on this work. I give special thanks to Professor Anthony W. England for his understanding and assistance in my transition of research fields. I further present my gratefulness to the colleagues at University of Michigan, including Sangtae Ahn, Idris Elbakri, Anastasia Yendiki, Matthew Jacobson, Rongping Zeng, Somesh Srivastava, Hugo Shi, Dan Ruan, Eran Bashan, SeYoung Chun, Ted Way and Kim Khalsa. I acknowledge Dr. Jiang Hsieh, Dr. Bruno DeMan and Dr. Samit Basu from GE for the access to the real data and their thoughful discussions.

I'm deeply indebted to my parents, Yu Zhang and Yuping Gao, whose unconditional love and support has accompanied me throughout my life. I owe my thanks to my brother, Hao Zhang, who helps me fulfill my obligation to take good care of my parents when I am far from home. My dear husband, Stephen O'Connor has been, always, the source of strength, love and confidence. I owe my deepest appreciation to him. Finally, but not least, I would like to express my special thanks to my parents-in-law, Dermot and Maureen

O’Connor, who treat me as their own child and bring me the warmth in this far-away land.

TABLE OF CONTENTS

CHAPTER

LIST OF FIGURES

Figure

LIST OF TABLES

Table

ABSTRACT

NOISE PROPERTIES OF REGULARIZED IMAGE RECONSTRUCTION IN X-RAY COMPUTED TOMOGRAPHY

by

Yingying Zhang-O'Connor

Chair: Jeffrey A. Fessler

X-ray computed tomography (CT) has routine use in medical diagnosis. Technology advancements enable further clinical applications, such as cardiac imaging and lung cancer screening. It also has use in industrial applications.

The spatial resolution and noise properties of image reconstruction methods are important for imaging system design, reconstruction method comparisons and reconstruction parameter selection. Current reconstruction methods fall into two main categories: analytical and iterative methods. The representative of the former category is filtered back projection (FBP) or convolution back projection (CBP). The iterative methods can be further divided into algebraic and statistical methods. The spatial resolution and noise properties of analytical methods are well studied and understood. The statistical reconstruction methods have the potential to offer improved image quality and better bias-variance performance. They are based on models for measurement statistics and physics, and can easily incorporate the prior information, the system geometry and the detector response. They can also model Compton scattering and the polyenergetic spectrum of the X-ray source. The main disadvantages of the statistical reconstruction methods are the longer computation time of iterative algorithms that is usually required to minimize certain cost functions, and the lack of insights into the resolution and noise properties of the reconstructed images.

This thesis addresses these two concerns of statistical reconstruction methods by developing the fast non-uniform FFT (NUFFT)-based forward and back-projectors and by deriving an analytical approach to study the noise properties of the statistically reconstructed images. The overall computation for the NUFFT-based 2D fan-beam forward projector is akin to previous hierarchical methods, and is about two times faster than the distance-driven (DD) forward projector while providing comparable accuracy. The proposed analytical noise variance predictions for the 2D fan-beam geometry provide accuracy comparable to FFT-based predictions and agree well with empirical variances in fan-beam CT, but require much less computation than the traditional FFT method. An extension to 3D cylindrical CT is also developed.

CHAPTER 1

Introduction

The tasks of medical imaging can be grouped into two generic categories: classification and estimation. Classification usually involves a decision-making process, determining from which class of underlying objects the data is derived. In the case of estimation tasks, quantification of a variety of parameters is performed based on the measurements to describe the objects. Image reconstruction is a common example of an estimation task: estimating the spatial distribution of a certain characteristic of the object. For example, the distribution of attenuation in transmission tomography and the distribution of the radioisotopes in emission tomography are the parameters of interest to reconstruct.

Objective assessment of image quality is task-specific. In the context of image reconstruction, the task can be performed by different estimators, such as a Bayesian estimator, an algebraic estimator or a maximum-likelihood (ML) estimator. Bias and variance are two common measures to assess estimator performance. The quality of reconstructed images is often characterized by the spatial resolution and noise. In this dissertation, we focus on tomographic imaging systems, particular transmission computed tomography (TCT).

The conventional method to reconstruct the attenuation images from computed tomography (CT) measurements is filtered back projection (FBP) or convolution back projection (CBP). FBP reconstruction method is a deterministic method based on the properties of the Radon transform and the central slice theorem. Therefore FBP method assumes an ideal realization of tomographic imaging. The effect of noise is often reduced by a spatial-invariant filter. Another class of methods that partially account for the data statistics are somewhat "semi-statistical", either using a spatial-variant filter to smooth the projection data [3, 29, 82], or first statistically "restoring" the sinogram [10, 46, 58, 95] before applying FBP. The "fully" statistical reconstruction methods, on the other hand, are based on models for measurement statistics and physics. They can easily incorporate the prior information, the system geometry and the detector response, and model scattering and energy spectrum of the X-ray source. Therefore, they have the potential to offer improved image quality, better bias-variance performance and reduced dose. Of all the statistical reconstruction methods, maximum likelihood reconstruction is most common. Because image reconstruction is an ill-posed problem, maximum likelihood reconstruction leads to very noisy images that are unacceptable. Noise reduction can be achieved by augmenting the original optimization problem with a regularizer. Penalized-likelihood (PL) reconstruction adds a roughness penalty to the negative log likelihood. Basically these penalty functionals can be viewed as expressing prior information about the underlying object. Usually an iterative algorithm is needed to minimize PL cost functions. The resolution and noise properties are influenced by both the data collection method and reconstruction parameter selection.

One of the main disadvantages of statistical reconstruction methods is the longer computation time of iterative algorithms that usually are required to minimize the cost function. Most iterative algorithms require one forward projection and one back-projection for each iteration. The primary computation burden of iterative image reconstruction methods is these forward and back-projections. All projection/back-projection methods are approximations to the real physical models. There are at least five practical types of backprojection approaches (including ours): rotation-based, pixel-driven, ray-driven, distance-driven and Fourier-based. We will discuss these approaches in Chapter 3.

The statistical properties of the reconstructed images have not been well studied previously. Typically, the variance or standard deviation images are estimated empirically. This requires multiple realizations of image reconstruction and therefore is impractical due to the long computation time. The choices of regularization parameters that control the trade-off between the data-fitting and the image smoothness are based mainly on trial and error. Accurate prediction of variance maps for iteratively reconstructed images can be useful for algorithm analysis and for the design of regularization methods. The existing variance prediction methods can be divided into iteration based and estimator based methods. The iteration-based variance predictions are studied in *e.g.*, [15,98] as a function of the iteration number for the maximum-likelihood expectation maximization (MLEM) algorithm that is based on a “stopping rule” to terminate the iterations before convergence. The estimator-based variance predictions are the properties of the convergent images, and independent of the particular algorithm and iterations, [32,78,91]. We focus on the latter approach because the predictions depend only on the selected cost function, not on the particular algorithm.

1.1 Contributions and Outline

The work in this dissertation has been focused on accelerating the forward and back-projection and studying noise properties associated with statistical image reconstruction in X-ray transmission CT:

1. Chapter 3 develops a fast Fourier-based projection and back-projection pair in 2D fan-beam CT.

   (a) Because there is no suitable Fourier slice theorem in divergent-beam geometry and it is not evident how to use for forward projection a recent extension [21] that is suitable for analytical reconstruction, we use the usual parallel-beam Fourier slice theorem and interpolate the samples into the fan-beam coordinates. To ensure good accuracy and computation efficiency, we use a min-max optimized nonuniform fast Fourier transform (NUFFT) approach for the radial "interpolation". The backprojection is the adjoint operation of the forward projection.

   (b) Because Fourier methods are efficient only for shift-invariant detector response models, we approximate the detector response by the effective width at the center of the field of view when the variation in detector response over the field of view is often fairly modest.

2. The proposed NUFFT-based fan-beam forward and backprojectors work generally for arbitrary fan-beam sampling patterns. For the usual 3rd-generation CT fan-beam geometry, the overall computation for the NUFFT-based fan-beam forward projector is $O(N^2 \log N)$, akin to previous hierarchical methods [16], whereas most space-based forward projectors require $O(N^3)$ operations. Therefore, the NUFFT-based forward and backprojectors are much faster than the line or beam-based space approaches. They are comparable to the distance-driven projectors for small images and are about 2 to 4 times faster for larger images.

3. Chapter 4 proposes an analytical variance prediction approach that can compute the variance map efficiently and accurately. The derivation of the closed-form approximations provides insight into the noise properties of the quadratically penalized likelihood (QPL) reconstructed images in 2D fan-beam CT:

   (a) Neglecting the depth-dependent detector blur, we start with the continuous-space counterpart of the existing matrix-based covariance approximation [32], and derive a "pure" analytical local frequency response of Gram operator. This step helps us understand the issue intuitively.

   (b) By using discrete-space Fourier transform (DSFT) and Parseval's theorem, we are able to bridge the discrete space to continuous space and derive an accurate analytical expression for variance prediction, based on local shift-invariance approximations and local Fourier analysis.

   (c) The simplest of these variance predictions require only a single backprojection and a few minor operations to produce an entire variance map, so they are much faster than the traditional FFT approach that would require a repetitive forward and backprojection for each pixel in the image.

4. Chapter 5 extends the analytical 2D variance prediction methods into a 3D cylindrical cone-beam geometry.

CHAPTER 2

Background

Statistical methods for image reconstruction can be used in different medical imaging modalities, such as magnetic resonance imaging (MRI), positron emission tomography (PET) and digital tomosynthesis. This thesis focuses on tomographic imaging. This chapter briefly reviews the principles in tomographic imaging, particularly X-ray computed tomography (CT).

2.1 Review of Principles of X-Ray Computed Tomography

Conventional tomography depicts a three-dimensional object into a two-dimensional image. The word ”tomography” is derived from the Greek: tomos (slice) and graphia (to write). In transmission tomography, the object to be imaged is the spatial attenuation distribution, while the object to be imaged in emission imaging is the radioactivity distribution. The main limitations of conventional tomography are the blurred overlying structures superimposed on the image and the large x-ray dose to the patient.

The basic idea of today’s tomography was proposed as early as in 1940 by Gabriel Frank [45] and by Allan Cormack independently. Computed tomography was later introduced into clinical practice in early 1970s with first clinically available CT device installed at Atkinson-Morley Hospital in Wimbledon, UK by Godfrey Hounsfield, James Ambrose and Louis Kreel, [8]. Unlike conventional tomography, computed tomography is able to produce images of thin slices of the object with enhanced contrast and reduced structure noise [19]. Tomographic imaging systems collect sets of projections and image reconstruction algorithms recover the original objects from these projections.

2.1.1 Evolution of X-Ray CT Scanners

The typical transmission CT scanner consists of a X-ray tube, a rotation gantry, a table and a detector with one or more detector cells. The types of CT scanners have evolved over five major generations over the past few decades.

Figure 2.1 shows the typical first-generation CT scanner geometry that is characterized by a single X-ray source and a single detector element. It represents the parallel beam geometry. In this scanning geometry, X-ray tube and detector undergo both linear translation and rotation. For a given projection angle, a parallel-beam projection measurement is collected by translating the X-ray tube and the detector along a straight line segment. The X-ray source and detector assembly is translated in a direction that is perpendicular to the X-ray direction and rotated to obtain projection measurements at different view angles.

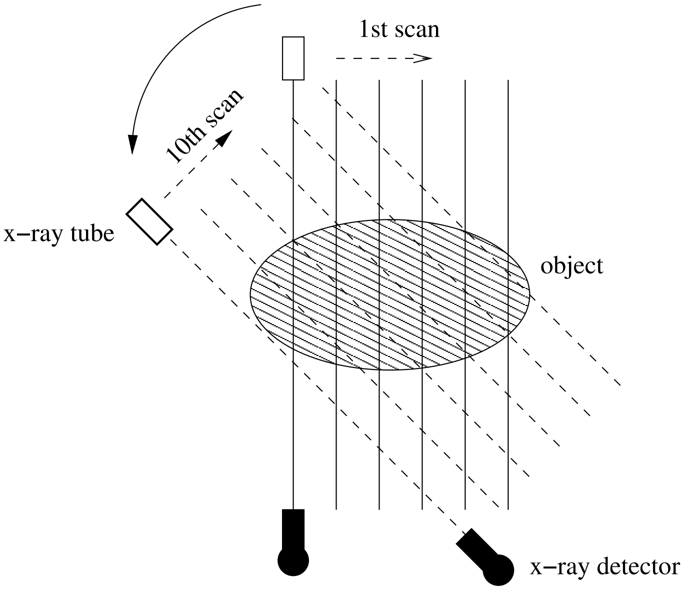

Figure 2.1: First generation CT scanner.

The advantages of this design are simplicity and the ability to accommodate objects of different sizes. The disadvantage is the long scan time.

The second-generation CT scanner is also in a translation-rotation mode with multiple detectors. A fan-beam of radiation is used. By using a small fan-beam angle, projection data at different view angles are collected for each translation. This design helps reduce scanning time by reducing the rotation step. Like the first-generation scanner, the second-generation scanner also has the flexibility to accommodate a wide range of different object sizes. This property enables important applications in some industrial areas.

The third-generation CT scanner utilizes a large number of detector elements and has a much wider fan-beam angle so that ideally X-rays cover the entire object at all times, shown in Figure 2.2. There is no need for translation in this geometry, leading to faster scanning time. The X-ray tube and detectors assembly is operated only in the rotation mode, as shown in Figure 2.2. However, to cover the entire object during the scan, the range of different object sizes is limited by the maximum fan angle and the distance between the X-ray tube and the object. Furthermore, having all detector elements contributing to each view impose more stringent requirements on detector performance than earlier generations.

The fourth-generation scanner is also a rotation-only scanner with a multi-element ring detectors installed around the object. Only the X-ray tube is rotated while the ring detector is stationary.

The mechanism of fifth-generation scanner is very different from that of all the earlier generations discussed above in which the X-ray source and/or the detectors move within the axial plane. The fifth-generation geometry is characterized by multiple X-ray sources arranged into a circular array and an area detector with multiple elements. There is no mechanical motion involved. Instead, the X-ray sources are electronically switched on or off during the data acquisition. A large volume of the object is covered during each scan and a series of 2D projections are collected. An example of this approach is when the X-ray source is produced by a electron-beam tomography (EBT) scanner, [45].

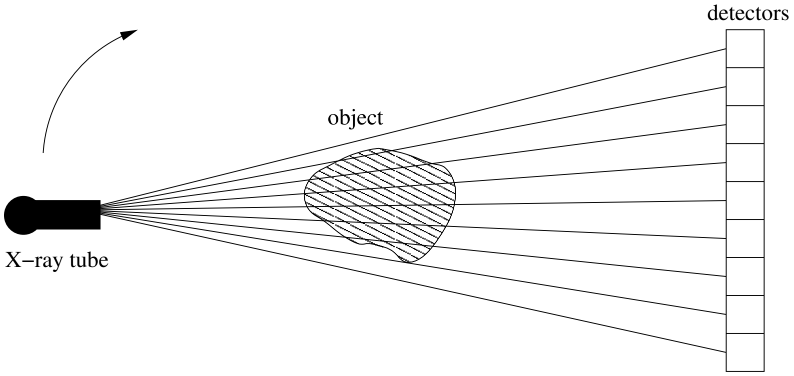

Figure 2.2: Third generation of CT scanner.

During the 1980s, the development of slip ring technology enabled spiral/helical scanning so that fan-beam helical scanning became the standard medical CT mode; see Figure 2.3. The X-ray source rotates continuously in one direction while the table on which the patient is lying translates at a constant speed. The introduction of helical scanning allows even larger body coverage during one single breath hold. Therefore artifacts due to patient motion are reduced. However, there can be artifacts due to missing data in helical acquisition.

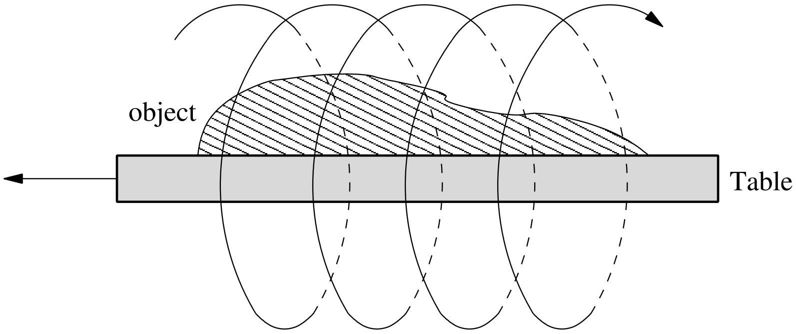

Figure 2.3: Illustration of fan-beam helical CT scan.

Although helical CT improves the volume coverage, higher volume coverage and thinner slices are still demanded in many clinical situations. Multi-slice or multi-detector CT scanners are available now commercially. They incorporate multiple rows of detector rings and acquire multiple slices per rotation. Multi-threaded cone-beam CT scanners with up to three X-ray tubes and corresponding detectors are proposed to improve temporal resolution and reduce cone-beam artifacts for multi-slice CT scanners [57]. Recently researchers developed an inverse-geometry CT (IGCT) system [63,67,83]. In this IGCT architecture, a scanned area source and one or more small detectors are used.

2.1.2 X-Ray CT Measurement Physics

Despite the different geometries mentioned in section 2.1.1, X-ray CT measurement physics are the same for all geometries. For simplicity, our following discussion is restricted to the 2D parallel-beam geometry. The detector measures the X-ray photon flux emerging from the object at different angles, shown in Figure 2.1. Let Y_i denote the measurement for the ith ray of the incident spectrum. For a ray L_i of infinitesimal width, the mean of the projection measurements could be expressed as:

$$E[Y_i] = \int I_i(\mathcal{E})\, \mathrm{e}^{-\int_{L_i} \mu(x,y,\mathcal{E})\, \mathrm{d}\ell}\, \mathrm{d}\mathcal{E} + r_i \tag{2.1}$$

where $i = 1, \ldots, N_d$ and N_d is the number of the rays. $\mu(x, y, \mathcal{E})$ denotes the unknown *spatially- and energy-dependent* attenuation distribution, $\int_{L_i} \cdot \, \mathrm{d}\ell$ is the "line integral" function along line L_i, and $I_i(\mathcal{E})$ incorporates the source spectrum and the detector gain. In reality, the measurements suffer from background signals such as Compton scatter, dark current and noise. The ensemble mean of those effects (for the ith ray) is denoted r_i.

2.1.3 Radon Transform and Fourier Slice Theorem

The CT measurements $\{Y_i\}_{i=1}^{N_d}$ indirectly correspond to the projections of the object's attenuation coefficient $\mu(x, y, \mathcal{E})$. The collection of line integrals is related to the *Radon* *transform*. The Radon transform and its associated Fourier slice theorem play a fundamental role in tomographic imaging systems and deserve an in-depth review.

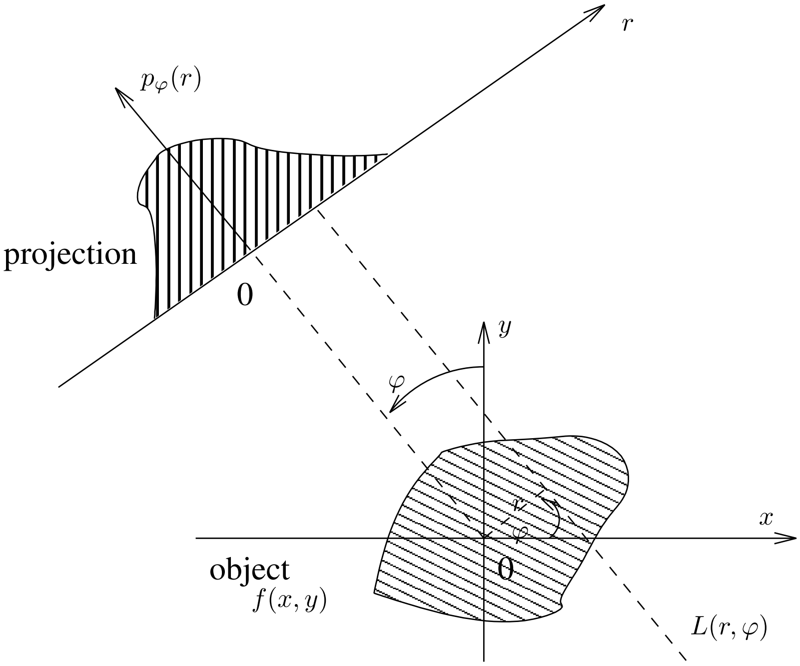

Figure 2.4: 2D function and its Line integrals.

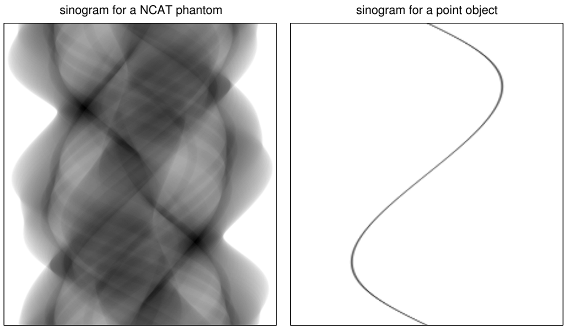

Figure 2.5: Example of sinograms. Left: a sinogram of a NCAT phantom (see Figure 4.5). Right: a sinogram of a point object.

For simplicity, we only consider the 2D case shown in Figure 2.4. The Radon transform relates a 2D image $f(x, y)$ to its line integrals as follows [62]:

$$\begin{aligned}
p_\varphi(r) = (\boldsymbol{\mathcal{P}} f)(r, \varphi) &= \int_{L(r,\varphi)} f(x, y)\, \mathrm{d}\ell \\
&= \int_{-\infty}^{\infty} f(r\cos\varphi - \ell\sin\varphi, r\sin\varphi + \ell\cos\varphi)\, \mathrm{d}\ell \\
&= \int_{-\infty}^{\infty}\int_{-\infty}^{\infty} f(x, y)\delta(x\cos\varphi + y\sin\varphi - r)\, \mathrm{d}x\, \mathrm{d}y \qquad (2.2)
\end{aligned}$$

where $\boldsymbol{\mathcal{P}}$ denotes projection operator, r is the radial distance from the origin and φ is the view angle measured counter-clockwise from the y-axis to the ray direction. The final expression in (2.2) is defined in polar coordinates, (r', ϕ). If the projections $p_\varphi(r)$ from different angles are arranged as an array with one axis of projection angle φ and the other axis of projection bins at the detector (radial distance r), then this 2D function is called sinogram because the sinogram of a point object traces a sinusoid, see Figure 2.5. The goal of image reconstruction is to estimate $f(x, y)$, more particularly $\mu(x, y, \mathcal{E})$ in transmission tomography, from a measured sinogram that is obtained from (noisy) samples of projection data $p_\varphi(r)$. In practice, the analytical reconstruction methods need to estimate $\hat{p}_\varphi(r)$ from measurements $\{Y_i\}$. Statistical reconstruction methods estimate $\mu(x, y, \mathcal{E})$ directly from measurements $\{Y_i\}$.

The *Fourier slice theorem* is also known as the *central section theorem* or *projection slice theorem*. This theorem is the foundation of the tomographic reconstruction method (filtered back-projection) that is widely used in commercial CT scanners. Let $P_\varphi(\rho)$ denote 1D Fourier transform of $p_\varphi(r)$:

$$P_\varphi(\rho) \triangleq \int_{-\infty}^{\infty} p_\varphi(r)\, \mathrm{e}^{-i2\pi\rho r}\, \mathrm{d}r\,.$$

Plugging (2.2) into $P_\varphi(\rho)$ yields the following mathematical statement of the Fourier slice theorem [62]:

$$P_\varphi(\rho) = \int_{-\infty}^{\infty}\int_{-\infty}^{\infty} f(x, y)\, \mathrm{e}^{-i2\pi\rho(x\cos\varphi + y\sin\varphi)}\, \mathrm{d}x\, \mathrm{d}y = F(\rho\cos\varphi, \rho\sin\varphi), \qquad (2.3)$$

where $F(f_x, f_y)$ denotes the 2D Fourier transform of object $f(x, y)$ and $f_x = \rho \cos \varphi, f_y = \rho \sin \varphi$. The 2D Fourier slice theorem (2.3) states that the 1D Fourier transform of the projection at view angle φ is equal to a central slice of the 2D Fourier transform of the object at the same angle.

2.2 Review of Image Reconstruction Methods for X-Ray CT

The overall goal of x-ray CT image reconstruction is to reconstruct the underlying object being imaged from the projection measurements, particularly $\mu(x, y, \mathcal{E})$ from $\{Y_i\}_{i=1}^{N_d}$ in transmission tomography. Image reconstruction methods or algorithms can divided into two main categories: analytical and iterative methods. Most conventional reconstruction methods such as filtered back-projection (FBP) and backprojected-filtration (BPF) are analytical methods. Iterative image reconstruction methods can be further divided into algebraic and statistical methods. Algebraic reconstruction technique (ART) and multiplicative algebraic reconstruction technique (MART) are two examples of algebraic methods [9, 48, 88, 100]. Weighted least squares (WLS) and penalized likelihood (PL) reconstruction are statistical reconstruction methods. Most conventional reconstruction methods ignore the energy spectrum of the beam. In contrast, statistical reconstruction methods can incorporate this energy spectrum into their statistical models. We give a brief review of some of the reconstruction methods in this section.

2.2.1 Direct Fourier Reconstruction and Filtered Back Projection

Both direct Fourier reconstruction (DFR) and filtered back projection (FBP) are analytical image reconstruction methods. Fourier slice theorem and Radon transform are the foundation of these approaches.

Direct Fourier Reconstruction

The direct Fourier reconstruction (DFR) method is very straightforward with the direct application of the Fourier slice theorem (2.3). To reconstruct $f(x, y)$ from the measured projections $p_\varphi(r)$, one performs the following steps depicted in Fig. 2.6:

1. Take 1D Fourier transform of each $p_\varphi(r)$ for each φ to get $P_\varphi(\rho)$. Based on the relationship in (2.3), we have the 2D FT of the object $f(x, y)$ in polar coordinates $F(\rho, \varphi)$.
2. Convert $F(\rho, \varphi)$ in the polar coordinates into $F(f_x, f_y)$ in Cartesian coordinates.
3. Take 2D inverse Fourier transform of $F(f_x, f_y)$ to get $f(x, y)$.

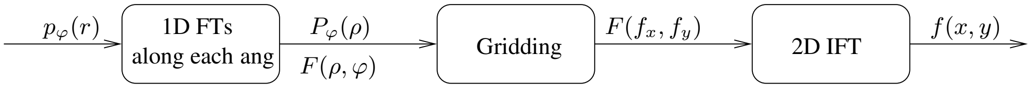

Figure 2.6: Basic steps of direct Fourier reconstruction.

In practice, we process the discretized versions of these continuous functions, as shown in Figure 2.7. Hence the conversion from polar frequency samples to Cartesian frequency samples usually involves Fourier domain interpolation (gridding). Fourier domain interpolation is non-trivial since local interpolation error in frequency domain can cause global artifacts in image domain. Later in Chapter 3, we propose a Fourier-based forward projector that uses a Kaiser-Bessel (KB) interpolator optimized in min-max sense in the gridding step.

Filtered Backprojection (FBP)

Filtered backprojection (FBP) is the most common analytical reconstruction technique that is based on the Radon transform. The basic idea behind this method is to “smear”

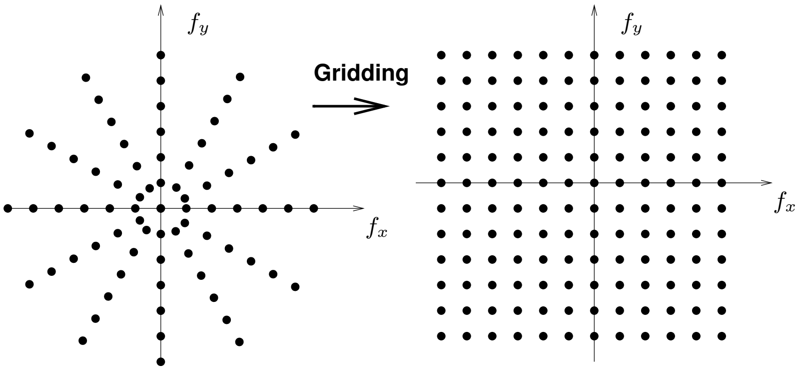

Figure 2.7: Illustration of gridding step that interpolates polar samples of $F(\rho, \varphi)$ of onto Cartesian samples of $F(f_x, f_y)$.

measured sinogram values back into the object space along the corresponding rays:

$$(\boldsymbol{\mathcal{P}}^* p)(x, y) = b(x, y) = \int_0^\pi p_\varphi(x \cos\varphi + y \sin\varphi) \, \mathrm{d}\varphi \,. \tag{2.4}$$

This operator $\boldsymbol{\mathcal{P}}^*$ is called the *backprojection* operator that is the *adjoint* operator of the forward projection operator in equation (2.2). The back-projection operation in (2.4) does not recover the original object $f(x, y)$, unfortunately. A blurred version of the object $b(x, y)$ called laminogram is yielded instead.

In practice we do not measure $p_\varphi(r)$ directly, we need to estimate the projections from the transmitted intensities $\{Y_i\}$. Conventional FBP assumes mono-energetic property of the X-ray spectrum $I_i(\mathcal{E}) = I_i(\mathcal{E}_0)\delta(\mathcal{E} - \mathcal{E}_0)$, then the mean intensities in (2.1) are given by *Beer's law*:

$$E[Y_i] = I_i(\mathcal{E}_0) \, \mathrm{e}^{-\int_{L_i} \mu(x,y,\mathcal{E}_0) \, \mathrm{d}\ell} + r_i. \tag{2.5}$$

The estimated projections can be obtained by taking the logarithm of the measurements:

$$\hat{p}_\varphi(r) \triangleq -\log\left(\frac{Y_i - r_i}{I_i(\mathcal{E}_0)}\right) \approx \int_{L_i} \mu(x, y, \mathcal{E}_0) \, \mathrm{d}\ell \,. \tag{2.6}$$

As mentioned earlier, the resulting laminogram $b(x, y)$ from (2.4) is a blurred version of the object $f(x, y)$. To deblur, we apply a 1D "ramp" filter to each projection at each angle

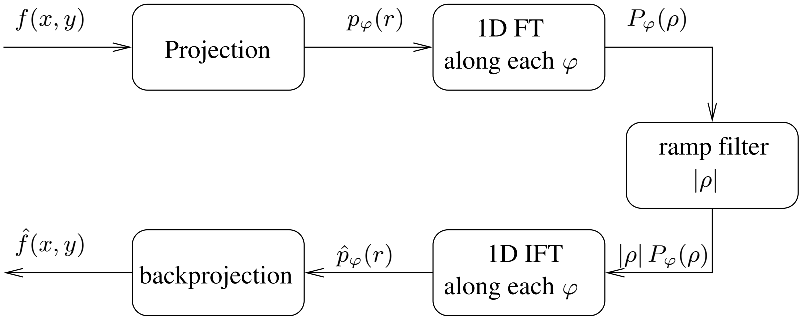

Figure 2.8: Basic steps of FBP reconstruction.

φ. The basic steps of FBP are illustrated in Figure 2.8. In reality, the ideal ramp filter does not really exist and must be set zero beyond certain cutoff frequency. The ramp filter is often apodized with a window function to reduce noise. Since the Fourier transform is implemented using a FFT, the zero-padded sinogram is used to avoid aliasing before 1D Fourier transform at each view and filtering.

Most CT scanners offer various filter options that the operator can select to enhance either soft tissue features or bone details for different clinical applications. For example, GE LightSpeed CT scanner has six types of filters: soft, standard, detail, lung, bone, edge filters [45].

Conventional FBP is based on the monochromaticity assumption of X-ray source. Using the monoenergetic photon source is impractical in diagnostic CT because of the signal-to-noise ratio (SNR) consideration. In reality, the photons emitted from a X-ray tube have a spread of energies. The photon flux density or intensity demonstrates an energy-dependent distribution. The shape of the X-ray spectrum is like a hump topped with several spikes. The continuous spectrum is generated by Bremsstrahlung radiation. The spikes result from the characteristic radiation that is not continuous.

2.2.2 Statistical X-Ray CT Image Reconstruction

Statistical image reconstruction methods are based on measurement statistics and physics models and offer numerous advantages, such as the potential for improved bias-variance performance and providing quantitatively accurate CT values. Conventionally, the X-ray CT measurements are assumed to follow discrete Poisson statistics. However, most CT detectors are energy-integrating, not photon-counting. Due to the polyenergetic property of the X-ray beam, although individual X-ray quanta will lead to Poisson statistics, the overall recorded signal will not be Poisson.

A compound Poisson probability distribution function (pdf) of X-ray CT measurements was derived by Whiting [97] using a moment generating function approach. The pdf is dependent on the X-ray energy quanta, flux level and quantization step size. It has been shown that the compound Poisson likelihood is similar to the ordinary Poisson likelihood for the normal clinical exposures and deviates significantly from the ordinary Poisson likelihood in situations of low counts. The compound Poisson statistics has a complicated likelihood that hinders its direct application in statistical reconstructions. An approximate likelihood was derived by Elbakri *et al.* in [28] using a generalized saddle-point integration method. Their proposed approximate likelihood is more accurate than regular Poisson likelihood. All the models above can be generalized to incorporate additive electronic noise that is usually assumed to be independent of the quanta measurements. Variance predictions in Chapter 4 and Chapter 5 are based on regular Poisson likelihood. However, because variance is second-order statistics, the proposed variance prediction method is applicable to essentially any statistical model.

We focus on the case of normal clinical exposures where regular Poisson statistics is fairly accurate. The measurements are often modeled as the sum of a *Poisson* distribution representing photon-counting statistics (2.1) and a zero-mean normal normal disctribution representing additive electronic noise:

$$Y_i \sim \mathsf{Poisson}\{E[Y_i]\} + \mathsf{N}(0, \sigma_e), \tag{2.7}$$

where σ_e denotes the standard deviation of electronic noise. Because (2.7) does not leads to a tractable likelihood function, an approximate shifted Poisson likelihood function that matches the first and second moments is often used [80, 85, 102]:

$$Y_i + \sigma_e \sim \mathsf{Poisson}\{E[Y_i] + \sigma_e\}\,. \tag{2.8}$$

For simplicity, we ignore the electronic noise and use a *single material* object to demonstrate the ideas behind statistical image reconstruction. We discretize the continuous attenuation function $\mu(x, y, \mathcal{E})$ and parameterize both the spatial and energy dependence. We parameterize the object space as follows:

$$\mu(x, y, \mathcal{E}) = \sum_{j=1}^{p} \mu_j(\mathcal{E}) b_j(x, y), \tag{2.9}$$

where $\mu_j(\mathcal{E})$ denotes the unknown attenuation coefficient in pixel j and $b_j(x, y)$ is the pixel basis function centered at pixel j. We further model the unknown attenuation coefficient as

$$\mu_j(\mathcal{E}) = m(\mathcal{E})\rho_j, \tag{2.10}$$

where $m(\mathcal{E})$ is the mass attenuation coefficient of the single object material (*e.g.*, water) and ρ_j is the (unknown) density of the object in pixel j. Figure 2.9 gives some typical mass attenuation coefficients for various materials.

Substituting (2.9) and (2.10) into (2.1), we obtain the following measurement statistics:

$$Y_i \sim \mathsf{Poisson}\left\{\int I_i(\mathcal{E})\, \mathrm{e}^{-m(\mathcal{E})[\mathbf{A}\boldsymbol{\rho}]_i}\, \mathrm{d}\mathcal{E} + r_i\right\}, \tag{2.11}$$

where $\mathbf{A}$ is the system matrix with entries $a_{ij} = \int_{L_i} b_j(x, y)\, \mathrm{d}\ell$. For a *mono-energetic* X-ray source, Beer's law applies:

$$Y_i \sim \mathsf{Poisson}\{I_i(\mathcal{E}_0)\, \mathrm{e}^{-m(\mathcal{E}_0)[\mathbf{A}\boldsymbol{\rho}]_i} + r_i\} \tag{2.12}$$

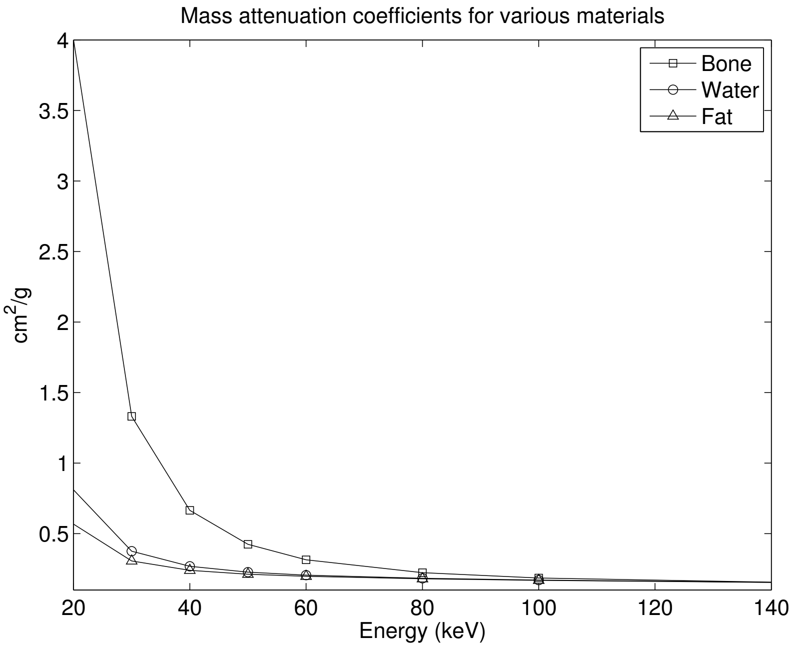

Figure 2.9: Energy-dependent mass attenuation coefficients $m(\mathcal{E})$ for bone, water and fat.

Now the reconstruction goal becomes to estimate $\boldsymbol{\rho} = (\rho_1, \ldots, \rho_p)$ from $\{Y_i\}_{i=1}^{N_d}$. When the assumption that the object consists of one single material is invalid, one must parameterize both the spatial and energy dependency as Clinthorne *et al.* [22, 92, 93] as follows:

$$\mu(x, y, \mathcal{E}) = \sum_{l=1}^{L} m_l(\mathcal{E}) \rho_l(x, y) \tag{2.13}$$

where $m_l(\mathcal{E})$ denotes the energy-dependent mass attenuation coefficients of the lth material and $\rho_l(x, y)$ is the (unknown) spatially-dependent density of the lth material.

Penalized-likelihood (PL) Reconstruction

Based on the statistical distribution of the measurements, we can estimate $\boldsymbol{\rho}$ using *penalized likelihood* estimation. For the mono-energetic model (2.13), the negative log-likelihood has the form

$$\begin{aligned} -L(\boldsymbol{\rho}) &= \sum_{i=1}^{N_d} \left\{ Y_i \log\bigl(\bar{Y}_i(\boldsymbol{\rho})\bigr) - \bar{Y}_i(\boldsymbol{\rho}) \right\} \\ &= \sum_{i=1}^{N_d} \left\{ Y_i \log\left(I_i(\mathcal{E}_0)\, \mathrm{e}^{-m(\mathcal{E}_0)[\mathbf{A}\boldsymbol{\rho}]_i} + r_i \right) - \left(I_i(\mathcal{E}_0)\, \mathrm{e}^{-m(\mathcal{E}_0)[\mathbf{A}\boldsymbol{\rho}]_i} + r_i \right) \right\} \qquad (2.14) \end{aligned}$$

where $\bar{Y}_i(\boldsymbol{\rho}) \triangleq E[Y_i|\boldsymbol{\rho}]$ is the mean of the measurement data along path L_i. For reconstruction, we add a roughness penalty term to the negative likelihood, resulting in the following *penalized-likelihood (PL)* cost function:

$$\Phi(\boldsymbol{\rho}) = -L(\boldsymbol{\rho}) + \alpha R(\boldsymbol{\rho}), \tag{2.15}$$

where the (pairwise) penalty term has the following form

$$R(\boldsymbol{\rho}) = \sum_{j=1}^{p} \sum_{k \in \mathcal{N}_j} \psi(\rho_j - \rho_k),$$

β is a scalar that controls the trade-off of data fit and smoothness of image, $\psi(\cdot)$ is an edge-preserving potential function and $\mathcal{N}_j$ is some neighborhood of pixel j.

Penalized Weighted Least Squares (PWLS) Reconstruction

The Poisson log-likelihood in (2.14) is based on the statistical properties of the tomographic reconstruction problem. However, because Poisson negative log-likelihood (2.14) is non-convex and non-quadratic, the minimization algorithms required can be complex. To simplify, one can apply a second-order Taylor expansion to the Poisson log-likelihood in (2.14), [30, 31]. This quadratic approximation leads to weighted least squares (WLS) likelihood function:

$$-L(\boldsymbol{\rho}) = \sum_{i=1}^{N_d} w_i \frac{1}{2}(-\log(Y_i) - [\mathbf{A}\boldsymbol{\rho}]_i)^2, \tag{2.16}$$

where w_i values are statistical weighting factors that depend on the model for the measurement statistics. For the case of shifted Poisson likelihood, $w_i \approx \frac{(\bar{Y}_i(\boldsymbol{\rho})+\sigma_e-r_i)^2}{\bar{Y}_i(\boldsymbol{\rho})+\sigma_e}$. For the case of regular Poisson likelihood, $w_i \approx \frac{(\bar{Y}_i(\boldsymbol{\rho})-r_i)^2}{\bar{Y}_i(\boldsymbol{\rho})}$. Plugging (2.16) into (2.15) yields penalized weighted least squares (PWLS) cost function. In practice, one often uses simply $w_i = Y_i$.

Iterative algorithms are often applied to minimize (2.15) subject to certain object constraints such as non-negativity:

$$\hat{\boldsymbol{\rho}} = \text{argmin}_{\boldsymbol{\rho} \geq 0} \Phi(\boldsymbol{\rho}). \tag{2.17}$$

To find the minimizer of (2.15), *optimization transfer* methods [2, 25, 27] can be used to replace a complex likelihood as in (2.14) with surrogate cost functions that are simpler and easier to minimize. Optimization transfer methods also ensure the cost function monotonically decreases after each iteration. The resulting algorithm is often a *diagonally-preconditioned gradient* descent method of the following form:

$$\boldsymbol{\rho}^{n+1} = [\boldsymbol{\rho}^n - \mathbf{D}^{-1} \nabla \Phi(\boldsymbol{\rho}^n)]_+ \tag{2.18}$$

where $\nabla \Phi(\boldsymbol{\rho}^n)$ is the gradient of the cost function evaluated at current estimates $\boldsymbol{\rho}^n$, $\mathbf{D}$ is a diagonal matrix and $[\cdot]_+$ enforces non-negativity constraint. The diagonal matrix $\mathbf{D}$, whose nonzero diagonal entries are the second derivatives of the surrogate function, is the key that controls the rate of convergence and monotonicity of the algorithm. The second derivative of the surrogate function has a curvature term that influences the rate of the convergence particularly. We have several different choices of the curvature term:

- Iteration-dependent optimal curvature that keeps step size as large as possible, but requires more computation [1].
- Iteration-independent maximum curvature that ensures the monotonicity of the algorithm, but leads to a slower convergence [1].
- Iteration-independent precomputed curvature that compromises the monotonicity and achieves faster convergence. It is usually used in the ordered-subset version of the algorithm [2].

The column gradient of the cost function in (2.18) has the follow matrix form:

$$\nabla \Phi(\boldsymbol{\rho}) = -\mathbf{A}' \, \boldsymbol{\mathcal{D}}\big(Y_i / \bar{Y}_i(\boldsymbol{\rho}) - 1\big) \, \nabla_{\boldsymbol{\rho}} \bar{\mathbf{Y}}(\boldsymbol{\rho}) + \beta \nabla \boldsymbol{R}. \tag{2.19}$$

From (2.12) and (2.19), we can see that one forward projection and one backprojection are involved in each iteration. Therefore, fast forward and back-projectors are essential in computation time reduction. This is the motivation for our work in next chapter on the development of fast NUFFT-based forward and back projectors.

2.2.3 Beam-Hardening Artifacts Correction

The phenomenon of beam hardening arises from the nature of a polychromatic X-ray source and the non-linearity between the attenuation and the material thickness. The lower energy rays are preferably attenuated than the higher energy rays, as they penetrate through a material. As a result, the effective beam energy shifts upward during the process. In other words, the beam becomes “harder”. This phenomenon is referred to beam hardening. If this beam-hardening effect is ignored, “cupping” artifacts will appear in the reconstructed images and the reconstructed attenuation is not quantitatively accurate. The cupping artifacts are caused by the fact that the rays passing though the center of the phantom are harder than the ones passing through the edges. The resultant attenuated profiles display a cupped shape compared to the ideal profiles without beam hardening. The beam-hardening artifacts become more severe for highly attenuating materials.

Correction of beam-hardening errors is essential in quantitative computed tomography (QCT). Current correction methods [7, 26, 49, 50, 56, 68, 101] can be divided into single-energy and dual-energy correction techniques. Two most commonly used single-energy techniques are the water and bone corrections. Water correction technique assumes a single-material object consisting of water. Bone correction technique usually performs water correction first and then additional correction for bone is performed. Since the single-material assumption is only partially valid, the techniques can not lead to an optimal correction. Dual-energy technique uses two polyenergetic x-ray sources and collects two sets of measurements. We summarize two techniques here: water-corrected FBP and dual-energy statistical reconstruction.

Water-Corrected FBP

Water-corrected FBP is the primary reconstruction method used clinically to eliminate some of the beam-hardening artifacts. It takes into account the X-ray spectrum in the pre-FBP processing.

This method assumes a single-material object consists only of water:

$$\mu(x, y, \mathcal{E}) = m(\mathcal{E})\rho(x, y) \tag{2.20}$$

and (2.1) becomes

$$\begin{aligned} E[Y_i] &= \int I_i(\mathcal{E})\, \mathrm{e}^{-\int_{L_i} \mu(x,y,\mathcal{E})\,\mathrm{d}\ell}\, \mathrm{d}\mathcal{E} \\ &= \int I_i(\mathcal{E})\, \mathrm{e}^{-m(\mathcal{E})\int_{L_i} \rho(x,y)\,\mathrm{d}\ell}\, \mathrm{d}\mathcal{E}\,. \end{aligned}$$

Before detailing how this method works, we first define the following notations:

$$\begin{aligned} \ell_i(\rho) &\triangleq -\int_{L_i} \rho(x, y)\, \mathrm{d}\ell \\ f_i(\ell) &\triangleq -\log\left(\frac{\int I_i(\mathcal{E})\, \mathrm{e}^{-m(\mathcal{E})\ell}\, \mathrm{d}\mathcal{E}}{I_i}\right) \end{aligned} \tag{2.21}$$

where a *total intensity* is defined

$$I_i = \int I_i(\mathcal{E}) d\mathcal{E}.$$

Since $m_{\text{water}}(\mathcal{E})$ depends only on the spectral characteristics of the material attenuation coefficient properties and we assume that the object consists of water only, $m_{\text{water}}(\mathcal{E})$ can be measured within the diagnostic x-ray energy range. By scanning a water-only phantom with a known shape (usually a cylinder), the line integral function $\ell_i(\rho)$ can be calculated analytically along different paths L_i. In principle, this water phantom scan only needs to be done once for a given scanner and source kVp setting. Then $f_i(\ell)$ is known as a function of ℓ. In reality, the water phantom scan needs careful calibration and we have only a finite number of measurements. An empirical water correction method is used [87].

By taking the logarithm of the measurements,

$$\hat{f}_i \triangleq -\log\left(\frac{Y_i}{I_i}\right), \tag{2.22}$$

we get the estimates denoted by $\hat{f}_i$ of the function $f_i(\ell)$. We can use a polynomial function to approximate the continuous function $f_i(\ell)$ (or more precisely f_i^{-1}), or build a look-up table for a certain range of ℓ. Then the estimated $\hat{\ell}_i$ of the ℓ_i's can be obtained by

$$\hat{\ell}_i = f_i^{-1}\left(\hat{f}_i\right). \tag{2.23}$$

Multiplying $\hat{\ell}_i$ by water mass attenuation coefficient $m_{\text{water}}(\mathcal{E}_0)$ for some reference energy $\mathcal{E}_0$ yields the estimated sinogram

$$\hat{p}_\varphi(r)\Big|_{L_i(r,\varphi)} = m_{\text{water}}(\mathcal{E}_0)\hat{\ell}_i. \tag{2.24}$$

Then we apply the regular FBP method mentioned in section 2.2.1 to this estimated sinogram to estimate $\hat{\mu}(x, y, \mathcal{E}_0)$. Comparing equations (2.6) and (2.24), we can see that water-corrected FBP partially takes into account the polyenergetic property of the incident spectrum by estimating $\hat{\ell}_i$ from the logarithm of the measurements.

Water-correction FBP greatly reduces the beam hardening artifacts and provides visually pleasing images. However, since the human body does not consist of only water, the reconstructed image using this method will be biased. Therefore water-corrected FBP does not provide quantitatively accurate CT values.

Dual-Energy Image Reconstruction

Dual-kVp or dual-energy image reconstruction approach [7, 38, 93] doubles the measurements by using two x-ray spectra, *i.e.*, $s = 1, 2$ in (2.26). Using these measurements from two diverse spectra, one is able to reconstruct *separate* soft tissue and bone images. The dual-energy reconstruction approach has shown promising potential for material characterization and for quantitatively accurate CT values. The conventional disadvantage of this method is the increased scan time and noise amplification due to the material decomposition process.

A more general parameterization could be used:

$$\mu(x, y, \mathcal{E}) = \sum_{l=1}^{L} \sum_{j=1}^{p} \mu_{lj}(\mathcal{E}) b_j(x, y), \tag{2.25}$$

where $\mu_{lj}(\mathcal{E}) = m_l(\mathcal{E})\rho_{lj}$ is the unknown attenuation coefficient in pixel j for lth material, L is the number of different materials, *i.e.*, the number of the spectral basis functions. In dual-kVp case, we assume the object consisting of two materials, water and cortical bone, where $L = 2$ in (2.25). The mean measurement for sth scan is given as

$$E[Y_{si}] = \int I_{si}(\mathcal{E})\, \mathrm{e}^{-\sum_{l=1}^{L} m_l(\mathcal{E})[\mathbf{A}\boldsymbol{\rho}_l]_i}\, d\mathcal{E}, \tag{2.26}$$

ignoring the background events. $\mathbf{A}$ is a system matrix with entries $a_{ij} = \int_{L_i} b_j(x, y)\, \mathrm{d}\ell$. We can use negative *penalized log likelihood* cost function as in (2.15) and apply *optimization transfer* methods to find the minimizer [38].

Water-corrected FBP can produce one image for each x-ray energy because it assumes the object consists of only water and use one-material model. Although this method overcomes some of the beam-hardening artifacts and produces visually plausible images, it introduces bias to the bone CT values which is not appropriate for the applications in which the quantitative accuracy is required, especially for bone mineral density measurements. On the other hand, dual-energy reconstruction is able to reconstruct soft tissue and bone density map separately and has the potential to provide the quantitatively accurate CT values at the price of the increased number of unknowns and possibly increased scan time and X-ray dose.

2.3 Summary

This chapter briefly reviews the X-ray CT measurement physics and the reconstruction methods of X-ray CT. Radon transform and Fourier slice theorem are also introduced. These concepts are essential as we develop the NUFFT-based forward and backprojectors and propose an analytical variance prediction method in the following chapters.

In chapter 3, we extend the Fourier-based projectors to a fan-beam geometry based on Fourier slice theorem and fan-to-parallel rebinning. For properly chosen parameters, an $O(N^2 \log N)$ forward/backprojector pair is developed.

Statistical image reconstruction methods offer better bias-variance tradeoff over conventional image reconstruction methods. However, noise properties of the reconstructed images have not been well studied. In chapter 4 and 5, analytical variance prediction methods are proposed for 2D fan-beam and 3D cone-beam geometries.

CHAPTER 3

Nonuniform Fourier Transform-Based Projectors for Fan-Beam Transmission Tomography [1]

The classical approach to reconstructing tomographic images is filtered back-projection. Statistical image reconstruction methods are based on models for measurement statistics and physics, and offer some attractive features such as the potential for improved image quality and reduced dose. A drawback of statistical image reconstruction methods (compared to FBP) is the longer computation time of the iterative algorithms.

Most iterative algorithms require one forward projection and one backprojection for each iteration. These projection steps are the computational bottleneck. The Fourier-slice theorem relates the 2D Fourier transform of the object and the 1D Fourier transforms of sinogram data along radial direction at different view angles. It suggests a forward projection scheme involving taking 2D Fourier transform of the object followed by the 1D inverse Fourier transforms at different views. This forward projection scheme should work exactly in the continuous spaces. For the discrete spaces in which computed tomography works, discrete Fourier transform can be implemented using fast Fourier transform (FFT) that is very computation-efficient. Therefore, Fourier-based projectors have the potential to greatly reduce the computation time. However, the FFT results does not give the

---

[1] This chapter is based on material from [106].

samples at the same frequency locations as shown in Figure 2.7. In parallel-beam tomography, the Fourier-based forward projector involves a non-uniform fast Fourier transform (NUFFT) obtaining polar spectral samples that are non-uniformly spaced in Cartesian coordinates from Cartesian images samples. Some interpolation is needed here and low interpolation error is the key for the good performance of this type of projectors.

Two important requirements are imposed on the NUFFT that are suitable for developing Fourier-based projectors in computed tomography: interpolation accuracy and computation efficiency. Matej *et al.* evaluated forward and back projectors [34, 41, 64, 65] that used a NUFFT with a min-max optimized Kaiser-Bessel (KB) interpolation kernel [42]. Their results showed low interpolation error and good computation efficiency. This chapter presents an extension of this NUFFT approach to the fan-beam geometry that is used widely in X-ray CT systems [104].

There are two complications in extending Fourier-based projectors to a fan-beam geometry. Firstly, in the fan-beam case there is no suitable Fourier slice theorem. (A recent extension is suitable for analytical reconstruction [21], but it is not evident how to use it for forward projection.) Therefore, we use the usual Fourier slice theorem and interpolate into the fan-beam coordinates. To ensure good accuracy and compute efficiency, we use a min-max optimized KB NUFFT approach for the radial "interpolation." The second complication is that Fourier-methods are efficient only for shift-invariant detector response models. In emission tomography with converging (fan-beam) collimators, the detector response is highly shift variant, and it is unlikely that Fourier-based methods can be suitable. We focus here on transmission tomography for the fan-beam geometries of typical clinical X-ray CT scanners, where the variation in detector response over the field of view is often fairly modest. We approximate the detector response by the effective width at the center of the field of view, and investigate the effect of this approximation. We focus on iterative reconstruction but we note for completeness that NUFFT-based direct Fourier image reconstruction methods have also been investigated [23] [43].

3.1 Nonuniform Fourier Transform (NUFFT)

The practical implementation of discrete Fourier transform, fast Fourier transform (FFT) is very computationally efficient when uniformly-spaced frequency samples are needed. FFT requires $O(N \log N)$ operations rather than $O(N^2)$ direct computation of discrete Fourier transform in 2D case when we have N by N image samples. However, in some applications where non-uniform frequency domain sampling is needed, FFT is not applicable. The fast approximation of the *non-uniform Fourier transform* [12] is required to retain the computation advantages of fast algorithm like FFT. It is called *non-uniform fast Fourier transform* (NUFFT). Interpolation errors are a limitation.

Recently, the NUFFT using min-max interpolation has been proposed by Fessler [42], and numerical results showed that this approach has lower approximation error than conventional interpolation methods. It has also been found that the conventional interpolators such as Kaiser-Bessel and Gaussian bell interpolators, with min-max optimized parameters provide a comparable accuracy as the min-max interpolator if larger neighborhood J is chosen. Particularly, Kaiser-Bessel interpolator, if suitably optimized, can provide a reasonable trade-off between accuracy and computation simplicity.

Min-Max Non-Uniform FFT

In parallel-beam and fan-beam tomography, 2D non-uniform FFT is needed. For simplicity, we consider 1D case first. The extension to 2D case is straightforward. The discussion follows the main idea in [42]. The basic steps of a 1D NUFFT are:

1. Calculation of a K/N times oversampled and scaled FFT:

   $$Y[k] = \sum_{n=0}^{N-1} s[n]x[n]\,\mathrm{e}^{-i\gamma kn} \tag{3.1}$$

   for $k = 0, \ldots, K-1$ and $\gamma = 2\pi/K$. $s[0], \ldots, s[n-1]$ are the predetermined scaling factors.

2. Interpolation onto the desired, non-uniformly spaced frequency locations ω_m, where $m = 1, \ldots, M$ with J nearest neighbors:

   $$\hat{X}(\omega_m) = \sum_{j=0}^{J-1} u_{mj}^{*} Y[\{k_0(\omega_m) + j\}_K], \tag{3.2}$$

   where u_{mj}s are the interpolation coefficients, "$*$" denotes complex conjugate, $\{\cdot\}_K$ denotes module-K operation and $k_0(\omega)$ is integer offset defined as:

   $$k_0(\omega) = \begin{cases} (\arg\min_{k\in\mathbb{Z}} |\omega - \gamma k|) - \frac{J+1}{2}, & J \text{ odd} \\ (\max\{k \in \mathbb{Z} : \omega \geq \gamma k\}) - \frac{J}{2}, & J \text{ even} \end{cases}. \tag{3.3}$$

   The integer offset function satisfies the following shift property:

   $$k_0(\omega + l\gamma) = l + k_0(\omega),\ \forall l \in \mathbb{Z}.$$

For min-max interpolator, we choose the interpolator $\mathbf{u}_m \triangleq (u_{m0}, \ldots, u_{m(J-1)})$ and scaling factors $\mathbf{s} \triangleq (s[0], \ldots, s[n-1])$ that minimizes the worst approximation error:

$$\min_{\mathbf{s}} \max_{\omega} \min_{\mathbf{u}(\omega)} \max_{\mathbf{x}:\|\mathbf{x}\|\leq 1} \left| \hat{X}(\omega) - X(\omega) \right|.$$

As shown in [42], the inner optimization of the interpolation coefficients $\mathbf{u}(\omega)$ for a fixed scaling vector $\mathbf{s}$ has an analytical solution by firstly finding the worst case signal $\mathbf{x}$ using Cauchy-Schwartz inequality and then transforming the inner optimization into an ordinary least-squares minimization. The outer optimization requires numerical evaluation.

One critical problem remains in the design of the min-max interpolator: the appropriate choice of the scaling factors, $\mathbf{s}$. The simplest choice is a unity scaling vector such that

$s[n] = 1$ for all n (trivial scaling in [69] or uniform scaling in [42]). A more sophisticated choice requires exhaustive minimization on the maximum error. A truncated Fourier series is used to expand $s[n]$s:

$$s[n] = \sum_{l=-L}^{L} c_l \, \mathrm{e}^{i\gamma\zeta(n-\frac{N-1}{2})}\,, \tag{3.4}$$

for $n = 0, \ldots, N-1$. c_ls are Hermitian symmetric Fourier coefficients and ζ is the design parameter. Brutal-force global search is used jointly to find the best c_ls and ζ. The unity scaling vector is a special case of (3.4) such that $\zeta = 0$ and $c_l = 1/(2L+1)$. The cosine scaling factors considered in (3.4), [69] is another special case corresponding to $\zeta = 0$ and $\mathbf{c} = (0, 1/2)$. As shown in [42], using the scaling vector by exhaustive search provides lower interpolation error than using the unity scaling vector that in turn outperforms the cosine scaling vector. However, the complexity of this choice of scaling factors increases greatly as truncation length L increases. Therefore, we need a practical procedure that gives a good trade-off between computation simplicity and interpolation accuracy. We discuss this procedure next.

2D non-uniform FFT is a straightforward generalization of 1D case. We compute a K_1K_2/N_1N_2 times oversampled and scaled 2D FFT:

$$Y[k_1, k_2] = \sum_{n_1=0}^{N_1-1} \sum_{n_2=0}^{N_2-1} s[n_1, n_2] x[n_1, n_2] \, \mathrm{e}^{-i(\gamma_1 k_1 n_1 + \gamma_2 k_2 n_2)} \tag{3.5}$$

For simplicity, we use *separable* scaling factors $s[n_1, n_2] = s[n_1]s[n_2]$ in [34].

Min-Max Optimized Kaiser-Bessel Non-Uniform FFT

Although exhaustively minimized scaling factors in (3.4) yields low interpolation error, the optimization of the scaling factors remains a complex problem and imposes computation challenge. A practical procedure is proposed in [42] using suitably optimized conventional shift-invariant interpolators, such as Gaussian bell or Kaiser-Bessel interpolators. Error analysis shows that for a given interpolation kernel $g(\cdot)$ with finite support, the following scaling factors minimize the worst case error at the DFT sample locations:

$$s[n] = \frac{1}{\int_{l=-J/2}^{J/2-1} \mathrm{e}^{i\gamma l(n-\frac{N-1}{2})}\, g(l)\, \mathrm{d}l}. \tag{3.6}$$

Using the min-max criterion, the conventional interpolators are also able to provide the accuracy comparable to min-max interpolator. In our studies, the min-max optimized Kaiser-Bessel interpolator is used for its reasonable trade-off between accuracy and simplicity. We will focus on Kaiser-Bessel interpolator from now on. The generalized Kaiser-Bessel function [60] has the following form:

$$g(\kappa)_{m,J,\tau} = f_J^m(\tau) \frac{I_m(\tau f_J(\kappa))}{I_m(\tau)} \tag{3.7}$$

where κ is the distance from KB window center, I_m denotes the modified Bessel function of order m, J is window size and parameter τ controls the kernel shape and frequency characteristics [60, 66].

$$f_J^m(\kappa) = \begin{cases} \sqrt{1 - \left(\frac{\kappa}{J/2}\right)^2}, & |\kappa| < \frac{J}{2} \\ 0, & \text{otherwise} \end{cases} \tag{3.8}$$

Numerical results in [42, 65] show that the approximation error decreases rapidly with the increase of oversampling factor K/N and for a fixed K/N, the min-max optimal Bessel function order is $m \approx 0$. For a fixed oversampling factor K/N and at $m = 0$, the optimal ratio τ/J is around 2.34 for a range of kernel size.

Min-Max Non-Uniform inverse FFT

By duality *i.e.*, by changing the sign in the exponent of (3.1), one can use the above procedure of computing NUFFT to evaluate a nonuniform inverse FFT when given uniformly-spaced spectral samples, and non-uniformly spaced spatial samples are needed.

3.2 NUFFT-Based Forward and Back-Projectors in Parallel-Beam Tomography

Min-max NUFFT has been applied recently to parallel-beam iterative image reconstruction by Matej *et al.* [65] and the results show low approximation errors and computation efficiency. The Fourier slice theorem is the basis of the Fourier-based forward and back-projections in parallel beam CT image reconstruction. Figure 3.1 illustrates the NUFFT-based forward projector.

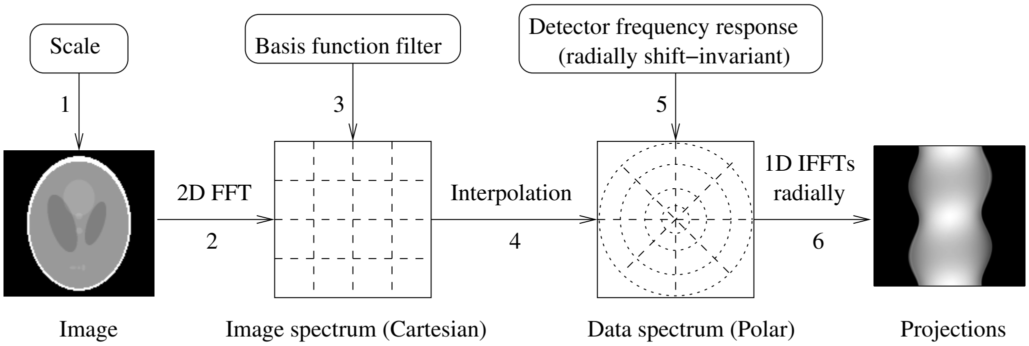

Figure 3.1: Basic steps of NUFFT forward projector.

Step 1 and 2 give us the spectral samples uniformly-spaced in Cartesian grid:

$$Y[k_1, k_2] = \sum_{n_1=0}^{N_1-1} \sum_{n_2=0}^{N_2-1} s[n_1]s[n_2]x[n_1, n_2]\,\mathrm{e}^{-i(\gamma_1 k_1 n_1 + \gamma_2 k_2 n_2)} \tag{3.9}$$

In the practice of image reconstruction, we work on a discretized version of continuous image, represented as a sum of weighted basis functions:

$$f(x, y) = \sum_{n_1=0}^{N_1-1} \sum_{n_2=0}^{N_2-1} f[n_1, n_2]b(x - n_1\triangle_1, y - n_2\triangle_2) \tag{3.10}$$

where $f[n_1, n_2]$ denotes the values of the continuous image $f(x, y)$ and $b(x - n_1\triangle_1, y - n_2\triangle_2)$ is the basis function such as square pixels or blob at location $[n_1\triangle_1, n_2\triangle_2)]$. Typically, the basis functions are spatially invariant and therefore could be imitated in the image frequency domain by including a basis function filter. In our studies, we use square pixels

$$b(x,y) = \text{rect}\left(\frac{x}{\triangle_1}\right)\text{rect}\left(\frac{y}{\triangle_2}\right) \tag{3.11}$$

Therefore, the basis function filter used in step 3 is

$$B(f_x,f_y) = \triangle_1\,\triangle_2\,\text{sinc}(\triangle_1 f_x)\text{sinc}(\triangle_2 f_y) \tag{3.12}$$

Step 3 performs the multiplication between the image spectral samples and the samples of $B(f_x,f_y)$:

$$Z[k_1,k_2] = Y[k_1,k_2]\cdot B[k_1,k_2] \tag{3.13}$$

where $B[k_1,k_2]$ is the basis function filter sampled at locations $(2\pi k_1/K_1, 2\pi k_2/K_2)$, $k_1 = -K_1/2,\ldots,K_1/2-1$ and $k_2 = -K_2/2,\ldots,K_2/2-1$, assuming K_1, K_2 are even.

Step 4 interpolates the uniformly-spaced Cartesian samples $Z[k_1,k_2]$ into polar grid and $Z_\theta[k]$'s are obtained.

In parallel beam geometry, the radially invariant detector blur can also be modeled by multiplying the data spectrum $Z_\theta[k]$'s radially by the samples $H[k]$'s of the detector frequency response $H(\rho)$. A choice for $h(r)$ is

$$h(r) = \frac{1}{w}\text{rect}\left(\frac{r}{w}\right) \tag{3.14}$$

where w is the finite width of the detector elements.

3.3 NUFFT-Based Forward and Back-Projectors in Fan-beam Tomography

There are two complications in extending Fourier-based projectors to a fan-beam geometry. Firstly, in the fan-beam case there is no suitable Fourier slice theorem. (A recent extension is suitable for analytical reconstruction [21], but it is not evident how to use it for forward projection.) Therefore, we use the usual Fourier slice theorem and interpolate into the fan-beam coordinates. To ensure good accuracy and compute efficiency, we use a min-max optimized KB-NUFFT approach for the radial “interpolation.” The second complication is that Fourier-methods are efficient only for shift-invariant detector response models. In emission tomography with converging (fan-beam) collimators, the detector response is highly shift variant, and it is unlikely that Fourier-based methods can be suitable. We focus here on transmission tomography and the fan-beam geometries of typical clinical X-ray CT scanners, where the variation in detector response over the field of view is often fairly modest. We approximate the detector response by the effective width at the center of the field of view, and investigate the effect of this approximation. This effective detector width is calculated by multiplying the actual detector width by the ratio of the source-to-isocenter distance over the source-to-detector distance.

The Fourier slice theorem [52] is the foundation of Fourier-based forward projection. Let η denote the 2D image and denote its 2D FT in polar coordinates by

$$G_\varphi(\rho) \triangleq \iint g(x,y)\, \mathrm{e}^{-\imath 2\pi\rho(x\cos\varphi + y\sin\varphi)}\, \mathrm{d}x\, \mathrm{d}y\,. \tag{3.15}$$

The ideal line-integral projection of $g(x,y)$ at angle φ (taken counter-clockwise from the y axis) as a function of the radial distance r from the origin is given by

$$p_\varphi(r) = \int \eta[r\cos\varphi - \ell\sin\varphi,\; r\sin\varphi + \ell\cos\varphi]\, \mathrm{d}\ell\,. \tag{3.16}$$

For our purposes, the most convenient form of the Fourier slice theorem expresses each projection as a 1D inverse Fourier transform of $G_\varphi(\rho)$ as follows:

$$p_\varphi(r) = \int G_\varphi(\rho)\, \mathrm{e}^{\imath 2\pi\rho r}\, \mathrm{d}\rho\,. \tag{3.17}$$

Fourier-based projectors use discretized versions of (3.15) and (3.17), whereas space-based projectors discretize (3.16).

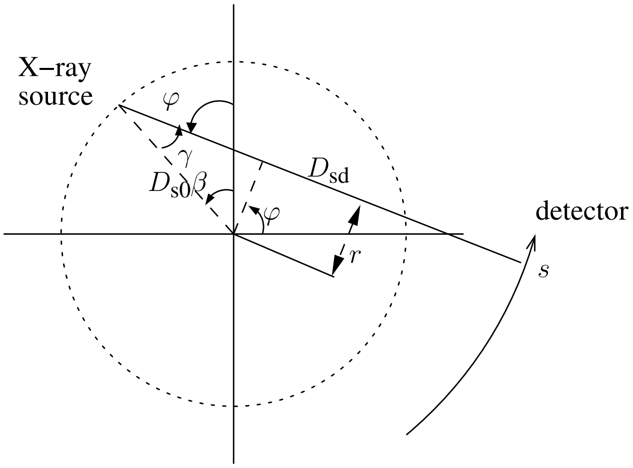

Figure 3.2: Angular coordinates in fan-beam geometry.

3.3.1 Fan-Beam Tomography

As illustrated in figure 3.2, fan-beam rays are indexed by angular coordinates (β, γ), where β is the angle of the source relative to the y axis, and γ is the angle of the ray relative to the source. Fan-beam FBP methods exist only for special detector configurations [18]. Here we accommodate any set of samples γ_m, $m = 1, \ldots, N_\gamma$, where $\gamma = s/D_{\mathrm{sd}}$. We assume that β is sampled uniformly, *i.e.*, $\beta = 2\pi \frac{k}{N_\beta}$, $k = 0, \ldots, N_\beta - 1$, although this could be relaxed.

To develop a Fourier-based projector for fan-beam geometries, we use the well-known relation between parallel-beam and fan-beam coordinates [73]:

$$r = D_{\mathrm{s0}} \sin \gamma \tag{3.18}$$

$$\varphi = \beta + \gamma, \tag{3.19}$$

where D_{s0} is the source to rotation center distance, illustrated in figure 3.2. For typical angular samples $\{\gamma_m\}$, the corresponding radial samples $r_m \triangleq D_{\mathrm{s0}} \sin \gamma_m$ are spaced non-uniformly. And when β is sampled uniformly, for a given γ_m (or equivalently a given r_m), the corresponding values of φ are also equally spaced but shifted by γ_m.

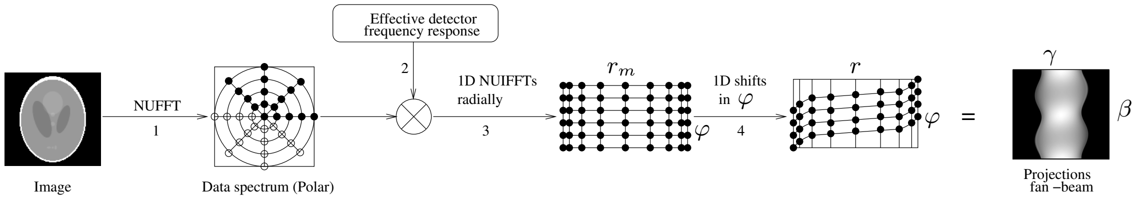

Figure 3.3: Basic steps of NUFFT forward projection in fan-beam CT. 1) 2D NUFFT of image to obtain polar spectrum samples. 2) Multiply radially by the frequency response of the effective detector blur. 3) 1D NUFFTs along radial direction r for each φ. 4) 1D shifts in φ using interpolation with periodic end condition.

3.3.2 NUFFT-Based Fan-Beam Forward and Back Projectors

Figure 3.3 shows the four major steps of the proposed fan-beam NUFFT-based forward projector. These four steps are summarized next.

2D Non-Uniform Fast Fourier Transform

Step 1 in figure 3.3 uses a 2D NUFFT to evaluate a discretized version of (3.15). The input is $N_1 \times N_2$ samples of the image η. The output is polar coordinate samples of $\mathcal{G}_+$ that are equally-spaced along ρ at locations $\{n\Delta_\rho\}$, for $n = -N_1/2, \ldots, N_1/2 - 1$, where Δ_ρ is the sample spacing in ρ. N_1 is chosen based on the choice of Δ_ρ and the extent of the spectral samples. In light of (3.19), we use φ samples that match the β samples, *i.e.* $\theta_k = 2\pi \frac{k}{N_\beta}$.

Step 1 is identical to the parallel-beam case that is detailed in [34, 41, 42, 64, 65]. It involves the following operations.

(i) Multiply the 2D image samples by a scaling function that precompensates for imperfections in the frequency-domain interpolator. We use separable Kaiser-Bessel scaling functions for simplicity [42].

(ii) Calculate a $K_1 \times K_2$ point (oversampled) 2D FFT of the scaled discrete image. Typically $K_1 = 2N_1$ and $K_2 = 2N_2$.

(iii) Interpolate onto the desired, non-uniformly spaced frequency locations from the

$J \times J$ nearest neighbors, using the Kaiser-Bessel interpolator that minimizes the worst-case approximation error [47, 72].

(iv) Multiply by the spectrum of the image-domain basis function (typically square pixels).

By choosing sufficient oversampling and sufficiently large $J \times J$ neighborhood, very high accuracy is achieved [42, 65].

Approximating Detector Response

In parallel-beam tomography, one can model shift-invariant detector blur in the frequency domain by multiplying the image spectrum $\mathcal{G}_+$ with the frequency response of the detector blur [65]. In fan-beam tomography, detector blur effects depend on the distances between each image pixel and the detector elements, and hence cannot be modeled exactly in the frequency domain. For example, in the CT system described in Section 4.5.4, the effective detector width varies from 0.22 mm to 0.64 mm over a 40 cm field of view. For simplicity, we approximate the depth-dependent detector response by the effective beam width at the rotation center, calculated by multiplying the actual detector width by the ratio of the source-to-isocenter distance over the source-to-detector distance.

Simulations in Section 4.5.4 evaluate the effects of this shift-invariant approximation.

The next two steps in figure 3.3 also differ between the parallel-beam and fan-beam geometries.

1D Non-Uniform IFFTs

Step 3 in figure 3.3 evaluates a discretized version of (3.17). In the parallel-beam case, a simple 1D inverse FFT along r for each θ_k will suffice [65]. For the fan-beam case, the desired radial samples r_m are spaced unequally, per (3.18). We discretize (3.17) as follows for $m = 1, \ldots, M$:

$$p_{\theta_k}(r_m) \approx \sum_{n=-\frac{N_1}{2}}^{\frac{N_1}{2}} G_{\theta_k}(n\Delta_\rho)\, \Delta_\rho\, \mathrm{e}^{\imath 2\pi \Delta_\rho n r_m}, \tag{3.20}$$

where we choose $\Delta_\rho \leq \frac{1}{2r_{\max}}$ to avoid aliasing.

Since the r_m values are spaced unequally, whereas the $\rho_n = n\Delta_\rho$ values are spaced equally, we evaluate (3.20) for each θ_k using a 1D NUFFT with "frequency" locations $-2\pi\Delta_\rho r_m$ [42].

1D Shifts Using FFT-Based Interpolations

After step 3 in figure 3.3, we have projection data that is non-uniformly spaced in r (corresponding to each γ_m), and uniformly-spaced in φ. For each $m = 1, \ldots, N_\gamma$, a 1D shift (by γ_m, see (3.19)) in the φ direction is needed. Since projections are 2π periodic in φ, Dirichlet-like "periodic sinc" interpolation is a natural choice to "fractionally shift" the resulting projection data in the previous step into the desired φ locations. We use 1D FFTs for this final step [44].

Symmetry Properties

Because the input image, $g(x, y)$ is real in CT, its Fourier Transform, $\mathcal{G}_+$ is Hermitian symmetric. Thus, only half of the Fourier samples must be calculated in the 2D NUFFT (step 1) and the 1D NUFFT (step 3). In particular, we implement (3.17) as follows:

$$p_{\theta_k}(r_m) \approx G_\theta(0) + 2 \cdot \mathrm{real}\left\{ \sum_{n=1}^{\frac{N_1}{2}} G_{\theta_k}(n\Delta_\rho)\, \Delta_\rho\, \mathrm{e}^{\imath 2\pi \Delta_\rho n r_m} \right\}. \tag{3.21}$$

This approach reduces computation and also ensures that the projections are entirely real valued. There may still be small negative values even if g is nonnegative. For some iterative algorithms these may need be set to zero.

For further savings, we exploit the Radon symmetry property: $p_\theta(-r) = p_{\theta\pm\pi}(r)$. So we only need to compute the polar frequency samples for $\theta \in [0, \pi)$ instead of $[0, 2\pi)$ in step 1 shown in figure 3.3.

Backprojection

Iterative algorithms require repeated forward and back-projections, where the back-projector is the adjoint operator of the forward projector. We implement the back-projector by *"reversing"* (not inverting!) the linear steps above. This approach provides an exact adjoint, so the forward and back projectors are matched perfectly.

3.3.3 Theoretical Analysis of Operation Flops

NUFFT-based			space-based (line integral)
steps	FFT	interpolation	
2D NUFFT	$2N^2 \log N$	$J^2 N_\gamma N_\beta / 4$	$O(N_\beta N_\gamma N)$
1D NUFFTs	$N_\beta N_\gamma \log N_\gamma$	$J_1 N_\gamma N_\beta$	
1D shifts	$2N_\beta \log N_\beta$		

Table 3.1: Floating-point operations for NUFFT-based and space-based forward projectors. Assumes $N \times N$ image and $N_1 \approx N_\gamma$.

Table 3.1 summarizes the dominant operation counts for the NUFFT-based forward projector. The expressions are for a $N \times N$ image and a $N_\gamma \times N_\beta$ sinogram. We use a $J \times J$ neighborhood of 2D DFT samples for interpolation in the 2D NUFFT, and J_1 neighbors for the 1D NUFFT. The 2D NUFFT computes $N_1 \times N_\beta/4$ polar frequency samples.

For comparison, a line-length space-based forward projector requires $O(N_\beta N_\gamma N)$ operations, where the proportionality constant can be large when the intersection lengths are computed on the fly (rather than precomputed) due to the very large image sizes in CT.

In the usual 3rd-generation CT fan-beam geometry where $N_\gamma \approx 2N$ and $N_\beta \approx 2N$, the overall computation for the NUFFT-based forward projector is $O(N^2 \log N)$, akin to previous hierarchical methods [16], whereas most space-based forward projectors require $O(N^3)$ operations.

3.4 Simulation and Real Data Results

We simulated a 3rd-generation fan-beam X-ray CT system with sinogram size of approximately $1.7N$ radial bins by $2N$ views over 360°. The source to detector distance, D_{sd}, is about 949mm, and the rotation center to detector distance is about 408mm. Thus $D_{\text{s0}} = 541$mm. For example, when $N = 512$, the corresponding sinogram size is 888 samples in γ, spaced by $\triangle_\gamma \approx 0.06^\circ$ and 984 source positions over 360°, so $\triangle_\beta \approx 0.37^\circ$. A quarter detector offset is also included to reduce aliasing. Except where noted below, we use $N_\rho = 1.7N$ and $\Delta_\rho = 1/\text{FOV}$ in (3.21). In all simulations, we used Shepp-Logan digital phantom and assume mono-energetic X-ray source.

The Fourier-based method is implemented in Matlab (version 7.0.4) using double precision; the NUFFT spectral interpolator is an ANSI C MEX routine. The space-based projector is an ANSI C MEX routine using single precision. All projectors are evaluated on a Dell 670n computer with dual Intel Xeon 3.40GHz CPU.

The space-based projector used here was designed originally for coordinate-wise algorithms, *e.g.*, [39]. It was not optimized for ray-driven calculation of the line-integral model described in Model 1 in section 3.4.1. Its primary role here is for accuracy comparisons.

3.4.1 Forward and Back-Projector as Single Modules

We evaluated the NUFFT-based fan-beam forward and back-projectors using the Shepp-Logan digital phantom. The brain-size field of view is approximately 308mm, thus pixel size is about 0.6mm for $N = 512$.

Forward Projector

We investigated four different scenarios, involving three different analytical models. All models used the analytical formula for the fan-beam projections of ellipses to provide a "gold standard" reference sinogram.

Analytical model 1: line integral model.

Here we used the analytical formula for the fan-beam line-integral projections of an ellipse, sampled at the center of each detector element. For the NUFFT approach we set the detector frequency response to unity. For the space-based approach we set a_{ij} to the usual length of intersection of the ith ray with the jth pixel. (This was implemented by setting the beam-width in Model 2 below to zero, rather than by developing an optimized, ray-driven line-integral algorithm.) This line-integral model is often used in evaluating forward projectors.

Analytical model 2: linear averaging model.

The line-integral model is unrealistic since detectors have finite width and they average the incoming signal across that width. For Model 2, we generated the reference sinogram by linearly averaging 8 analytical rays sampled across each detector element. This also accounts for depth-dependent detector response. For the NUFFT method, we accounted for the finite beam width approximately by using the beam width at the center of the field of view. For the space-based approach, we computed a_{ij} as the area of intersection between the jth pixel and the thin-wedge connecting the point X-ray source with the ith finite-width detector. That space-based model accounts for distance dependent beam-width but increases computation.

Analytical model 3: nonlinear averaging model.

Due to the nonlinearity of Beer's law, the linear averaging model is imperfect. For Model 3, instead of linearly averaging the 8 analytically computed line integrals per

analytical models	Model 1		Model 2		Model 3a		Model 3b	
discretized models	space	NUFFT	space	NUFFT	space	NUFFT	space	NUFFT
max % error	7.03	6.13	2.31	2.15	2.91	2.71	2.64	2.67
ℓ_1 % error	0.13	0.10	0.07	0.08	0.07	0.08	0.07	0.09
% nrms error	0.28	0.25	0.16	0.16	0.17	0.17	0.16	0.16

Table 3.2: Space-based and NUFFT-based forward projectors of 512×512 image compared to exact analytical projections for three different analytical models. Model 1: analytical, space-based and NUFFT-based methods all use line integrals. Model 2: analytical method linearly average 8 rays across one detector element; space-based method uses the thin-wedge beam and NUFFT-based method approximates the beam width at the rotation center. Model 3a: analytical method nonlinearly average 8 rays across one detector element before taking the logarithm; space-based method uses thin-wedge beam; NUFFT-based method uses the beam width at the rotation center. Model 3b: As in Model 3a except NUFFT and space-based both use multi-line nonlinear averaging.

detector element used in Model 2, we formed the reference sinogram by computing the negative logarithm of the average of the exponentials of the negatives of these ray values multiplied by 0.02/mm. This nonlinear averaging introduces the "exponential edge gradient effect" that occurs in practice [51].

For this reference sinogram, we compared two different approaches to pixelized forward projectors. For Model 3a we used the same NUFFT and space-based forward projectors described under Model 2. Those projectors use linear averaging so increased errors are expected. For Model 3b we used over-sampled versions of the line-integral models described under Model 1 and nonlinearly averaged the resulting line integrals over each detector element. These over-sampling approaches require much more computation than may be practical for routine use, but better match the nonlinearly averaged analytical sinogram. In this model, all of the methods account for distance-dependent beam width.

For all of the above scenarios, we computed the normalized maximum error, $\frac{\max_j(|x_j - y_j|)}{\max_j(|x_j|)}$, and the normalized ℓ_p error, $\frac{\|x_j - y_j\|_p}{\|x_j\|_p}$, specifically the normalized absolute error (ℓ_1 error) and the normalized root mean square (NRMS) error. For 1D and 2D NUFFT, we used FFT oversampling factor $K/N = 2$ and the number of neighbor samples $J = 5$. Table 3.2

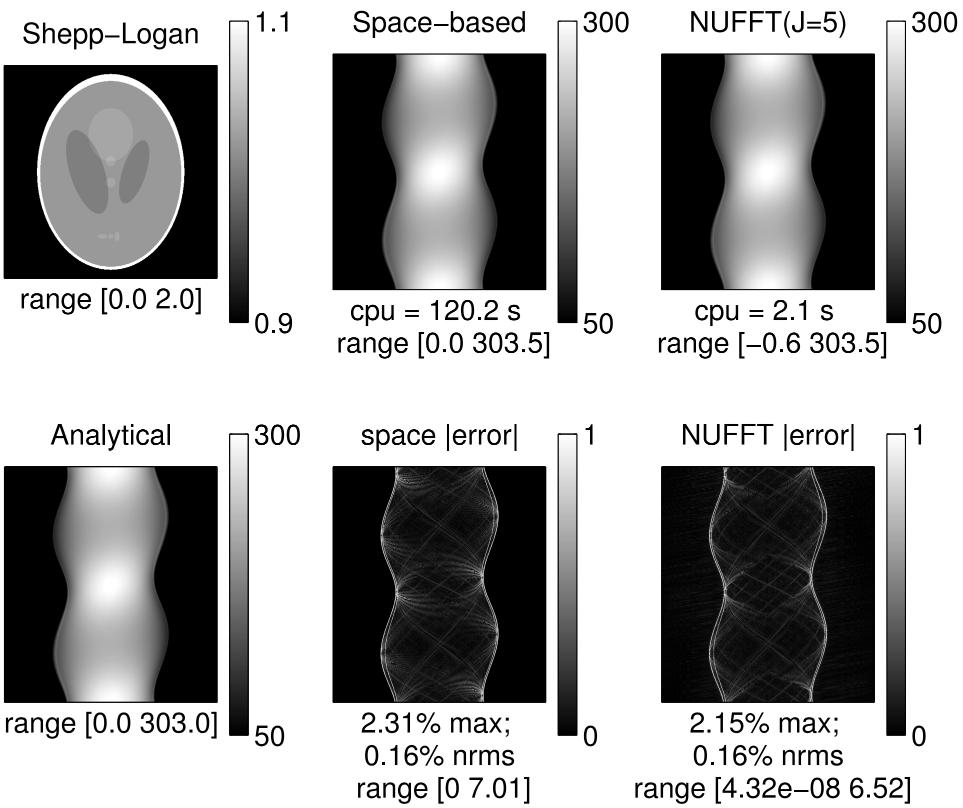

Figure 3.4: Simulation results for forward projectors of image size 512×512 in Model 2: sinogram size of 888 bins by 984 views. The gray-scale ranges were chosen to show details. The exact range are shown below each Figure.

summarizes the comparisons under these three different models. The space-based and NUFFT-based forward projectors perform similarly for all situations, despite the approximated detector response model.

We also performed the forward projections on various image sizes, $N = 128, 256, 384, 512$ and 1024. figure 3.4 shows the projections of an image of size 512^2 in Model 2. The sinograms are visually indistinguishable. The accuracy of the NUFFT-based method is comparable with the space-based method, while the computation time (using Matlab `cputime` command) is about 57 times faster. This acceleration factor does not equal to $\frac{N}{\log N}$ due to other constants.

Table 3.3 further compares the computation times and accuracies for images of various sizes. To further demonstrate the computation efficiency, we also include the performance

Image size	CPU time (in seconds)				max % error			% nrms error		
	Space		NUFFT	DD	Space	NUFFT	DD	Space	NUFFT	DD
	(line)	(beam)			(beam)			(beam)		
128^2	1.7	1.9	0.1	0.1	3.57	3.82	3.58	0.64	0.63	0.61
256^2	13.5	15.2	0.5	0.7	3.05	3.76	3.05	0.31	0.31	0.30
384^2	45.4	50.9	1.2	2.1	2.34	2.97	2.34	0.21	0.21	0.20
512^2	106.9	120.2	2.1	5.0	2.31	2.15	2.31	0.16	0.16	0.15
1024^2	852.5	956.3	8.6	39.2	1.53	1.58	1.53	0.08	0.08	0.07

Table 3.3: Comparison of space-based, NUFFT-based and distance-driven (DD) forward projectors for various image sizes.

of the fast distance-driven (DD) projector proposed recently by De Man *et al.* [24], which is a $O(N^3)$ method, implemented as a C MEX interface to C++ code provided by those authors. The computation time of the NUFFT-based forward projector is comparable to the distance-driven forward projector for small images and is about 2 to 4 times faster for larger images. The benefits of a $O(N^2 \log N)$ method improves as N increases, but in practice, the preferred method will depend on hardware considerations like pipelining.

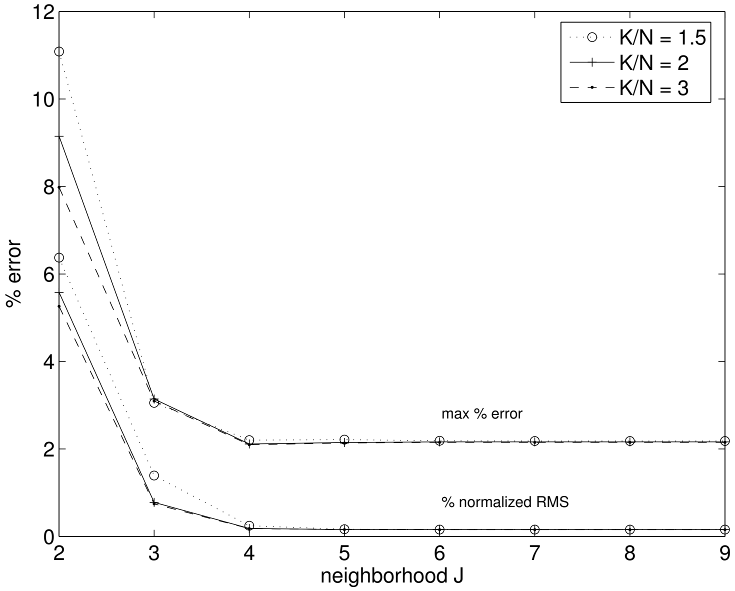

Figure 3.5: Trade-off between NUFFT-based forward projector accuracy and oversampling factor K/N and neighborhood $J \times J$ for 512^2 image.

Figure 3.5 shows the accuracy as a function of the oversampling factor K/N and the neighborhood size J. This plot suggests that $J = 4$ would be adequate. However, this plot shows only the accuracy in the sinogram domain. In the image domain, some ringing artifacts appeared in the NUFFT image for $J = 4$, suggesting that the sinogram domain does not adequately reveal high frequencies. Therefore in all subsequent results, we chose $J = 5$.

Back-Projector

To evaluate the back-projector, we processed the sinogram obtained from the analytical projections with the first two steps in the fan-beam FBP method. Since there is no easy way to calculate the exact back-projections analytically, here we applied only space-based and NUFFT-based methods to this processed sinogram.

In results not shown, the computation efficiencies and accuracies were very similar to those in Table 3.3, as is expected because the back-projector is the exact adjoint of the forward projector. For a 512^2 image, the back-projection times for the space-based, NUFFT and DD methods were 245.2, 2.4 and 5.1 seconds, respectively.

3.4.2 Forward and Back-Projectors within Iterative Reconstruction

Because even small approximation errors might accumulate after many iterations, it is necessary to evaluate the accuracy of the NUFFT-based projectors in iterative reconstruction methods.

Simulation Study

We used the analytical method mentioned under “Model 2” in section 3.4.1 to simulate a noiseless sinogram $\mathbf{y}$ from a Shepp-Logan phantom. The sinogram size was 888 radial bins by 984 views over 360°. We ran 200 iterations of the conjugate gradient algorithm, initialized with $\mathbf{x} = \mathbf{0}$, for the following penalized weighted least-squares cost function with a quadratic roughness penalty (QPWLS-CG)

$$\Phi(\mathbf{x}) = \sum_{i=1}^{N_d} w_i \frac{1}{2}(y_i - [\mathbf{A}\mathbf{x}]_i)^2 + \alpha R(\mathbf{x}) \tag{3.22}$$

$$R(\mathbf{x}) = \sum_k \psi([\mathbf{C}\mathbf{x}]_k), \tag{3.23}$$

where y_i is the negative $\log$ of the measured sinogram, w_is are statistical weighting factors, $\mathbf{A}$ is the system matrix, $\mathbf{C}$ is a differencing matrix and $\psi(t)$ is the potential function. Here $\psi(t) = t^2/2$, a quadratic penalty. For this simulation, we used $w_i = \exp(-\xi[\mathbf{A}\mathbf{x}]_i)$ where ξ is a scaling factor chosen to set the maximum value of $\xi[\mathbf{A}\mathbf{x}]_i$ to about 5. We chose $\alpha = 2^8$ for this simulation. Evaluating the PSF using the approximations described in [40] shows that the FWHM is about 2.1 pixels, *i.e.*, 1.3mm, for this value of β. We used the modified quadratic roughness penalty in [40] to obtain approximately uniform resolution.

We ran QPWLS-CG using the distance-driven, space-based and NUFFT-based forward and back projectors respectively. Here, we used $N_\rho = 1332$ in (3.21).

Figure 3.6 shows that the reconstructed images are visually indistinguishable even with a 200HU window. Figure 3.7 shows the profiles through the region of interest containing the small features in lower part of the phantom. The max percent difference between NUFFT-based and space-based and distance-driven methods is less than 1.4% and normalized RMS is about 0.3%. This difference is much smaller than the 3.7% NRMS error of the PWLS estimates themselves (compared to the true object). The NUFFT method exhibits oscillations of about 1HU in this region. This could be reduced by increasing N_ρ at the price of increased computation. The computation time is reduced by a factor of 80 for the NUFFT approach compared to the space-based method and a factor of 2 for the NUFFT approach compared to the distance-driven method.

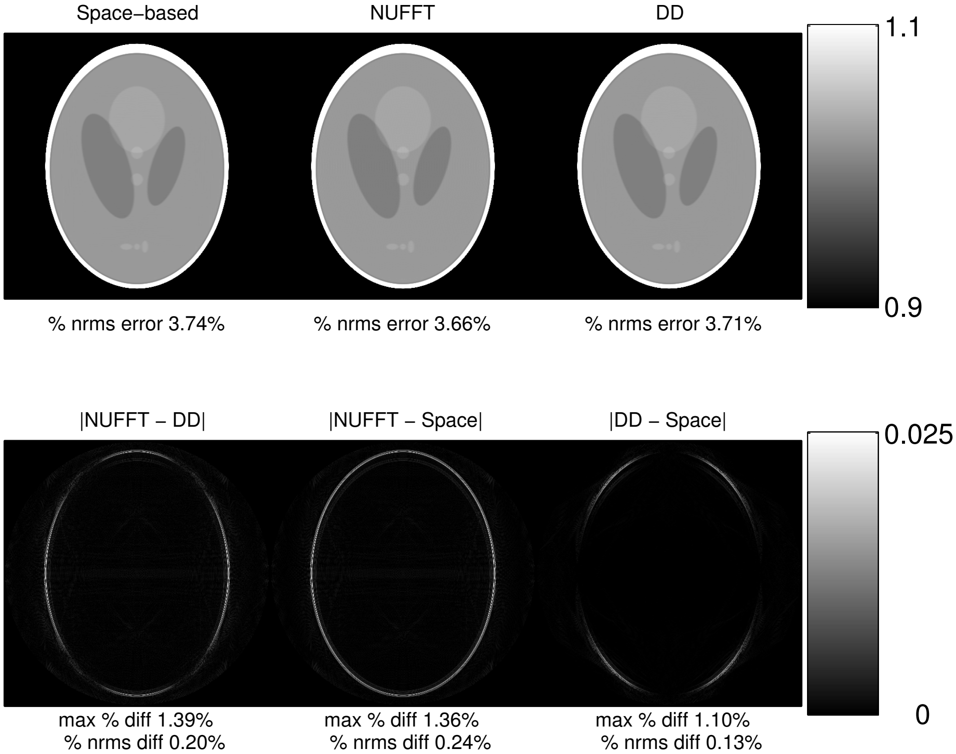

Figure 3.6: QPWLS-CG reconstruction (200 iterations) for Shepp-Logan phantom with projectors from Model 2: noiseless data, square pixels.

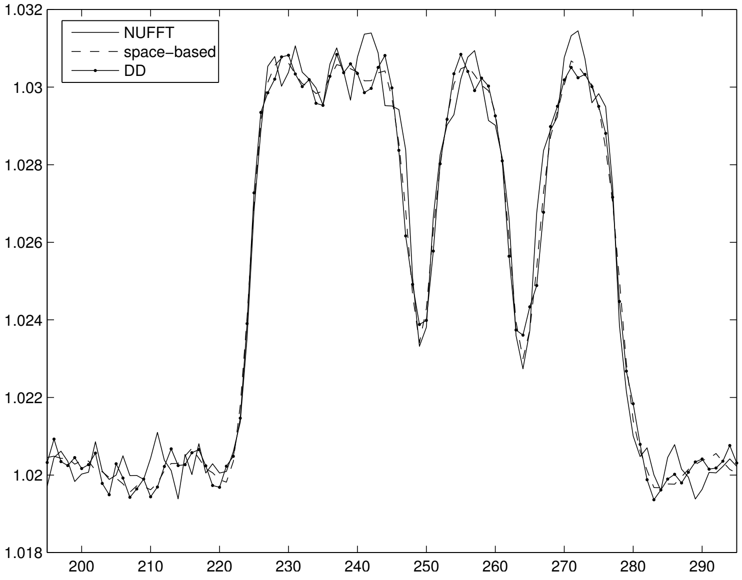

Figure 3.7: Horizontal profiles through region of interest of the reconstructed images of distance-driven, space-based and NUFFT-based methods at the 200th iteration.

Real X-Ray CT Data

We further tested the NUFFT approach within iterative reconstruction using real (noisy) CT data. Transmission data from a human shoulder phantom were acquired on a GE Lightspeed scanner. The field of view is 500mm, thus pixel size is about 1.0mm. Other parameters, such as D_{sd}, D_{s0} and the detector offset are as the same as those used in the previous noiseless data simulation. The initial image is the ramp-filtered FBP image with median filtering using a 3-by-3 neighborhood.

We ran 60 iterations of conjugate gradient algorithm for a PWLS cost function (PWLS-CG) [37]. We again use the expression in (3.22) and (3.23) except here we used an edge-preserving “hyperbola” penalty function:

$$\psi(t) = \frac{\delta^2}{3}\left(\sqrt{1 + 3(t/\delta)^2} - 1\right). \tag{3.24}$$

The regularization parameters were $\delta = 100$HU and $\alpha = 2^9$ which gives FWHM 1.7 pixels, *i.e.*, about 1.6mm. We also used the modified penalty described in [40]. We chose w_i to correspond to the 2nd derivative of the transmission Poisson log-likelihood [81].

Figure 3.8 shows the results of iterative reconstruction on real data with space-based and NUFFT-based projectors, respectively, using a standard display window width of 400 Hounsfield units (HU). The reconstructed images from the reconstruction methods with space-based and NUFFT-based projectors are again visually indistinguishable, with the max difference less than 3.4% (178.3 HU) and normalized rms around 1.0%. The largest differences were at the edges of the FOV.

This chapter has presented a NUFFT-based projection method for fan-beam tomography. This framework is an extension of parallel-beam NUFFT-based projectors. Our results show that the min-max NUFFT approach provides an accurate and efficient method for fan-beam forward and back-projection. Software is available online [36].

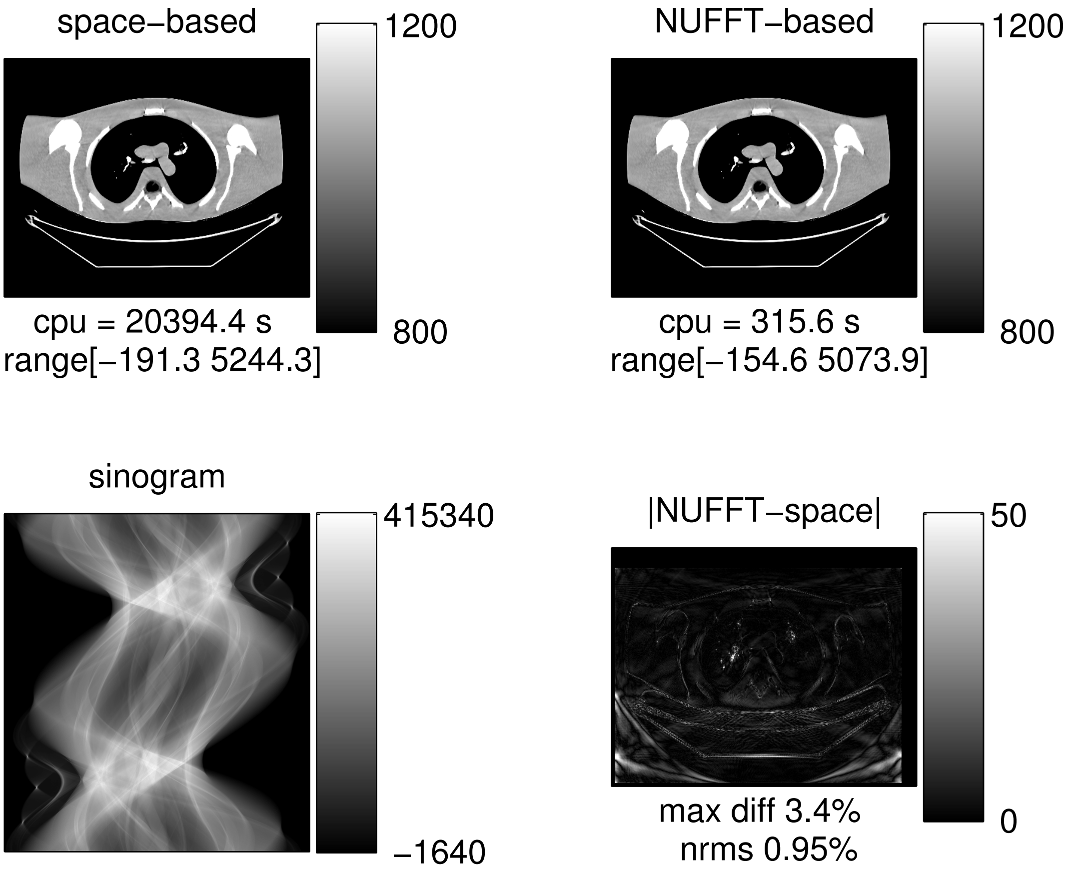

Figure 3.8: PWLS-PCG reconstruction (60 iterations) for real X-ray CT fan-beam sinogram data with projectors from Model 2.

The NUFFT-based forward and back-projectors with min-max interpolation kernels are efficient computationally compared to space-based methods, and are reasonably accurate. As expected, the computation advantage increases with larger data size (Table 3.3). The approximation error remains low even after many iterations. We have proposed this NUFFT approach for iterative fan-beam reconstruction. It is unclear how the NUFFT method could be used directly for fan-beam FBP, since that approach requires a weighted backprojection. However, one could first rebin from fan-beam to parallel-beam rays and then apply an NUFFT-type method.

3.5 Conclusion and Discussion

We have used an NUFFT method that works generally for arbitrary fan-beam sampling patterns. Further acceleration may be possible if one uses a specific 2D NUFFT approach that is tailored to the polar sampling pattern required for the Radon transform, *e.g.*, [11]. Many such methods have been proposed for direct Fourier reconstruction, *e.g.*, [13, 17, 59, 74, 96]. Presumably some of these methods could be adapted to iterative reconstruction, for both parallel-beam and fan-beam geometries. The method also can be extended to the helical cone-beam geometry.

However this method is poorly suited for “ordered-subsets” algorithms since it must compute an oversampled 2D FFT even if only a few projecton views are needed. This property limits its application to algorithms where ordered-subsets are not needed. Existing $O(N^2 \log N)$ methods also have this limitation [99].

CHAPTER 4

Analytical Noise Analysis for Fan-Beam Transmission Tomography with Quadratic Regularization [1]

Statistical image reconstruction methods offer improved resolution and noise tradeoff over conventional reconstruction methods such as FBP. However, iterative methods based on maximum-likelihood criteria often lead to very noisy reconstructed images upon convergence. There are several ways to reduce the undesirable noise: stopping the iteration long before convergence, post-filtering the convergent images, or including a roughness penalty term in the objective function. The latter is referred to as penalized-likelihood (PL) criteria. Our primary interest is penalized-likelihood image reconstruction.

Accurate predictions of image variances can be useful for reconstruction algorithm analysis and for the design of regularization methods. Computing the predicted variance at every pixel using matrix-based approximations [32] is impractical. Even most recently adopted methods that are based on local discrete Fourier approximations are impractical since they would require a forward and back-projection and two FFT calculations for every pixel, particularly for shift-variant systems like fan-beam tomography.

This chapter describes new "analytical" approaches to predicting the approximate variance maps of 2D images that are reconstructed by penalized-likelihood estimation with

---

[1] This chapter is based on material from [107].

quadratic regularization in fan-beam geometries. The simplest of the proposed analytical approaches requires computation equivalent to one back-projection and some summations, so it is computationally practical even for the data sizes in X-ray CT. Simulation results show that it gives accurate predictions of the variance maps. The parallel-beam geometry is a simple special case of the fan-beam analysis. The analysis is also applicable to 2D PET.

We start with a brief review on the matrix approximation proposed in [32] and then present an analytical variance prediction method that can be applied to any 2D tomography. Instead of working in the discrete space, we use the discrete space Fourier transform (DSFT) and Parseval's theorem to bridge from *the discrete space* to *the continuous space*. Using local shift-invariance approximations and local Fourier analysis, we derive "analytical" closed-form expressions for the local impulse response and local frequency response of the Gram operator and the regularization operator. The final approximations eliminate the need of FFTs for variance predictions, greatly reducing computation for cases where the variance is to be predicted at numerous pixel locations. Furthermore, these approximations provide insight into the resolution and noise properties of the reconstructed images.

4.1 Review of Existing Noise Analysis Methods

Statistical image reconstruction methods are usually nonlinear and shift-variant. To analyze the statistical characteristics of the reconstructed images, one would like to be able to predict the variances and covariances of estimated pixel values. The variance information provides an uncertainty measure of the reconstructed image and may aid regularization parameter selection. The existing noise analysis methods can be divided into two categories: iteration based and estimator based. The iteration-based variance predictions are studied in *e.g.*, [15,98] as a function of the iteration number for the maximum-likelihood expectation maximization algorithm based on the "stopping rule" to terminate the iterations before convergence. The estimator-based variance predictions are independent of the particular algorithm and iterations, [32,78,91]. Our proposed method falls in the estimator-based category. In this section, we give a brief overview on the existing estimator-based methods and our proposed method.

The estimator-based analysis for the mean and variance proposed in [32] uses the partial derivatives of the cost function and Taylor approximations. The approximations are in matrix form and give accurate results. However, the predictions involve the inversion of the Hessian matrices and therefore are computationally expensive. Based on this work, a great deal of effort has been given to simplify these matrix methods [78,91]. All these methods, that we refer to as the DFT approximations, are based on a factorization of the system matrix and circulant approximations to the Hessian matrices to precompute and store a great portion of the calculations. The factorization of the system matrix into geometric and object-dependent portions is specially useful for the shift-varying imaging systems. However, these DFT approximations still require in precomputation one forward and backprojection and two FFT calculations, one for likelihood Hessian and one for penalty Hessian, for each location of interest. Moreover, these expressions are still in matrix form and provide little direct insight into the noise properties.

Because our analysis is built on the previous work [32], we briefly repeat its main results here. The goal of transmission image reconstruction is to estimate an attenuation image $\mu[\vec{n}]$ from projection data $\boldsymbol{Y}$, where $\vec{n}$ is a vector denoting the 2D image pixel location. We focus here on penalized-likelihood estimators obtained by minimizing a cost function as follows:

$$\hat{\boldsymbol{\mu}} = \arg\min_{\boldsymbol{\mu}} \Phi(\boldsymbol{\mu}, \boldsymbol{Y}),$$

where $\boldsymbol{\mu} = (\mu[\vec{n}_1], \ldots, \mu[\vec{n}_p]) \in \mathbb{R}^p$ (p-dimensional real space). The cost function includes a negative log-likelihood term and a regularization term:

$$\Phi(\boldsymbol{\mu}, \boldsymbol{Y}) = -L(\boldsymbol{\mu}, \boldsymbol{Y}) + \alpha R(\boldsymbol{\mu}), \tag{4.1}$$

where α is a global regularization parameter, controlling the trade-off between the resolution and noise. As a concrete example, for transmission tomography under the Poisson noise model, the log-likelihood is

$$L(\boldsymbol{\mu}, \boldsymbol{Y}) = \sum_i Y_i \log\big(\bar{Y}_i(\boldsymbol{\mu})\big) - \bar{Y}_i(\boldsymbol{\mu}). \tag{4.2}$$

For mono-energetic transmission scans, the measurement means are modeled by

$$\bar{Y}_i(\boldsymbol{\mu}) = b_i \, \mathrm{e}^{-[\boldsymbol{A}\boldsymbol{\mu}]_i} + r_i, \tag{4.3}$$

where $\boldsymbol{A}$ is the system matrix, b_i denotes the blank scan, and r_i denotes the additive contribution of scatter to the ith ray.

We focus on regularization terms of the following form:

$$R(\boldsymbol{\mu}) = \sum_{l=1}^{4} R_l(\boldsymbol{\mu}) \tag{4.4}$$

$$R_l(\boldsymbol{\mu}) = \sum_{\vec{n}, \vec{n}-\vec{m}_l \in \mathcal{S}} r_l[\vec{n}] \frac{1}{2} \left(\mu[\vec{n}] - \mu[\vec{n} - \vec{m}_l]\right)^2, \tag{4.5}$$

where $\mathcal{S} \triangleq \{\vec{n}_j : j = 1, \ldots, p\}$ denotes the subset of the $N \times M$ lattice that is estimated and $\vec{m}_l \in \{(1,0),\ (0,1),\ (1,1),\ (-1,1)\}$. The roughness penalty (4.4) involves the horizontal, vertical, and diagonal neighbors and allows for the possibility of using regularization coefficients $\{r_l[\vec{n}]\}$ that vary both with spatial location and direction [35, 84]. In general $1 \leq p \leq NM$ and $p < NM$ because the physical field of view (FOV) is a subset of the lattice (see Figure 4.1).

The goal of this work is to approximate the covariance matrix $\mathsf{Cov}\{\hat{\boldsymbol{\mu}}\}$ efficiently yet accurately, motivated by the problem of designing the regularizer $R(\boldsymbol{\mu})$. The proposed

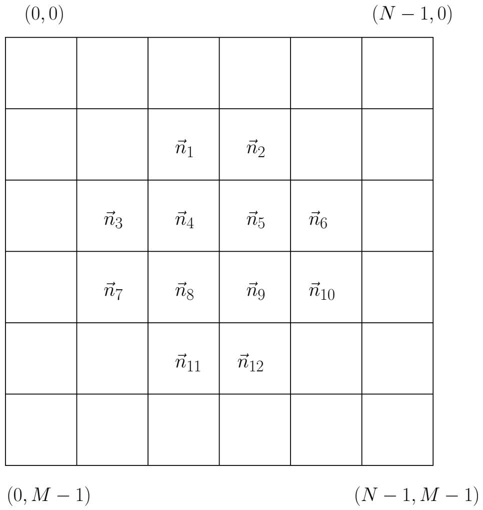

Figure 4.1: A $N \times M$ lattice with approximately circular FOV. Only the pixels with indices are estimated. In this example, $p = |\mathcal{S}| = 12$.

prediction methods can be generalized to other log-likelihood terms including 2D emission tomography by modifying $\boldsymbol{W}$ in (4.7) below. An accurate estimation of the Fisher information matrix in emission tomography is essential [61].

The following approximation to the $p \times p$ covariance matrix of $\hat{\boldsymbol{\mu}}$ was derived in [32]:

$$\boldsymbol{K} = (\boldsymbol{A}'\boldsymbol{W}\boldsymbol{A} + \alpha\boldsymbol{R})^{-1}\boldsymbol{A}' \,\mathsf{Cov}\{Y_i\}\, \boldsymbol{A}(\boldsymbol{A}'\boldsymbol{W}\boldsymbol{A} + \alpha\boldsymbol{R})^{-1}, \tag{4.6}$$

where $\boldsymbol{R}$ is the Hessian matrix of the roughness penalty. Usually, $\boldsymbol{W} \approx \mathsf{diag}\{\bar{Y}_i\}$ based on models (4.1) and (4.2). The weighting matrix $\boldsymbol{W}$ depends on the cost function we use in image reconstruction and the diagonal covariance matrix of measurements $\mathsf{Cov}\{Y_i\}$ depends on the statistical model. This general form of covariance matrix approximation (4.6) is accurate for any cost functions used in image reconstructions, provided that the measurements' second-order moments can be accurately estimated.

For transmission tomography with the simple Poisson statistical model (4.3), $\mathsf{Cov}\{Y_i\} = \mathsf{diag}\{\bar{Y}_i\}$. The approximation (4.6) becomes

$$\boldsymbol{K} = (\boldsymbol{A}'\boldsymbol{W}\boldsymbol{A} + \alpha\boldsymbol{R})^{-1}\boldsymbol{A}'\boldsymbol{W}\boldsymbol{A}(\boldsymbol{A}'\boldsymbol{W}\boldsymbol{A} + \alpha\boldsymbol{R})^{-1}, \tag{4.7}$$

In practice $\bar{Y}_i$ is unknown, so we plug in Y_i as an approximation [33]. Although we focus on (4.7) hereafter, the analysis generalizes easily to more complicated statistical models and log-likelihoods, using (4.6). The covariance between pixels $\hat{\mu}[\vec{n}_k]$ and $\hat{\mu}[\vec{n}_j]$ can be approximated using (4.7) as follows:

$$\mathsf{Cov}\{\hat{\mu}[\vec{n}_j], \hat{\mu}[\vec{n}_k]\} \approx \mathbf{e}_j' \boldsymbol{K} \mathbf{e}_k, \tag{4.8}$$

where $\mathbf{e}_j$ denotes the jth unit column vector of length p.

The matrix method described in (4.7) and (4.8) has been used in various applications [75, 91]. Simulation and experimental results have confirmed the accuracy of this covariance approximation in image regions where the non-negativity constraint is usually inactive. However, evaluating (4.8) is relatively expensive. In this chapter, we introduce "continuous space analysis" and use "local stationarity" to develop fast approximations for the variance and covariance of the reconstructed image $\hat{\mu}[\vec{n}]$.

4.2 Local Shift-Invariance Approximations

The matrix method described in (4.7) and (4.8) is very expensive to compute, even for the variance at a single pixel. To accelerate computation, local shift-invariance approximations are usually used in practice, (*e.g.*, [54,75,78,79,91]). Figure 4.2 demonstrates the idea behind local shift-invariance approximations. When two pixels are sufficiently close to each other, the local impulse responses at these pixels are similar. We state this idea mathematically in the following context.

Let $\boldsymbol{M}$ denote one of the $p \times p$ matrices in (4.7), such as $\boldsymbol{A}'\boldsymbol{W}\boldsymbol{A}$ or $\boldsymbol{R}$, or inverses or sums thereof. Then a matrix-vector operation $\boldsymbol{y} = \boldsymbol{M}\boldsymbol{x}$ can be expressed equivalently as

$$\begin{aligned} y[\vec{n}] &= \delta_{\mathcal{S}}[\vec{n}] \sum_{\vec{n}' \in \mathcal{S}} h(\vec{n}, \vec{n}')\, x[\vec{n}'] \\ &= \delta_{\mathcal{S}}[\vec{n}] \sum_{\vec{n}'} h(\vec{n}, \vec{n}')\, x[\vec{n}'] \delta_{\mathcal{S}}[\vec{n}'], \end{aligned} \tag{4.9}$$

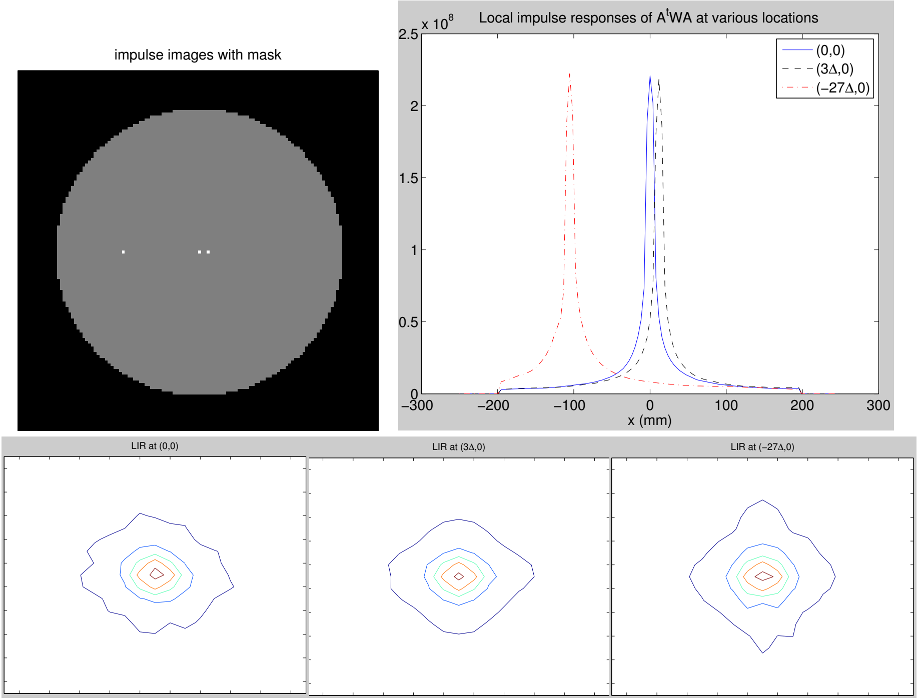

Figure 4.2: Local impulse responses (LIR) of $\boldsymbol{A}' \boldsymbol{W} \boldsymbol{A}$ at three different pixels: $(0, 0)$, $(3\Delta, 0)$ and $(-27\Delta, 0)$. The contours shown are at $95\%,\ 75\%,\ 50\%,\ 30\%,\ 15\%$ of LIR maximum.

where $\delta_{\mathcal{S}}[\vec{n}]$ is an indicator function of $\vec{n}$ defined as follows:

$$\delta_{\mathcal{S}}[\vec{n}] \triangleq \begin{cases} 1, & \vec{n} \in \mathcal{S} \\ 0, & \text{otherwise.} \end{cases} \tag{4.10}$$

In other words, the elements of $\boldsymbol{M}$ correspond to $M_{kj} = h(\vec{n}_k, \vec{n}_j)$.

Near a given location $\vec{n}_0$ of interest, we define a *local impulse response* of $\boldsymbol{M}$ as follows[2]:

$$\begin{aligned} h_0(\vec{m}) &\triangleq h(\vec{n}_0 + \lambda\vec{m}, \vec{n}_0 - (1-\lambda)\,\vec{m}) \\ & \qquad \delta_{\mathcal{S}}[\vec{n}_0 + \lambda\vec{m}]\delta_{\mathcal{S}}[\vec{n}_0 - (1-\lambda)\vec{m}], \end{aligned} \tag{4.11}$$

where $\vec{m} \in \mathbb{Z}^2$, $\mathbb{Z}$ denotes the set of integers. Usually we choose $\lambda = 1$. However, sometimes we can approximate h even for non-integer arguments, in which case $\lambda = 1/2$ may also be useful [14, p. 870].

---

[2] Throughout the paper we use the subscript “0” to indicate dependence on a given pixel location $\vec{n}_0$.

We say that $h(\vec{n}, \vec{n}')$ is locally shift invariant near $\vec{n}_0$ if $h(\vec{n}, \vec{n}') \approx h_0(\vec{n} - \vec{n}')$ for $\vec{n}$ and $\vec{n}'$ close to $\vec{n}_0$. The approximation should be accurate provided $\vec{n}$ and $\vec{n}'$ are "sufficiently close" to $\vec{n}_0$ relative to the width of h_0. Thus, if the operator $\boldsymbol{M}$ is approximately locally shift invariant near $\vec{n}_0$, then we can approximate the superposition sum (4.9) by (almost) a convolution sum:

$$y[\vec{n}] \approx \delta_{\mathcal{S}}[\vec{n}] \sum_{\vec{n}'} h_0(\vec{n} - \vec{n}')\, x[\vec{n}']\delta_{\mathcal{S}}[\vec{n}'], \tag{4.12}$$

or equivalently $\boldsymbol{y} \approx \boldsymbol{M}_0 \boldsymbol{x}$, where the $p \times p$ matrix $\boldsymbol{M}_0$ is defined by $[\boldsymbol{M}_0]_{kj} = h_0(\vec{n}_k - \vec{n}_j)$. The expression (4.12) is *almost* a convolution sum, except for the "edge conditions" of the indicator functions. If the point $\vec{n}_0$ is not "too close" to the boundaries of the support mask $\mathcal{S}$, then we may able to disregard the indicator functions and treat the expression as a convolution.

Let $\mathbf{T}$ be the $NM \times p$ matrix such that

$$\mathbf{T}_{1+n+mN,j} = \begin{cases} 1, & \vec{n}_j = (n, m) \\ 0, & \text{otherwise}, \end{cases}$$

for $n = 0, \ldots N-1$ and $m = 0, \ldots M-1$. The purpose of $\mathbf{T}$ is to embed the p elements of $\boldsymbol{\mu}$ (as shown in figure 4.1) back to the 2D $N \times M$ lattice. Then $\boldsymbol{M}_0 = \mathbf{T}' \breve{\boldsymbol{M}}_0 \mathbf{T}$, where $(\breve{\boldsymbol{M}}_0)_{\vec{n},\vec{n}'} = h_0(\vec{n} - \vec{n}')$ is an $NM \times NM$ matrix that is *block Toeplitz with Toeplitz blocks* (*BTTB*). Thus we can make a circulant approximation to $\breve{\boldsymbol{M}}_0$, ([20]). Such approximations are often reasonably accurate except near the edges of the FOV, where the differences between "Toeplitz" and "circulant" end conditions are largest. The local impulse response (4.11) and the corresponding circulant approximation are two key tools for analysis.

4.3 Variance Predictions for Fan-Beam Tomography

In the spirit of the local shift-invariance approximations presented in Section 4.2, we approximate the covariance matrix in (4.7) near a given location $\vec{n}_0$ by

$$\begin{aligned} \boldsymbol{K} &\approx \boldsymbol{K}_0 \triangleq \mathbf{T}'\breve{\boldsymbol{K}}_0\mathbf{T} \\ \breve{\boldsymbol{K}}_0 &\triangleq (\mathsf{F}_0 + \alpha\boldsymbol{R}_0)^{-1}\mathsf{F}_0(\mathsf{F}_0 + \alpha\boldsymbol{R}_0)^{-1}, \end{aligned}$$

where F_0 and $\boldsymbol{R}_0$ are the $NM \times NM$ BTTB approximations corresponding to $\boldsymbol{A}'\boldsymbol{W}\boldsymbol{A}$ and $\boldsymbol{R}$, respectively. Then we approximate the covariance between pixels $\hat{\mu}[\vec{n}]$ and $\hat{\mu}[\vec{n}']$ in (4.8) by the following inner product:

$$\mathsf{Cov}\{\hat{\mu}[\vec{n}], \hat{\mu}[\vec{n}']\} \approx \langle \breve{\boldsymbol{K}}_0 \mathbf{e}_{\vec{n}'}, \, \mathbf{e}_{\vec{n}} \rangle, \tag{4.13}$$

where $\mathbf{e}_{\vec{n}}$ is $\vec{n}$th unit vector of length NM.

Two useful approximations to (4.13) follow from Parseval's theorem. One option is to interpret the arguments in (4.12) with a suitable modulo N or M. In this case, the inner product defined in (4.13) is in the form of circulant convolution and can be approximated by FFTs:

$$\mathsf{Cov}\{\hat{\mu}[\vec{n}], \hat{\mu}[\vec{n}']\} \approx \frac{1}{NM} \sum_{\vec{k}=\vec{0}}^{\vec{N}-1} P_{d0}[\vec{k}] \, \mathrm{e}^{i\vec{\omega}_{\vec{k}} \cdot (\vec{n}-\vec{n}')}, \tag{4.14}$$

for $\vec{n}, \vec{n}' \approx \vec{n}_0$, where $\vec{N} = (N, M)$, $\vec{\omega}_{\vec{k}} = (2\pi k_1/N, 2\pi k_2/M)$ and

$$P_{d0}[\vec{k}] \triangleq \frac{\Gamma_0[\vec{k}]}{(\Gamma_0[\vec{k}] + \alpha\Omega_0[\vec{k}])^2},$$

with

$$\begin{aligned} \mathsf{F}_0 &\approx \boldsymbol{Q}\boldsymbol{\Gamma}_0\boldsymbol{Q}' \\ \boldsymbol{R}_0 &\approx \boldsymbol{Q}\boldsymbol{\Omega}_0\boldsymbol{Q}', \end{aligned}$$

where $\boldsymbol{Q}$ is the 2D (N, M)-point orthonormal DFT matrix. The diagonal matrices $\boldsymbol{\Gamma}_0$ and $\boldsymbol{\Omega}_0$ have diagonal elements $\Gamma_0[\vec{k}]$ and $\Omega_0[\vec{k}]$ that are the 2D DFT coefficients of the local impulse response of $\boldsymbol{A}'\boldsymbol{W}\boldsymbol{A}$ and $\boldsymbol{R}$ near $\vec{n}_0$, respectively. This DFT/FFT approximation has been used in [37, 78, 90] to predict variance at a single pixel:

$$\begin{aligned} \mathsf{Var}\{\hat{\mu}[\vec{n}_0]\} &\approx \langle \breve{\boldsymbol{K}}_0 \mathbf{e}_{\vec{n}},\, \mathbf{e}_{\vec{n}} \rangle \\ &\approx \frac{1}{NM} \sum_{\vec{k}=0}^{\vec{N}-1} \frac{\Gamma_0[\vec{k}]}{(\Gamma_0[\vec{k}] + \alpha\Omega_0[\vec{k}])^2}. \end{aligned} \tag{4.15}$$

Generally, evaluating this expression for a single pixel requires a forward and backprojection and two FFTs. Computation of this DFT approximation is still expensive for realistic image sizes when the variance must be computed for many or all pixels, particularly for shift-variant systems like fan-beam tomography.

An alternative option is to consider $\mu[\vec{n}]$ to be defined over all of $\mathbb{Z}^2$ (two-dimensional integer space), in which case (4.13) is in the form of ordinary convolution that can be expressed using the discrete-space Fourier transform (DSFT) as follows:

$$\mathsf{Cov}\{\hat{\mu}[\vec{n}], \hat{\mu}[\vec{n}']\} \approx \int_{-\pi}^{\pi} \int_{-\pi}^{\pi} P_{d0}(\vec{\omega})\, \mathrm{e}^{i\vec{\omega}\cdot(\vec{n}-\vec{n}')} \,\frac{\mathrm{d}\vec{\omega}}{(2\pi)^2}, \tag{4.16}$$

where $P_{d0}(\vec{\omega})$ is the local spectrum of $\breve{\boldsymbol{K}}_0$, given as follows:

$$P_{d0}(\vec{\omega}) \triangleq \frac{H_{\mathrm{d}0}(\vec{\omega})}{[H_{\mathrm{d}0}(\vec{\omega}) + \alpha R_{\mathrm{d}0}(\vec{\omega})]^2}, \tag{4.17}$$

where $H_{\mathrm{d}0}(\vec{\omega})$ is the local frequency response of the Gram matrix $\boldsymbol{A}'\boldsymbol{W}\boldsymbol{A}$ and $R_{\mathrm{d}0}(\vec{\omega})$ is the local frequency response of $\boldsymbol{R}$ near $\vec{n}_0$. To our knowledge, this paper is the first to use (4.16) to develop analytical variance approximations as a faster alternative to the DFT approach (4.15).

For regularizer design, the standard deviation map of the reconstructed image is one quantity of interest, and our numerical investigation will focus on variance prediction. However, the methodology applies readily to approximate covariances.

Using the DSFT approximation (4.16), we approximate the variance at pixel $\vec{n}_0$ as follows:

$$\mathsf{Var}\{\hat{\mu}[\vec{n}_0]\} \approx \int_{-\pi}^{\pi}\int_{-\pi}^{\pi} P_{d0}(\vec{\omega})\frac{\mathrm{d}\vec{\omega}}{(2\pi)^2}. \tag{4.18}$$

Let Δ denote the sample spacing in the reconstructed image. By making the change of variable, $\vec{\omega} = (2\pi\rho\Delta)\vec{e}_\Phi$ where $\vec{e}_\Phi \triangleq (\cos\Phi, \sin\Phi)$, we rewrite (4.18) in terms of polar frequency coordinates (ρ, Φ) as follows:

$$\mathsf{Var}\{\hat{\mu}[\vec{n}_0]\} \approx \Delta^2 \int_0^{2\pi}\int_0^{\rho_{\max}(\Phi)} P_0(\rho, \Phi)\rho \,\mathrm{d}\rho \,\mathrm{d}\Phi, \tag{4.19}$$

where $\rho_{\max}(\Phi) = \frac{1}{2\Delta\max\{|\cos\Phi|,|\sin\Phi|\}}$, and we define

$$P_0(\rho, \Phi) \triangleq P_{\mathrm{d}0}(2\pi\rho\Delta\vec{e}_\Phi) = \frac{H_0(\rho, \Phi)}{[H_0(\rho, \Phi) + \alpha R_0(\rho, \Phi)]^2}. \tag{4.20}$$

We defined H_0 and R_0 similarly in terms of $H_{\mathrm{d}0}$ and $R_{\mathrm{d}0}$. The variance prediction (4.19) applies to any 2D geometry with appropriate local frequency responses $H_0(\rho, \Phi)$ and $R_0(\rho, \Phi)$. We will specialize (4.19) by finding $H_0(\rho, \Phi)$ for fan-beam geometry and $R_0(\rho, \Phi)$ for quadratic regularization.

4.4 "Pure" Analytical Variance Predictions for Ideal Fan-Beam Tomography

We first present a "pure" analytical analysis in continuous space for an ideal fan-beam scanner that has infinitesimal beams and zero-width detectors. In this ideal case, the system operator $\boldsymbol{\mathcal{A}}$ is the continuous counterpart of the system matrix $\boldsymbol{A}$ in (2.11) and is same as the fan-beam projection operator $\boldsymbol{\mathcal{P}}$.

The result developed under this idealized situation is not practical but served as a natural starting point of and provides first intuition on the noise properties of the fan-beam tomography.

4.4.1 Local Frequency Response of The Gram Operator

The linear operator $\boldsymbol{\mathcal{A}}$ transforms a signal $f(x,y)$ in image space into a signal $p(s,\beta)$ in fan-beam projection space:

$$p(s,\beta) \triangleq (\boldsymbol{\mathcal{A}}f)(s,\beta) = \int_{-\infty}^{\infty} f(x,y)\delta(x\cos\varphi(s,\beta) + y\sin\varphi(s,\beta) - r(s))\,\mathrm{d}x\,\mathrm{d}y\,.$$

The usual inner product for fan-beam projection space is given as the following:

$$\langle p_1,\, p_2\rangle = \int_{-s_{\max}}^{s_{\max}} \int_0^{\beta_{\max}} p_1(s,\beta)\, p_2(s,\beta)\,\mathrm{d}s\,\mathrm{d}\beta, \tag{4.21}$$

where $p_1(s,\beta)$ and $p_2(s,\beta)$ are two signals in fan-beam projection space. This is the natural inner product when considering the usual case of samples that are equally-spaced in the arc length s and in source angle β for equiangular case. The parallel-fan relationships are given in (3.18) and (3.19). For convenience, we repeat the results here with slightly different notations:

$$r(s) = D_{\mathrm{s0}} \sin\gamma(s) \tag{4.22}$$

$$\varphi(s,\beta) = \beta + \gamma(s), \tag{4.23}$$

where D_{s0} is the source to rotation center distance and $\gamma(s)$ is the angle of the ray relative to the source. $\gamma(s) = s/D_{\mathrm{sd}}$ for equiangular case and $\gamma(s) = \arctan(s/D_{\mathrm{sd}})$ for equidistant case. We consider equiangular case only here.

For the inner product (4.21), the adjoint of $\boldsymbol{\mathcal{P}}$ is given by

$$(\boldsymbol{\mathcal{P}}^* p)(x,y) = \int_{-s_{\max}}^{s_{\max}} \int_0^{\beta_{\max}} \delta(x\cos\varphi(s,\beta) + y\sin\varphi(s,\beta) - r(s))\, p(s,\beta)\,\mathrm{d}s\,\mathrm{d}\beta\,.$$

To analyze the impulse response of the Gram operator $\boldsymbol{\mathcal{P}}^*\boldsymbol{\mathcal{W}}\boldsymbol{\mathcal{P}}$, consider an impulse object $\delta_0(x,y) = \delta(x - x_0, y - y_0)$ as follows:

$$\begin{aligned} h(x,y;x_0,y_0) &= (\boldsymbol{\mathcal{P}}^*\boldsymbol{\mathcal{W}}\boldsymbol{\mathcal{P}}\,\delta_0)\,(x,y) \\ &= \int_0^{2\pi} \int_{-s_{\max}}^{s_{\max}} \delta(x\cos\varphi(s,\beta) + y\sin\varphi(s,\beta) - r(s)) \\ &\quad \cdot \delta(x_0\cos\varphi(s,\beta) + y_0\sin\varphi(s,\beta) - r(s))\, w(s,\beta)\,\mathrm{d}s\,\mathrm{d}\beta\,. \end{aligned} \tag{4.24}$$

We assume hereafter that $w(s,\beta)$ is chosen such that $w(s,\beta) = 0$ when $\beta > \beta_{\max}$. Thus we can assume $\beta_{\max} = 2\pi$ for the analysis, yet the results are still applicable to "short" scans provided $w(s,\beta)$ is chosen appropriately. For convenience, we express the point (x_0, y_0) in polar coordinates (r_0, φ_0). Now make the change of variables $r' = D_{\mathrm{s0}} \sin\gamma(s),\ \varphi' = \beta + \gamma(s)$, the impulse response in (4.24) becomes

$$\begin{aligned} h(x,y;x_0,y_0) &= \int_0^{2\pi}\int_{-r_{\max}}^{r_{\max}} \delta(x\cos\varphi' + y\sin\varphi' - r')\,\delta(r_0\cos(\varphi'-\varphi_0) - r') \\ &\qquad\qquad \cdot w(s(r'),\beta(r',\varphi'))\,J(r')\,\mathrm{d}r'\,\mathrm{d}\varphi' \\ &= \int_0^{2\pi} \delta(x\cos\varphi' + y\sin\varphi' - r_0')\,\bar{w}(r_0(\varphi'),\varphi')J(r_0(\varphi'))\ 1_{\{|r_0(\varphi')|\le r_{\max}\}}\,\mathrm{d}\varphi', \end{aligned}$$

where $J(r)$ is the determinant of the Jacobian matrix of transforming from the fan-beam coordinates to parallel-beam coordinates and $\bar{w}(r,\varphi)$ is rebinned $w(s,\beta)$ in parallel coordinates:

$$\begin{aligned} J(r) &= \left|\frac{D_{\mathrm{sd}}^2}{\arcsin(r/D_{\mathrm{s0}})}\right| \\ \bar{w}(r,\varphi) &= w(s(r),\beta(r,\varphi)) \\ r_0(\varphi') &= r_0\cos(\varphi'-\varphi_0) \\ s(\varphi') &= D_{\mathrm{sd}}\arcsin\left(\frac{r_0(\varphi')}{D_{\mathrm{s0}}}\right) \\ \beta' &= \varphi' - \arcsin\left(\frac{r_0'}{D_{\mathrm{s0}}}\right). \end{aligned} \tag{4.25}$$

We focus on locations within the field of view (FOV) where $r_0 \le r_{\max} \triangleq D_{\mathrm{s0}}\sin\gamma(s_{\max})$. In the spirit of local shift invariance, $x \approx x_0 + r\cos\varphi$ and $y \approx y_0 + r\sin\varphi$. Consider the following local impulse response:

$$\begin{aligned} h_0(r,\varphi) &\triangleq h(x_0 + r\cos\varphi,\ y_0 + r\sin\varphi;\ x_0, y_0) \\ &= \int_0^{2\pi} \delta(r\cos(\varphi-\varphi'))\,\bar{w}(r_0(\varphi'),\varphi')J(r_0(\varphi'))\,\mathrm{d}\varphi' \\ &= \frac{1}{|r|}\left[\bar{w}(r_0(\varphi'),\varphi')J(r_0(\varphi'))\Big|_{\varphi'=\varphi+\frac{\pi}{2}} + \bar{w}(r_0(\varphi'),\varphi')J(r_0(\varphi'))\Big|_{\varphi'=\varphi-\frac{\pi}{2}}\right], \end{aligned} \tag{4.26}$$

Thus, for the fan-beam case the local impulse response of the Gram operator is

$$h_0(r,\varphi) = \frac{1}{|r|} w_0(\varphi + \pi/2), \tag{4.27}$$

where the angular-dependent weighting is

$$w_0(\varphi) \triangleq \bar{w}(r_0(\varphi'),\varphi') J(r_0(\varphi'))\Big|_{\varphi'=\varphi} + \bar{w}(r_0(\varphi'),\varphi') J(r_0(\varphi'))\Big|_{\varphi'=\varphi-\pi}. \tag{4.28}$$

The local impulse response $h_0(r,\varphi)$ is in form of $\frac{1}{r}$ that decays rapidly with the increase of the distance r with respect to the location (x_0, y_0).

We can obtain the local frequency response of the Gram operator by taking local Fourier transform of $h_0(r,\varphi)$ in (4.27):

$$\begin{aligned}
H_0(\rho,\Phi) &= \int_0^\pi \int_{-\infty}^{\infty} h_0(r,\varphi)\, \mathrm{e}^{-\imath 2\pi r\rho\cos(\varphi-\Phi)}\, |r|\, \mathrm{d}r\, \mathrm{d}\varphi \\
&= \int_0^\pi w_0(\varphi+\pi/2) \int_{-\infty}^{\infty} \delta(\rho\cos(\varphi-\Phi))\, \mathrm{d}\varphi \\
&= \frac{1}{|\rho|} \int_0^\pi w_0(\varphi')\, \delta(\sin(\varphi'-\Phi))\, \mathrm{d}\varphi' \\
&= \frac{w_0(\Phi)}{|\rho|},
\end{aligned} \tag{4.29}$$

where $w_0(\Phi)$ is a location-dependent angular weighting function.

4.4.2 Local Frequency Response of Quadratic Regularization Operator

Analogous to the discrete-space regularization (4.4) in Section 4.1, natural approaches to quantify the continuous-space roughness involve the derivatives of the image $\mu(x,y)$. Define $\boldsymbol{\mathcal{D}}_{\phi_\ell}$ to be the differentiation operator along direction $[\cos\phi_\ell \;\sin\phi_\ell]^T$:

$$(\boldsymbol{\mathcal{D}}_{\phi_\ell}\,\mu)(x,y) = \sqrt{r_{l,0}} \left(\cos\phi_\ell \frac{\partial}{\partial x} + \sin\phi_\ell \frac{\partial}{\partial y}\right)^m \mu(x,y),$$

where $r_{l,0}$ is a user-designed weight along direction $[\cos\phi_\ell \;\sin\phi_\ell]^T$. Usually, $m = 1$ or 2. For the usual $\mathcal{L}_2$ norm we have

$$\|\boldsymbol{\mathcal{D}}_{\phi_\ell}\,\mu\|^2 = \iint \left| \sqrt{r_{l,0}} \left(\cos\phi_\ell \frac{\partial}{\partial x} + \sin\phi_\ell \frac{\partial}{\partial y}\right)^m \mu \right|^2 \mathrm{d}x\,\mathrm{d}y,$$

These norms quantify the roughness of μ. (To use such semi-norms we must restrict attention to the subspace of functions with square integrable derivatives.) We can write this differentiation operator in frequency domain:

$$\begin{aligned}\boldsymbol{\mathcal{D}}_{\phi_\ell} &= \boldsymbol{\mathcal{F}}_2^{-1}\boldsymbol{\mathcal{D}}\big(\sqrt{r_{l,0}}(\imath 2\pi u\cos\phi_\ell + \imath 2\pi v \sin\phi_\ell)^m\big)\,\boldsymbol{\mathcal{F}}_2\\ &= \boldsymbol{\mathcal{F}}_2^{-1}\boldsymbol{\mathcal{D}}\big((\imath 2\pi\rho)^m\sqrt{r_{l,0}}(\cos\Phi\cos\phi_\ell+\sin\Phi\sin\phi_\ell)^m\big)\boldsymbol{\mathcal{F}}_2\\ &= \boldsymbol{\mathcal{F}}_2^{-1}\boldsymbol{\mathcal{D}}\big((\imath 2\pi\rho)^m\sqrt{r_{l,0}}\cos^m(\Phi-\phi_\ell)\big)\,\boldsymbol{\mathcal{F}}_2, \qquad (4.30)\end{aligned}$$

where $(u = \rho\cos\Phi, v = \rho\sin\Phi)$ denotes the frequency domain Cartesian coordinates. The adjoint operator of $\boldsymbol{\mathcal{D}}_{\phi_\ell}$ can be easily obtained for the usual inner product in $\mathcal{L}_2(\mathbb{R}^2)$:

$$\boldsymbol{\mathcal{D}}^*_{\phi_\ell} = \boldsymbol{\mathcal{F}}_2^{-1}\,\boldsymbol{\mathcal{D}}\big((-\imath 2\pi\rho)^m\sqrt{r_{l,0}}\cos^m(\Phi-\phi_\ell)\big)\,\boldsymbol{\mathcal{F}}_2. \qquad (4.31)$$

We can show from (4.30) and (4.31) that

$$\boldsymbol{\mathcal{D}}^*_{\phi_\ell}\,\boldsymbol{\mathcal{D}}_{\phi_\ell} = \boldsymbol{\mathcal{F}}_2^{-1}\,\boldsymbol{\mathcal{D}}\big((2\pi\rho)^{2m}\cdot r_{l,0}\cos^{2m}(\Phi-\phi_\ell)\big)\,\boldsymbol{\mathcal{F}}_2.$$

Then we define the following regularization operator:

$$\boldsymbol{\mathcal{R}} \triangleq \sum_{\ell=1}^{L}(\boldsymbol{\mathcal{D}}^*_{\phi_\ell}\,\boldsymbol{\mathcal{D}}_{\phi_\ell}) = \boldsymbol{\mathcal{F}}_2^{-1}R_0(\rho,\Phi)\boldsymbol{\mathcal{F}}_2,$$

where the frequency response of $\boldsymbol{\mathcal{R}}$ is separable in ρ and Φ:

$$R_0(\rho,\Phi) = (2\pi\rho)^{2m}\sum_{\ell=1}^{L} r_{l,0}\cos^{2m}(\Phi-\phi_\ell) = (2\pi\rho)^{2m}\tilde{R}_0(\Phi), \qquad (4.32)$$

with angular-dependent regularization

$$\tilde{R}_0(\Phi) \triangleq \sum_{\ell=1}^{L} r_{l,0}\cos^{2m}(\Phi-\phi_\ell)\,. \qquad (4.33)$$

Consider the usual quadratic regularization design where $m = 1$ for the first-order derivatives: $R(\rho,\Phi) = C_R(2\pi\rho)^2\tilde{R}_j(\Phi)$.The variance approximation becomes

$$\begin{aligned}\mathsf{Var}\{\hat{\mu}_0\} &\approx \int_0^{2\pi}\int_0^{\rho_{\max}} \frac{w_0(\Phi)/\,|\rho|}{\left(\frac{w_0(\Phi)}{|\rho|} + \alpha(2\pi\rho)^2\tilde{R}_j(\Phi)\right)^2}\rho\,\mathrm{d}\rho\,\mathrm{d}\Phi\\ &= \frac{1}{3}\int_0^{2\pi}\frac{1}{\left[w_0(\Phi)/\rho_{\max}^3 + \alpha 4\pi^2\tilde{R}_0(\Phi)\right]}\,\mathrm{d}\Phi, \qquad (4.34)\end{aligned}$$

where $\hat{\mu}_0 \triangleq \hat{\mu}(x_0, y_0)$ and the inner integral over ρ can be computed analytically. The angular-dependent weighting function $w_0(\Phi)$ is equivalent to one back-projection. The approximation (4.34) is not accurate for realistic fan-beam CT, however it agrees with one version of our practical derivation in next section, the SI approximation in (4.71).

4.5 Fast Variance Predictions for Non-Ideal Fan-Beam Transmission Tomography

In this section, we conduct a different analysis on local frequency responses of Gram matrix and quadratic regularization in fan-beam tomography. The analysis takes into account of the discretization effect and gives closed-form expression for $P_0(\rho, \Phi)$. With these results, the variance prediction in (4.19) is practical and accurate for implementation.

The following analysis is focused on equiangular fan-beam transmission tomography with an arc detector. However, the method generalizes readily to flat detectors, *i.e.*, equidistant sampling and to parallel-beam geometries.

4.5.1 Analysis For Fan-Beam Gram Matrix

To accurately predict variance images in realistic fan-beam transmission tomography using (4.19), we need to determine the local frequency response $H_0(\rho, \Phi)$, or equivalently $H_{\mathrm{d}0}(\vec{\omega})$. We first find the local impulse response.

Local Impulse Response

Consider the 2D object model based on a common basis function $\chi(\vec{x})$ superimposed on a $N \times M$ Cartesian grid as follows:

$$\mu(\vec{x}) = \sum_{\vec{n} \in \mathcal{S}} \mu[\vec{n}] \, \chi\left(\frac{\vec{x} - \vec{x}_c[\vec{n}]}{\Delta} \right), \tag{4.35}$$

where $\vec{x} \in \mathbb{R}^2$ denotes the 2D coordinates of the continuous image space, and $\vec{x}_c[\vec{n}]$ denotes the center of the basis function. Typically

$$\begin{aligned} \vec{x}_c[\vec{n}] &= (\vec{n} - \vec{w}_{\vec{x}})\Delta, \quad \vec{n} \in \mathcal{S} \\ \vec{w}_{\vec{x}} &= (\vec{N} - \vec{1})/2 + \vec{c}_{\vec{x}}, \end{aligned}$$

where $\vec{N} = (N, M)$ and the user-selectable parameter $\vec{c}_{\vec{x}}$ denotes an optional spatial offset for the image center.

For simplicity, we assume here that the detector blur $b(s)$ is locally shift invariant, independent of source position β, and acts only along the s coordinate. Then we model the mean projections as follows:

$$\bar{y}_\beta[s_k] = \int b(s_k - s')\, p_{\tilde{\varphi}(s',\beta)}(r(s'))\, \mathrm{d}s' \tag{4.36}$$

for $s_k = (k - w_{\mathrm{S}})\Delta_{\mathrm{S}}$ and $k = 1, \ldots, n_s$, where Δ_{S} is the sample spacing in s, w_{S} is defined akin to $\vec{w}_{\vec{x}}$, and $p_\varphi(r)$ is the 2D Radon transform of $\mu(\vec{x})$:

$$p_\varphi(r) = \int \mu(r\cos\varphi - \ell\sin\varphi, r\sin\varphi + \ell\cos\varphi)\, \mathrm{d}\ell\,.$$

Substituting the basis expansion model in (4.35) for the object into the measurement model (4.36) and simplifying leads to the linear model

$$\bar{y}_\beta[s_k] = \sum_{\vec{n} \in \mathcal{S}} a(s_k, \beta; \vec{n}) \mu[\vec{n}],$$

where the fan-beam system matrix elements are samples of the following fan-beam projection of a single basis function centered at $\vec{x}_c[\vec{n}]$:

$$a(s, \beta; \vec{n}) = \int b(s - s')\, \Delta\, g\left(\frac{r(s') - r_{\varphi(s',\beta)}[\vec{n}]}{\Delta}, \varphi(s', \beta)\right) \mathrm{d}s', \tag{4.37}$$

where $g(\cdot, \varphi)$ is the Radon transform of $\chi(\vec{x})$ at angle φ and

$$r_\varphi[\vec{n}] \triangleq \vec{x}_c[\vec{n}] \cdot \vec{e}_\varphi,$$

with $\vec{e}_\varphi \triangleq (\cos\varphi, \sin\varphi)$.

Then the elements of the *Gram matrix* are given exactly by

$$\begin{aligned} h_{\mathrm{d}}[\vec{n};\vec{n}'] &= \begin{cases} [\boldsymbol{A}'\boldsymbol{W}\boldsymbol{A}]_{jj'}, & \vec{n}=\vec{n}_j \in \mathcal{S}, \vec{n}'=\vec{n}_{j'} \in \mathcal{S} \\ 0, & \text{otherwise} \end{cases} \\ &= \breve{h}_{\mathrm{d}}[\vec{n};\vec{n}']\eta(\vec{x}_c[\vec{n}])\eta(\vec{x}_c[\vec{n}']) \end{aligned} \tag{4.38}$$

where $\eta(\vec{x}_c[\vec{n}]) \triangleq 1_{\{\vec{n}\in\mathcal{S}\}}$,

$$\breve{h}_{\mathrm{d}}[\vec{n};\vec{n}'] \triangleq \sum_{l=1}^{n_{\mathrm{A}}}\sum_{k=1}^{n_s} w(s_k,\beta_l)\, a(s_k,\beta_l;\vec{n})a(s_k,\beta_l;\vec{n}') \tag{4.39}$$

and $w(s,\beta)$ denotes the weighting associated with $\boldsymbol{W}$ and n_{A} denotes the number of samples of the source position β. To simplify (4.38), we first use an *integral* to approximate the summation in (4.39) as follows:

$$\breve{h}_{\mathrm{d}}[\vec{n};\vec{n}'] \approx \frac{1}{\Delta_\beta}\frac{1}{\Delta_{\mathrm{S}}}\int_0^{2\pi}\int_{-\infty}^{\infty} w(s,\beta)\, a(s,\beta;\vec{n})a(s,\beta;\vec{n}')\mathrm{d}s\,\mathrm{d}\beta, \tag{4.40}$$

where Δ_β is the source angular sampling interval. Notice that $\breve{h}_{\mathrm{d}}[\vec{n};\vec{n}']$ in (4.40) is not shift invariant.

We develop locally shift-invariant approximations to $\breve{h}_{\mathrm{d}}[\vec{n};\vec{n}']$ in (4.40) by re-parameterizing variables s, β using analogs of fan-to-parallel beam rebinning. Reparameterize variables s and β in (4.40) according to the inversion of (4.22) and (4.23):

$$\begin{aligned} s \longrightarrow \tilde{s}(r) &= D_{\mathrm{sd}} \arcsin(r/D_{\mathrm{s0}}) \\ \beta \longrightarrow \tilde{\beta}(r,\varphi) &= \varphi - \arcsin(r/D_{\mathrm{s0}})\,. \end{aligned}$$

Then the fan-to-parallel beam rebinning of $a(s,\beta;\vec{n})$ is

$$\begin{aligned} a(\tilde{s}(r),\tilde{\beta}(r,\varphi);\vec{n}) &\approx \int b(\tilde{s}(r)-\tilde{s}(r'))\,\Delta\, g\left(\frac{r'-r_\varphi[\vec{n}]}{\Delta},\varphi\right)\left|\dot{\tilde{s}}(r')\right|\mathrm{d}r', \\ &\triangleq a(r,\varphi;\vec{n}) \end{aligned} \tag{4.41}$$

because $r(\tilde{s}(r')) = r'$ and $\tilde{\varphi}(\tilde{s}(r'), \tilde{\beta}(r,\varphi)) \approx \varphi$ for $r \approx r'$.

A first-order Taylor expansion of $\tilde{s}(r)$ around r' yields

$$\tilde{s}(r) - \tilde{s}(r') \approx \dot{\tilde{s}}(r')(r - r').$$

Substituting into (4.41), the system matrix elements become

$$a(r, \varphi; \vec{n}) \approx \int b\big(\dot{\tilde{s}}(r')(r - r')\big)\, \Delta\, g\bigg(\frac{r' - r_\varphi[\vec{n}]}{\Delta}, \varphi\bigg) \left|\dot{\tilde{s}}(r')\right| \mathrm{d}r' \,. \tag{4.42}$$

Substituting (4.42) into (4.40) and changing variables from (s, β) to (r, φ) using (4.22) and (4.23) yields the local impulse approximation,

$$\begin{aligned} \breve{h}_{\mathrm{d}}[\vec{n}; \vec{n}'] &\approx \frac{1}{\Delta_\beta} \frac{1}{\Delta_{\mathrm{S}}} \int_0^{2\pi}\!\!\int_{-\infty}^{\infty} \bar{w}(r,\varphi) a(r,\varphi;\vec{n}) a(r,\varphi;\vec{n}') \left|J(r)\right| \mathrm{d}r \,\mathrm{d}\varphi \\ &= \frac{1}{\Delta_\beta} \frac{1}{\Delta_{\mathrm{S}}} \int_0^{2\pi} \breve{w}(\varphi;\vec{n};\vec{n}') \breve{h}_\varphi[\vec{n};\vec{n}'] \,\mathrm{d}\varphi, \end{aligned} \tag{4.43}$$

where $|J(r)| = \left|\dot{\tilde{s}}(r)\right|$ is the determinant of Jacobian matrix, and

$$\begin{aligned} \breve{h}_\varphi[\vec{n};\vec{n}'] &\triangleq \int_{-\infty}^{\infty} a(r - r_\varphi[\vec{n}], \varphi; \vec{n})\, a(r - r_\varphi[\vec{n}'], \varphi; \vec{n}')\,\mathrm{d}r \\ \breve{w}(\varphi;\vec{n};\vec{n}') &\triangleq \frac{\int_{-\infty}^{\infty} \bar{w}(r,\varphi) \left|J(r)\right| a(r - r_\varphi[\vec{n}], \varphi)\, a(r - r_\varphi[\vec{n}'], \varphi)\,\mathrm{d}r}{\int_{-\infty}^{\infty} a(r - r_\varphi[\vec{n}], \varphi)\, a(r - r_\varphi[\vec{n}'], \varphi)\,\mathrm{d}r} \\ \bar{w}(r,\varphi) &\triangleq w(\tilde{s}(r), \tilde{\beta}(r,\varphi)). \end{aligned} \tag{4.44}$$

Let $r_0(\varphi) \triangleq r_\varphi[\vec{n}_0]$. Because $\dot{\tilde{s}}(r)$ is fairly smooth, we make the following approximation for $r' \approx r_0(\varphi)$:

$$\dot{\tilde{s}}(r') \approx \dot{\tilde{s}}(r_0(\varphi)) \triangleq m_0(\varphi) \,. \tag{4.45}$$

Substituting (4.45) into (4.42) and simplifying yields

$$\begin{aligned} a(r,\varphi;\vec{n}) &\approx a(r,\varphi;\vec{n}_0) \triangleq a_0(r,\varphi) \\ &= \int b_0(r - r_\varphi[\vec{n}] - r'', \varphi) \Delta g\bigg(\frac{r''}{\Delta}, \varphi\bigg) \mathrm{d}r'', \end{aligned} \tag{4.46}$$

with $r'' = r' - r_\varphi[\vec{n}]$ and

$$b_0(r,\varphi) \triangleq m_0(\varphi)\, b(m_0(\varphi)\, r)\,. \tag{4.47}$$

Therefore, we further simply (4.43) as follows

$$\breve{h}_{\mathrm{d}}[\vec{n};\vec{n}'] \approx \frac{1}{\Delta_\beta}\frac{1}{\Delta_{\mathrm{S}}} \int_0^{2\pi} w_0(\varphi) \breve{h}_0(\Delta(\vec{n}-\vec{n}')\cdot\vec{e}_\varphi,\varphi)\,\mathrm{d}\varphi, \tag{4.48}$$

where because $\bar{w}(r,\varphi)$ often varies slowly in r relative to the typically sharp peak of $a_0(r,\varphi)$ at $r=0$,

$$\begin{aligned}
\breve{h}_0(r,\varphi) &\triangleq a_0(r,\varphi) \star a_0(r,\varphi), \\
\breve{w}(\varphi;\vec{n};\vec{n}') &\approx \frac{\int_{-\infty}^{\infty} \bar{w}(r,\varphi)\,|m_0(\varphi)|\, a_0^2(r - r_\varphi[\vec{n}_0],\varphi)\,\mathrm{d}r}{\int_{-\infty}^{\infty} a_0^2(r - r_\varphi[\vec{n}_0],\varphi)\,\mathrm{d}r} \\
&\approx |m_0(\varphi)|\,\bar{w}(r_0(\varphi),\varphi) \triangleq w_0(\varphi),
\end{aligned} \tag{4.49}$$

where $\star$ denotes a 1D autocorrelation with respect to r and $a_0(r,\varphi)$ is a locally parallel-beam version of the system model defined in (4.46).

The angle-dependent weighting $w_0(\varphi)$ is associated with pixel $\vec{n}_0$, accounting for the position-dependent magnification as follows:

$$w_0(\varphi) \triangleq |m_0(\varphi)|\, w(s(r_0(\varphi)), \beta(r_0(\varphi),\varphi)) \tag{4.50}$$

$$\begin{aligned}
r_0(\varphi) &\triangleq r_\varphi[\vec{n}_0] \\
m_0(\varphi) &\triangleq \frac{\partial}{\partial r} s(r)\bigg|_{r=r_0(\varphi)} = \frac{D_{\mathrm{sd}}/D_{\mathrm{s0}}}{\sqrt{1-(r_0(\varphi)/D_{\mathrm{s0}})^2}},
\end{aligned} \tag{4.51}$$

where $s(r)$ and $\beta(r,\varphi)$ are the inverse of (4.22) and (4.23). The local impulse response of Gram matrix has the following almost shift invariant form:

$$h_{\mathrm{d}}[\vec{n};\vec{n}'] \approx \frac{\eta(\vec{x}_c[\vec{n}])\eta(\vec{x}_c[\vec{n}'])}{\Delta_\beta \Delta_{\mathrm{S}}} \int_0^{2\pi} w_0(\varphi) \breve{h}_0(\Delta(\vec{n}-\vec{n}')\cdot\vec{e}_\varphi,\varphi)\,\mathrm{d}\varphi\,. \tag{4.52}$$

The shape of $\breve{h}_{\mathrm{d}}[\vec{n};\vec{n}']$ in (4.48) is a modification of 1/r (cf [71]) with statistically modulated angular weighting. The key property of (4.52) is that it is locally shift invariant, except for edge effects. This approximation should be reasonably accurate provided that $\vec{n}$ and $\vec{n}'$ are "sufficiently close" to $\vec{n}_0$, the coordinates of the pixel of interest.

Now we apply the local shift-invariance approximation to (4.52). One way is to use the coordinate transformation recommended for analyzing quasi-stationary noise in [14, p. 870] as follows:

$$\begin{aligned}\tilde{h}_\varphi[\vec{n};\vec{n}_0] &\triangleq h_\varphi[\vec{n}_0+\vec{n}/2;\vec{n}_0-\vec{n}/2]\\ &= \breve{h}_0(\Delta\vec{n}\cdot\vec{e}_\varphi,\varphi)\eta_2(\Delta\vec{n}),\end{aligned}$$

where $\vec{x}_0 \triangleq \vec{x}_c[\vec{n}_0]$, and η_1 denotes the support of the image,

$$\eta_1(\vec{x}) \triangleq \eta(\vec{x}_0+\vec{x}/2)\eta(\vec{x}_0-\vec{x}/2). \tag{4.53}$$

This approach yields a local impulse response that is symmetric in $\vec{n}$, thus ensuring that its spectrum is real.

Another alternative is to refer all displacements relative to the point $\vec{n}_0$ as follows:

$$\begin{aligned}\tilde{h}_\varphi[\vec{n};\vec{n}_0] &\triangleq h_\varphi[\vec{n}_0+\vec{n};\vec{n}_0]\\ &= \breve{h}_0(\Delta\vec{n}\cdot\vec{e}_\varphi,\varphi)\eta_2(\Delta\vec{n}),\end{aligned}$$

where

$$\eta_2(\vec{x}) \triangleq \eta(\vec{x}_0+\vec{x})\eta(\vec{x}_0). \tag{4.54}$$

This choice is not symmetric in $\vec{n}$ but it better corresponds to the local Fourier analysis based on the DFT of $\boldsymbol{A}'\boldsymbol{W}\boldsymbol{A}\mathbf{e}_j$.

By referring all displacements relative to the point $\vec{n}_0$, we can obtain the final form of local impulse response:

$$h_\mathrm{d}[\vec{n};\vec{n}'] \approx \frac{1}{\Delta_\beta\Delta_\mathrm{s}}\int_0^{2\pi} w_0(\varphi)\, s_{\varphi,0}(\Delta\vec{n}\cdot\vec{e}_\varphi)\,\mathrm{d}\varphi, \tag{4.55}$$

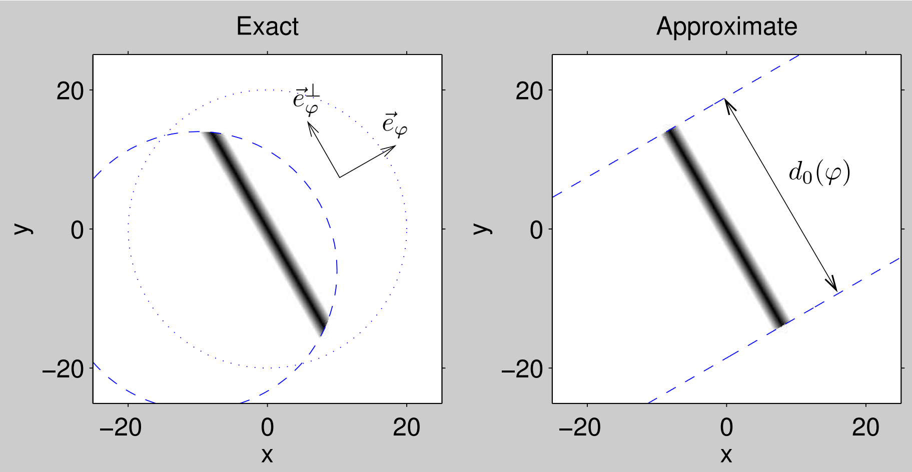

Figure 4.3: Approximation on “strip-like” function, $s_{\varphi,0}(\vec{x})$. A circular support function $\eta(\vec{x})$ is used here.

where we define the following “strip like” function:

$$s_{\varphi,0}(\vec{x}) \triangleq \breve{h}_0(\vec{x} \cdot \vec{e}_\varphi, \varphi)\eta_2(\vec{x}). \tag{4.56}$$

Local Frequency Response

Having found the local impulse response approximation (4.55), the next step is to find the local frequency response. This requires consideration of the edge effects.

The simplest approach to finding the local frequency response would be to take the 2D Fourier transform of the local impulse response in (4.48), while ignoring the “edge effects” caused by the support functions in (4.55). We found this approach to yield suboptimal accuracy. Taking the DSFT of (4.55) yields the following result:

$$H_{\mathrm{d0}}(\vec{\omega}) = \frac{1}{\Delta_\beta}\frac{1}{\Delta_{\mathrm{s}}}\int_0^{2\pi} w_0(\varphi) H_\varphi(\vec{\omega})\,\mathrm{d}\varphi, \tag{4.57}$$

where $H_\varphi(\vec{\omega})$ is the spectrum of $s_{\varphi,0}(\Delta\vec{n})$, as follows:

$$\begin{aligned} H_\varphi(\vec{\omega}) &= \sum_{\vec{n}} s_{\varphi,0}(\Delta\vec{n})\,\mathrm{e}^{-\imath(\vec{\omega}\cdot\vec{n})} \\ &\approx \frac{1}{\Delta^2}\iint s_{\varphi,0}(\vec{x})\,\mathrm{e}^{-\imath\frac{1}{\Delta}(\vec{\omega}\cdot\vec{x})}\,\mathrm{d}\vec{x} \\ &= \frac{1}{\Delta^2} S_{\varphi,0}\left(\frac{\vec{\omega}}{2\pi\Delta}\right), \end{aligned} \tag{4.58}$$

where $s_{\varphi,0}(\vec{x}) \overset{\text{2D FT}}{\longleftrightarrow} S_{\varphi,0}(u,v)$.

Because $s_{\varphi,0}(\vec{x})$ is in form of multiplication in space domain, this leads to convolution in frequency domain that is not desirable. Because of the "strip-like" nature, we make further approximation on $s_{\varphi,0}(\vec{x})$ that is projection-angle dependent and pixel dependent. The left plot in Figure 4.3 shows $s_{\varphi,0}(\vec{x})$ for fixed φ and $\vec{n}_0$ when a circular support function is used. $s_{\varphi,0}(\vec{x})$ has finite width along the ray direction $\vec{e}_\varphi^\perp$ and is very sharp along the direction perpendicular to the ray direction $\vec{e}_\varphi$. Therefore we make the following approximation:

$$s_{\varphi,0}(\vec{x}) \approx \check{h}_0(\vec{x}\cdot\vec{e}_\varphi, \varphi)\eta_0\left(\frac{\vec{x}\cdot\vec{e}_\varphi^\perp}{d_0(\varphi)}\right), \tag{4.59}$$

where $d_0(\varphi)$ denotes the length of the chord through $\vec{n}_0$ through the FOV at angle $(\varphi + \pi/2)$. This approximation is useful because the approximated $s_{\varphi,0}(\vec{x})$ is a separable function in rotated coordinates, $(\vec{e}_\varphi, \vec{e}_\varphi^\perp)$. To preserve the non-negative definiteness of the *Gram Matrix*, we chose $\eta_0(\vec{x})$ to be a triangular function with the angular-dependent width $d_0(\varphi)$:

$$\eta_0\left(\frac{\vec{x}\cdot\vec{e}_\varphi^\perp}{d_0(\varphi)}\right) = \text{tri}\left(\frac{\vec{x}\cdot\vec{e}_\varphi^\perp}{d_0(\varphi)}\right).$$

The 2D FT of $s_{\varphi,0}(\vec{x})$ is easiest to see for the case $\varphi = 0$:

$$\begin{aligned} s_{0,0}(x,y) &= \check{h}_0(x,0)\text{tri}\left(\frac{y}{d_0(0)}\right) \\ &\overset{\text{2D FT}}{\longleftrightarrow} S_{0,0}(u,v) = |A_0(u,0)|^2\, d_0(0)\, \text{sinc}^2(d_0(0)\, v), \end{aligned}$$

where $A_0(\nu,\varphi)$ is associated with the detector response and basis effect, given in (4.74). By the rotation property of the 2D FT:

$$S_{\varphi,0}(\rho,\Phi) \approx |A_0(\rho\cos(\Phi-\varphi),\varphi)|^2\, d_0(\varphi)\, \text{sinc}^2(d_0(\varphi)\rho\sin(\Phi-\varphi)).$$

Therefore, using (4.49) and (4.58), the local frequency response $H_0(\rho,\Phi)$ around a point $\vec{n}_0$ is

$$H_0(\rho,\Phi) \approx \frac{1}{\Delta_\beta\Delta_{\text{S}}\Delta^2}\int_0^{2\pi} w_0(\varphi)\, S_{\varphi,0}(\rho,\Phi)\, \mathrm{d}\varphi, \tag{4.60}$$

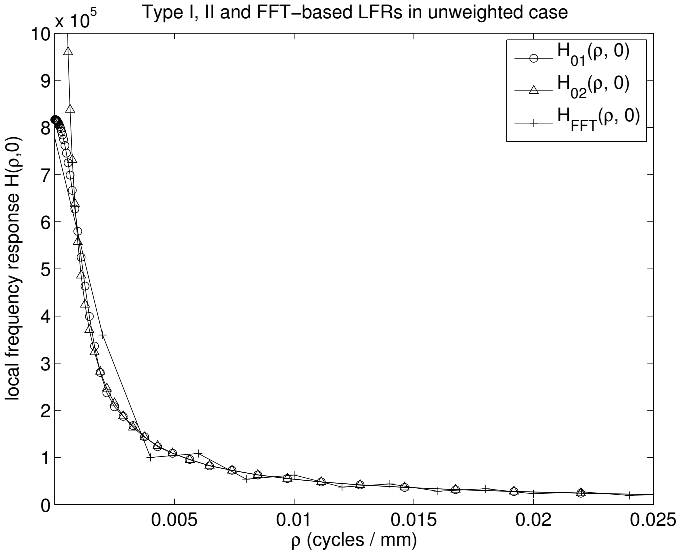

Figure 4.4: Type I, Type II and FFT-based local frequency responses $H_{01}(\rho, 0)$, $H_{02}(\rho, 0)$ and $H_{\text{FFT}}(\rho, 0)$ for $\vec{n}_0$ at image center in unweighted case: $w(s, \beta) = 1$. $H_{02}(0, 0)$ is not shown because it is infinite.

where the following function captures both detector response effects and edge effects:

$$S_{\varphi,0}(\rho, \Phi) = |A_0(\rho\cos(\Phi - \varphi), \varphi)|^2 \, d_0(\varphi) \operatorname{sinc}^2(d_0(\varphi)\rho\sin(\Phi - \varphi)), \tag{4.61}$$

$A_0(\nu, \varphi)$ is the 1D FT of $a_0(r, \varphi)$ with respect to r.

Further Approximations of Local Frequency Response

The local frequency response of the Gram operator in (4.60) is very accurate. However, direct implementation of (4.60) is still computationally demanding. We present here two types of further approximations to simplify (4.60).

1. **Type I non-separable form**

   As $d_0(\varphi) \to \infty$, one can show that for large $|\rho|$,

   $$d_0(\varphi) \operatorname{sinc}^2(d_0(\varphi)\rho\sin(\Phi - \varphi)) \to \delta(\rho\sin(\Phi - \varphi)) \, .$$

   Therefore the sinc^2 term is sharply peaked near $\Phi = \varphi$ and $\Phi = \varphi \pm \pi$, so we consider the further simplifying approximation

   $$\int_0^{2\pi} w_0(\varphi) \, S_{\varphi,0}(\rho, \Phi) \, \mathrm{d}\varphi \approx w_0(\Phi) \, |A_0(\rho, \Phi)|^2 \, G_0(\rho, \Phi), \tag{4.62}$$

where

$$G_0(\rho, \Phi) = \int_0^{2\pi} d_0(\varphi) \operatorname{sinc}^2(d_0(\varphi)\rho \sin(\Phi - \varphi)) \, \mathrm{d}\varphi \, . \tag{4.63}$$

Substituting into (4.60) leads to the "Type I" approximation:

$$H_0(\rho, \Phi) \approx H_{01}(\rho, \Phi) \triangleq \frac{w_0(\Phi)}{\Delta_\beta \Delta_{\mathrm{S}} \Delta^2} \left| A_0(\rho, \Phi) \right|^2 G_0(\rho, \Phi). \tag{4.64}$$

Although $H_{01}(\rho, \Phi)$ is not separable, we can precompute $w_0(\Phi)$ and tabulate $G_0(\rho, \Phi)$ once for all pixels for coarsely sampled Φ. Accurately computing $G_0(\rho, \Phi)$ is crucial, therefore finely sampled φ is necessary in (4.62).

2. **Type II separable form**

   We can simplify further by using the sifting property of the Dirac impulse:

$$\int_0^{2\pi} w_0(\varphi) \, S_{\varphi,0}(\rho, \Phi) \, \mathrm{d}\varphi \approx \frac{2}{|\rho|} \, w_0(\Phi) \left| A_0(\rho, \Phi) \right|^2 .$$

Because typically $A_0(\nu, \varphi)$ varies slowly, we also consider the following further approximation:

$$A_0(\nu, \varphi) \approx A_0(0, \varphi). \tag{4.65}$$

Combining all the above approximations yields the following separable approximation to the local frequency response:

$$H_0(\rho, \Phi) \approx H_{02}(\rho, \Phi) \triangleq \frac{2 \left| A_0(0, \varphi) \right|^2}{\Delta_\beta \Delta_{\mathrm{S}} \Delta^2} \frac{w_0(\Phi)}{|\rho|}. \tag{4.66}$$

This "Type II" separable form agrees with the familiar FT of $\frac{1}{r}$. Figure 4.4 shows the profiles of analytical Type I, Type II and FFT-based local frequency responses for $\vec{n}_0$ at image center in unweighted case. We can see that three profiles agrees with each other closely. The discrepancy is mainly at low frequencies.

4.5.2 Analysis for 2D Quadratic Regularization

To evaluate the variance using (4.19) and (4.20), we also need the local frequency response of quadratic regularization, $R_0(\rho, \Phi)$, [33, 35, 89, 94].

Practical regularization methods are based on the differences between neighboring pixel values. For a discrete-space 2D object $\mu[\vec{n}]$, a typical quadratic roughness penalty is given in (4.4) and (4.5) for 1st-order differences. The $r_l[\vec{n}]$ values are possibly space variant. For the purpose of local frequency response analysis, we examine the characteristics of $R(\boldsymbol{\mu})$ near a pixel $\vec{n}_0$ of interest, so we define $r_{l,0} \triangleq r_l[\vec{n}_0]$ assuming $r_l[\vec{n}]$ values vary smoothly. Then, the quadratic roughness penalty near a pixel $\vec{n}_0$ has the following form:

$$R(\boldsymbol{\mu}) = \sum_{\vec{n}} \sum_{l=1}^{L} r_{l,0} \frac{1}{2} \Big((c_l ** \mu)[\vec{n}] \Big)^2 .$$

The $r_{l,0}$ values are design parameters that affect the directionality of the regularization and hence the shape of the PSF. Each $c_l[\vec{n}]$ is a (typically) high-pass filter. For a first-order difference:

$$c_l[\vec{n}] = \xi_l \left(\delta_2[\vec{n}] - \delta_2[\vec{n} - \vec{m}_l] \right),$$

or for a 2nd-order difference:

$$c_l[\vec{n}] = \xi_l(\delta_2[\vec{n}] - \delta_2[\vec{n} - \vec{m}_l]) ** \xi_l(\delta_2[\vec{n}] - \delta_2[\vec{n} - \vec{m}_l]),$$

where $\xi_l = \|\vec{m}_l\|^{-\upsilon/2}$, $\vec{m}_l = (n_l, m_l)$ denotes the spatial offsets to the neighboring pixels, and υ is the power of weights for diagonal neighbors that can be chosen by the user. For example, common practice chooses $\upsilon = 1$ [30, 70].

Applying Parseval's theorem, we can rewrite $R(\boldsymbol{\mu})$ as follows:

$$R(\boldsymbol{\mu}) = \sum_{l=1}^{L} \int_{-\pi}^{\pi} \int_{-\pi}^{\pi} \frac{1}{2} r_{l,0} \left| C_l(\vec{\omega}) U(\vec{\omega}) \right|^2 \frac{d\vec{\omega}}{(2\pi)^2}, \tag{4.67}$$

where $\mu[\vec{n}] \overset{\text{FT}}{\longleftrightarrow} U(\vec{\omega})$ and the DSFT of a Λ-order (where $\Lambda \in \mathbb{N}$) difference has the following magnitude:

$$\begin{aligned} |C_l(\vec{\omega})| &= \xi_l^{\Lambda} \left|1 - \mathrm{e}^{-\imath(\vec{\omega}\cdot\vec{m}_l)}\right|^{\Lambda} \\ &= \xi_l^{\Lambda} 2^{\Lambda} \left|\sin^{\Lambda}\left(\frac{1}{2}(\vec{\omega}\cdot\vec{m}_l)\right)\right|. \end{aligned}$$

In the polar coordinates of (4.20):

$$|C_l(\rho, \Phi)|^2 = |C_l(2\pi\rho\Delta\vec{e}_{\Phi})|^2 = \xi_l^{2\Lambda} 4^{\Lambda} \sin^{2\Lambda}(\pi\Delta\rho\vec{e}_{\Phi}\cdot\vec{m}_l)\,. \tag{4.68}$$

Thus, the *Type I* local frequency response for the regularization operator is

$$\begin{aligned} R_0(\rho, \Phi) &= R_{01}(\rho, \Phi) = \sum_{l=1}^{L} r_{l,0} \, |C_l(\rho, \Phi)|^2 \\ &= \sum_{l=1}^{L} r_{l,0} \xi_l^{2\Lambda} 4^{\Lambda} \sin^{2\Lambda}(\pi\Delta\rho\vec{e}_{\Phi}\cdot\vec{m}_l)\,. \end{aligned} \tag{4.69}$$

Applying the approximation $\sin(x) \approx x$ to (4.68) yields:

$$\begin{aligned} |C_l(\rho, \Phi)|^2 &\approx \xi_l^{2\Lambda}(\vec{m}_l\cdot\vec{e}_{\Phi})^{2\Lambda}(2\pi\Delta\rho)^{2\Lambda} \\ &= (2\pi\rho\Delta)^{2\Lambda}\xi_l^{(1-2/\upsilon)2\Lambda}\cos^{2\Lambda}(\Phi - \varphi_l), \end{aligned}$$

where the angle between the lth neighbors is

$$\varphi_l \triangleq \tan^{-1}\frac{m_l}{n_l}.$$

With this simplification, the *Type II* local frequency response of the regularizer is approximately separable in (ρ, Φ):

$$R_0(\rho, \Phi) \approx R_{02}(\rho, \Phi) = (2\pi\rho\Delta)^{2\Lambda}\tilde{R}_0(\Phi), \tag{4.70}$$

where

$$\tilde{R}_0(\Phi) \triangleq \sum_{l=1}^{L} \xi_l^{(1-2/\upsilon)2\Lambda} r_{l,0} \cos^{2\Lambda}(\Phi - \varphi_l)\,.$$

This separable form agrees with the familiar FT of the differentiation operation.

4.5.3 Variance Prediction Implementation

Having obtained the approximations to $H_0(\rho, \Phi)$, the local frequency response of the Gram operator given in (4.64) and (4.66), and to $R_0(\rho, \Phi)$, the local frequency response of the regularizer given in (4.69) and (4.70), we can discretize the integral (4.19) again to compute the variance image. There are two variance prediction expressions for fan-beam transmission tomography based on the Type I $H_{01}(\rho, \Phi)$ given in (4.64) and $R_{01}(\rho, \Phi)$ given in (4.69), and the Type II $H_{02}(\rho, \Phi)$ given in (4.66) and $R_{02}(\rho, \Phi)$ given in (4.70).

Double Integral Approach

The variance prediction using $H_{01}(\rho, \Phi)$ in (4.64) and $R_{01}(\rho, \Phi)$ in (4.69) involves a double integral and can be implemented by a double summation. We call this prediction the double integral (DI) approach. The location-dependent weighting function $w_0(\Phi)$ can be precomputed, with the computation equivalent to one back-projection. We can coarsely sample Φ because $P_0(\rho, \Phi)$ is fairly smooth along Φ.

Single Integral Approach

The separability properties of $H_{02}(\rho, \Phi)$ in (4.66) and $R_{02}(\rho, \Phi)$ in (4.70) enable us to carry out the inner integral over ρ analytically. Therefore the double-integral in (4.19) is reduced to one single integral over Φ. Substituting (4.66) and (4.70) into (4.19) yields the remarkably simple expression:

$$\mathsf{Var}\{\hat{\mu}[\vec{n}_0]\} \approx \int_0^{2\pi} \frac{\zeta(\Phi)/3}{2\,|A_0(0,\Phi)|^2\, w_0(\Phi) + \alpha 4\pi^2 \zeta(\Phi) \tilde{R}_0(\Phi)} \, \mathrm{d}\Phi, \tag{4.71}$$

where $\zeta(\Phi) \triangleq \rho_{\mathrm{max}}^3(\Phi) \Delta_\beta \Delta_{\mathrm{S}} \Delta^4$. We call this prediction the single integral (SI) approach. We evaluate this integral using a finite summation, with $w_0(\Phi)$ and $\tilde{R}_0(\Phi)$ precomputed. Therefore, computing (4.71) is equivalent to one back-projection.

Implementation of The Single Integral Prediction

We found empirically that the SI approach (4.71) gave predictions that could be improved by including a single global scale factor, presumably because the SI approach (4.71) uses many approximations to achieve its simple form. In particular, we found that the SI method underestimates the variance, presumably because the "Fisher information" implied by Type II local frequency response in (4.66) is too large for low spatial frequencies. To determine the scale factor, we assumed that the DFT-based approach and the analytical approach should produce equivalent results at the image center. Specifically, we used the predicted variance for unweighted least squares estimator with standard quadratic penalty (QPULS) for unit variance data.

For QPULS estimator for unit variance data, the statistical weighting, $w(s, \beta)$ becomes 1. Consider the standard quadratic penalty with first-order ($\Lambda = 1$) differences and second-order neighborhood (L = 4), for which $\varphi_{1,2,3,4} = 0, \pi/2, \pi/4$, and $-\pi/4$ and $r_{l,0} = (1, 1, 1, 1)$. We used $\upsilon = 1$ both in calibration and reconstruction as is the common practice in quadratic regularization. For these choices, the Type II $R_{02}(\rho, \Phi)$ in (4.70) becomes independent of Φ:

$$\tilde{R}_0(\Phi) = \sum_{l=1}^{L} \|\vec{m}_l\| = 1 + \sqrt{2}. \tag{4.72}$$

Finally, to determine the scale factor, we computed the ratio of the variance predicted by the DFT approach over that predicted by (4.71). For the parameters used in our simulations, this factor was $(1.13)^2$. This value would need to recomputed for different system geometries or regularization parameters, but is otherwise patient independent.

4.5.4 Simulation Results

To evaluate the performance of the proposed methods, we implemented the variance predictions for fan-beam tomographic images reconstructed by quadratically penalized likelihood algorithm. We simulated 1000 realizations of fan-beam transmission scans using a 256×256 NCAT phantom and a blank scan of 10^6 counts/detector. The corresponding sinogram size was 444 samples in s, spaced by $\Delta_{\mathrm{S}} \approx 2$ mm and 492 source positions over 360°. We simulated the geometry of the GE LightSpeed Pro CT scanner with the source-to-detector distance around 949 mm, the isocenter-to-detector distance 408 mm and $\Delta = 500/256$ mm.

An elliptical support was used for $\mathcal{S}$, with $p = |\mathcal{S}| = 43892$. For simplicity, in (4.63) we used the width of the central profile through the FOV:

$$d_0(\varphi) \approx d(\varphi) \triangleq \frac{2 z_1 z_2}{\sqrt{z_1^2 \sin^2\!\varphi + z_2^2 \cos^2\!\varphi}}, \tag{4.73}$$

where $z_1 = 244.1$ mm and $z_2 = 220.7$ mm are the semi-major and semi-minor axes of the ellipse. This approximation is exact when $\vec{n}_0$ is at the ellipse center. The approximation to $d(\varphi)$ becomes less accurate as $\vec{x}_c[\vec{n}_0]$ approaches the edge of the ellipse support.

For simplicity, we use $\rho_{\max}(\Phi) \approx \frac{1}{2\Delta}$ and model the detector response[3] in (4.36) by a shift-invariant rectangle of width Δ_{S}:

$$b(s) = \frac{1}{\Delta_{\mathrm{S}}} \operatorname{rect}\left(\frac{s}{\Delta_{\mathrm{S}}}\right).$$

In the case of a square pixel basis $\chi(\vec{x}) = \operatorname{rect}_2(\vec{x})$[4], we have from (4.46)

$$A_0(\nu, \varphi) = \operatorname{sinc}\left(\frac{\Delta_{\mathrm{S}} \nu}{m_0(\varphi)}\right) \Delta^2 \operatorname{sinc}(\nu \Delta \cos\varphi) \operatorname{sinc}(\nu \Delta \sin\varphi), \tag{4.74}$$

which we substitute into (4.61). In our simulation, we make the following simplification:

$$m_0(\varphi) \approx m_c(\varphi) = m_c = D_{\mathrm{sd}} / D_{\mathrm{s0}},$$

where m_c is the value of $m_0(\varphi)$ at the image center.

---

[3] A more accurate model could include detector deadspace and crosstalk effects.

[4] $\operatorname{rect}_2(\vec{x}) \triangleq \operatorname{rect}(x)\operatorname{rect}(y)$ is a 2D square function.

We chose the regularization parameter $\alpha = 2^{11}$ to give FWHM = 1.72 pixels, *i.e.*, 3.4 mm, at the center of the image. For each realization, $\hat{\boldsymbol{\mu}}$ was reconstructed using 70 iterations of the convergent incremental optimization transfer algorithm (PL-IOT) [4] with 41 subsets and no nonnegativity constraint. The initial images were the filtered back-projection (FBP) images with equivalent spatial resolution, obtained by post-filtering ramp-filtered FBP images with the designed PSF. We computed the sample standard deviation pixel by pixel within the finite support $\mathcal{S}$ used in reconstruction. All images and profiles are shown in Hounsfield unit (HU).

Two prediction approaches are investigated here: the DI approximation (4.19) with Type I $H_{01}(\rho, \Phi)$ in (4.64) and $R_{01}(\rho, \Phi)$ in (4.69), and the SI approximation (4.71) with $\tilde{R}_0(\Phi)$ in (4.70). The former formula was derived with fewer approximations while the latter formula involves more approximations. The accuracy and computation time are compared below.

We considered three types of regularization: standard, certainty-based [40]. and modified [84]. In all cases, we implemented (4.69) and (4.70) for regularization with first-order ($\Lambda = 1$) differences and second-order neighborhood ($L = 4$). The standard and certainty-based cases used all 1000 realizations of fan-beam transmission scans while only 250 realizations are used in modified case.

In all cases, the standard deviation images predicted by the DI approach are displayed while both DI and SI predictions are compared in the profile plots.

Standard Quadratic Penalty Function

We first considered a standard quadratic penalty where

$$r_{l,0} = \kappa_c^2,$$

and κ_c^2 is the value of $\kappa^2[\vec{n}_0]$ at the image center in (4.75) below. This choice assures that the resolution of the two studies is matched at the image center. In this case, $\tilde{R}_0(\Phi) = (1+\sqrt{2})\kappa_c^2$ is a constant for all pixels.

Figure 4.5 shows the reconstructed images and empirical standard deviation images. The empirical standard deviation image for FBP is also shown. The average of FBP standard deviations is around 2.2 HU, approximately 1.8 times higher than that of PL-IOT, 1.2 HU, illustrating the noise advantage of the statistical reconstruction methods at matched resolution.

Figure 4.5 also shows the central horizontal and vertical profiles of the standard deviation maps. The analytical, the FFT-based and the empirical standard deviations agree with one another very closely within the object. The largest discrepancy within the object was about 10% in the left lung for unknown reasons.

Certainty-Based Quadratic Penalty Function

We next investigate a more complicated regularizer that was designed to achieve nearly uniform spatial resolution [40]. In this case, we used space-varying regularizer:

$$r_{l,0} = \kappa^2[\vec{n}_0],$$

where

$$\kappa^2[\vec{n}_0] \triangleq \frac{1}{2\pi}\int_0^{2\pi} w(\tilde{s}(r_0(\varphi)), \tilde{\beta}(r_0(\varphi),\varphi))\,\mathrm{d}\varphi\,. \tag{4.75}$$

Here, $\tilde{R}_0(\Phi)$ is still independent of Φ, but varies spatially. Computing the "certainty map" (4.75) requires a simple backprojection with fan-to-parallel beam rebinning.

Figure 4.6 shows the reconstructed images, standard deviation images and central horizontal and vertical profiles. In this case, the average of FBP standard deviations is around 2.2 HU, approximately 1.8 times higher than that of PL-IOT, 0.7 HU. The analytical, the FFT-based and the empirical standard deviations agree with one another very closely within the object.

Modified Quadratic Penalty Function

Consider a modified quadratic penalty in [84], where

$$\tilde{R}_0(\Phi) \triangleq \sum_{l=1}^{L} r_{l,0} \cos^2(\Phi - \varphi_l)\,.$$

For first-order differences and 2nd-order neighborhood (L = 4), $\varphi_{1,2,3,4} = 0, \pi/2, \pi/4$, and $-\pi/4$. Ideally, $r_{l,0}$ is designed in a way that leads to nearly uniform and isotropic spatial resolution s.t.

$$\tilde{R}_0(\Phi) \approx w_0(\Phi). \tag{4.76}$$

Figure 4.7 shows the reconstructed images, standard deviation images and central horizontal and vertical profiles. In this case, the average of FBP standard deviations is around 1.8 HU, approximately 3 times higher than that of PL-IOT, 0.6 HU. The analytical, the FFT-based and the empirical standard deviations agree with one another very closely within the object. However, both empirical and predicted standard deviation images show four bright strips coming out from the object. Analytical method overestimates the variances at these areas. The angles of the strips seem to follow the φ_l's in the second order neighborhood. Analytical prediction method also overestimates the variance at the area around the nodule in the left lung. These are probably due to the rapid change of the statistical weights $w(s, \beta)$ and the user-designed parameters $r_{l,0}$. These facts indicate that further investigation might be needed to find the optimal solution in regularization design problem. We only use 250 realizations of transmission scans to compute empirical predctions in fully-modified quadratic penalty case. Therefore empirical predictions appear more noisy than the ones in standard and certainty-based cases.

In all cases, the analytical and the FFT-based predictions are somewhat less accurate near the edge of the finite support used in image reconstruction. This is probably due to the fact that the "local stationarity" approximation is less accurate in this area where the statistical weights $w(s, \beta)$ can vary rapidly. The approximation (4.73) may also vary rapidly in our study, so it may be possible to improve accuracy near the edges of the FOV by using $d_0(\varphi)$.

Error Distribution

We are interested in the distribution of the reconstruction errors, $\hat{\mu}[\vec{n}] - \mu[\vec{n}]$, from 1000 realizations for three different pixels: a pixel at image center, a pixel outside of object and inside the finite support, and a pixel in a lower-right rib. Figure 4.8 shows the histograms of the reconstruction errors for standard and certainty-based quadratic penalty functions. All the histograms display an approximately Gaussian shape. Table 4.1 shows the results of Lilliefors goodness-of-fit test of composite normality on the reconstruction errors by using Matlab `lillietest` command. These quantitative results confirm that the reconstruction errors follow an approximately Gaussian.

p-value	standard quadratic penalty			certainty-based quadratic penalty		
pixel locations	center	top	lower-right	center	top	lower-right
p-value	0.2093	> 0.5	0.3984	> 0.5	> 0.5	0.3554

Table 4.1: p-values of Lilliefors goodness-of-fit test of composite normality on the reconstruction errors for standard and certainty-based quadratic functions, respectively.

Computation Time and Accuracy

In our calculations, we used 123 samples in Φ and 128 samples in ρ in (4.19) to predict a 256×256 standard deviation image. Both DI and SI predictions precompute $w_0(\Phi)$ and $G_0(\rho, \Phi)$. The precomputation time for $w_0(\Phi)$ was about 19 seconds on dual Intel Xeon 3.40GHz CPU. Table 4.2 summarizes the computation time comparison for empirical, FFT-based and analytical (double-integral and single-integral) prediction methods. The precomputation time for $G_0(\rho, \Phi)$ with 492 samples in φ was 2.3 seconds. The DI prediction requires no scale factor precomputation and the computation time was about 135 seconds. The SI prediction requires the scale factor precomputation that is $(1.13)^2$ in our case, and the computation time for prediction was about 0.6 second. In contrast, the FFT-based prediction needed about 374 seconds to compute only one single central profile. Because the FFT-based predictions are only computed for two central profiles, we calculted its computation time for the whole standard deviation map by multipling the prediction time for a single pixel and $p = 43892$. We see that our proposed methods are much faster than both empirical and FFT-based methods. As expected, the DI prediction is slightly more accurate than the SI prediction, particularly near edges. The SI prediction matches a bit better with the FFT-based prediction because the scale factor calibration was based on FFT-predicted values. For the purposes of regularization design or noise exploration, we believe that the very fast SI approach is adequate.

Table 4.3 compares the normalized root-mean square (NRMS) percent errors of analytical and FFT-based predictions with respect to empirical results. Because we only compute two central profiles of the FFT-based prediction in each case, we compute the normalized root-mean square (NRMS) percent errors only for these two central profiles. For κ_c^2 case, the NRMS percent errors for FFT, DI and SI are 6.6%, 6.8% and 6.6%; for κ_0^2 case, the NRMS percent errors for FFT, DI and SI are 6.5%, 6.0% and 8.3%; for modified penalty case, the NRMS percent errors for FFT, DI and SI are 10%, 14.6% and 10.7% within the object, respectively. Our analytical methods can provide comparable accuracies as the FFT-based method.

Types of predictions	precomputation			total time
	$w_0(\Phi)$	$G_{\text{center}}(\rho, \Phi)$	calibration	
empirical	N/A	N/A	N/A	several days
FFT-based	N/A	N/A	N/A	64123 s
analytical (Double-integral)	19 s	2.3 s	N/A	156.3 s
analytical (Single-integral)	19 s	N/A	2.1 s	21.1 s

Table 4.2: Computation time comparison. The FFT-based predictions are computed only for two central profiles. We calculted its computation time for the whole standard deviation map by multipling the prediction time for a single pixel and $p = 43892$.

Types of penalties	FFT-based	Analytical	
		Double-integral	Single-integral
standard	6.6%	6.8%	6.6%
certainty-based	6.5%	6.0%	8.3%
modified	10%	14.6%	10.7%

Table 4.3: The normalized root-mean square (NRMS) percent errors of analytical and FFT-based predictions with respect to empirical predictions for the two central profiles. The standard error of empirical predictions in standard and certainty-based quadratic penalty cases (with 1000 realizations) is about $1/\sqrt{2(1000-1)} \approx 2.2\%$. The standard error of empirical predictions in modified quadratic penalty cases (with 250 realizations) is about $1/\sqrt{2(250-1)} \approx 4.5\%$.

4.5.5 Conclusion and Discussion

This chapter has developed analytical variance approximations for 2D tomography. The double integral (4.19) with (4.64) and (4.69), and the single integral (4.71) provide fast and accurate variance predictions for a quadratically penalized likelihood estimator in fan-beam tomography. The simplest of the proposed approaches (4.71) requires one backprojection with some additional summations, which is much less computation than previous FFT-based methods. In fact, using the proposed methods, we can predict the variance map in much less time than it takes to reconstruct a single image. The proposed approximations are especially useful in the case that the variance information is needed for many or all pixels, such as when choosing space-varying regularization parameters [84]. The empirical results from the simulated fan-beam CT transmission scans demonstrate that the proposed variance approximations are very accurate. Future work will explore using these predictions for regularization design. As indicated in modified quadractic penalty case, variance predictions can provide guidance in finding the optimal solution in regularization design.

Although we focused on variance prediction, by using (4.16) we could also easily predict covariances and thus predict the covariance of an region of interest (ROI) whose size is small enough that the local approximations are sufficiently accurate. However, if only a single local autocorrelation function is needed, then the FFT approach is probably easier to use. For analysis of detectability of lesions with unknown locations, autocorrelations at many spatial positions may be needed [53–55, 76, 103], in which case the proposed approach based on (4.16) can save computation. The matrix method described in (4.7) and (4.8) is also applicable to other imaging modalities, such as PET and SPECT [32]. Therefore the proposed methods are also readily extended to those imaging modalities, with different considerations of the weighting function.

The proposed analytical variance approximations are only investigated in the case of the shift-invariant detector blur. We can also generalize the analysis to shift-variant detector blur where the local shift-invariance approximation is applicable, *e.g.*, for varifocal collimators in SPECT. In this case, $b(s - s')$ is replaced by $b(s, s')$ in (4.37) and $b_0(r, \varphi)$ in (4.47) becomes

$$b_0(r, \varphi) \triangleq m_0(\varphi)\, b(s_0(\varphi) + m_0(\varphi)\, r, s_0(\varphi)),$$

where

$$s_0(\varphi) \triangleq D_{\mathrm{sd}} \arcsin \frac{r_0(\varphi)}{D_{\mathrm{s0}}}.$$

The work in this chapter has focused on 2D fan-beam geometry. 3D generalization of these methods can be done by applying the same principles [108]. This chapter has also focused on analytical variance approximations for the case of quadratic regularization. An interesting challenge for future work is to generalize the analysis to the case of edge-preserving non-quadratic regularization. The analysis in [5, 6] may be a useful starting point.

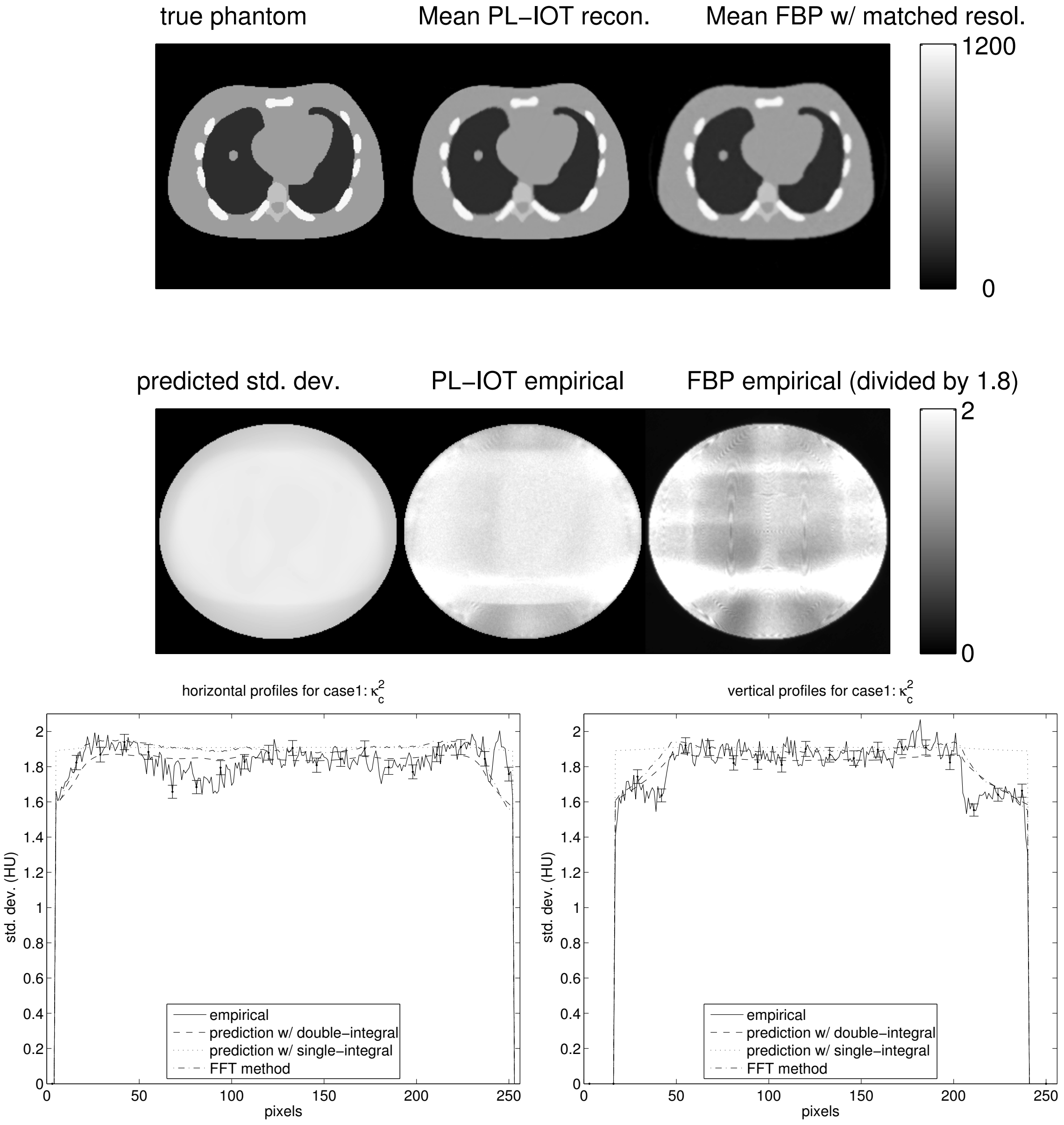

Figure 4.5: Predicted and empirical standard deviation images (in HU) and central profiles for NCAT phantom for PL fan-beam transmission image reconstruction using the standard quadratic penalty: $\tilde{R}_0 = (1 + \sqrt{2})\kappa_c^2$.

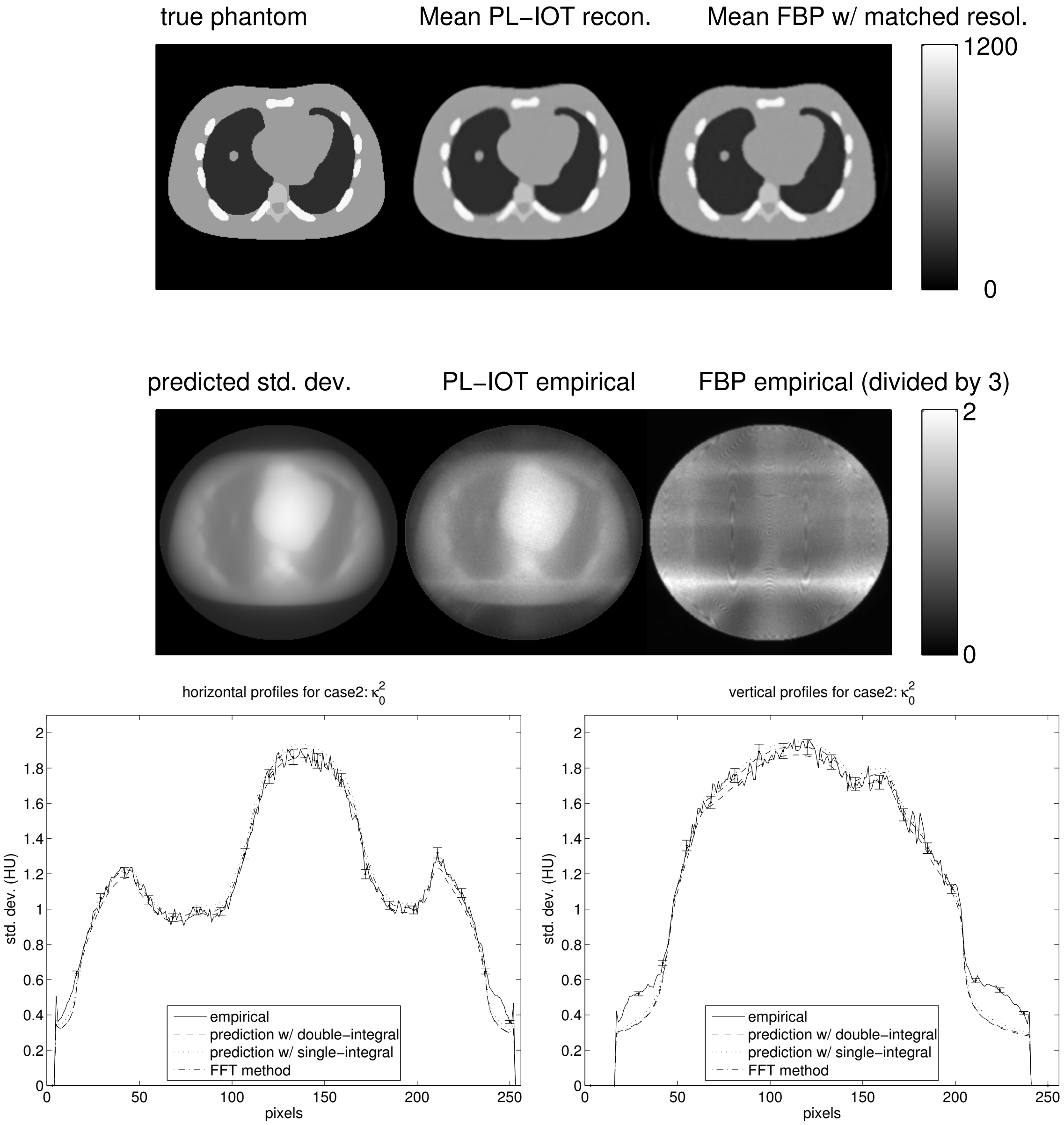

Figure 4.6: Predicted and empirical standard deviation images (in HU) and central profiles for NCAT phantom for PL fan-beam transmission image reconstruction using the certainty-based quadratic penalty.

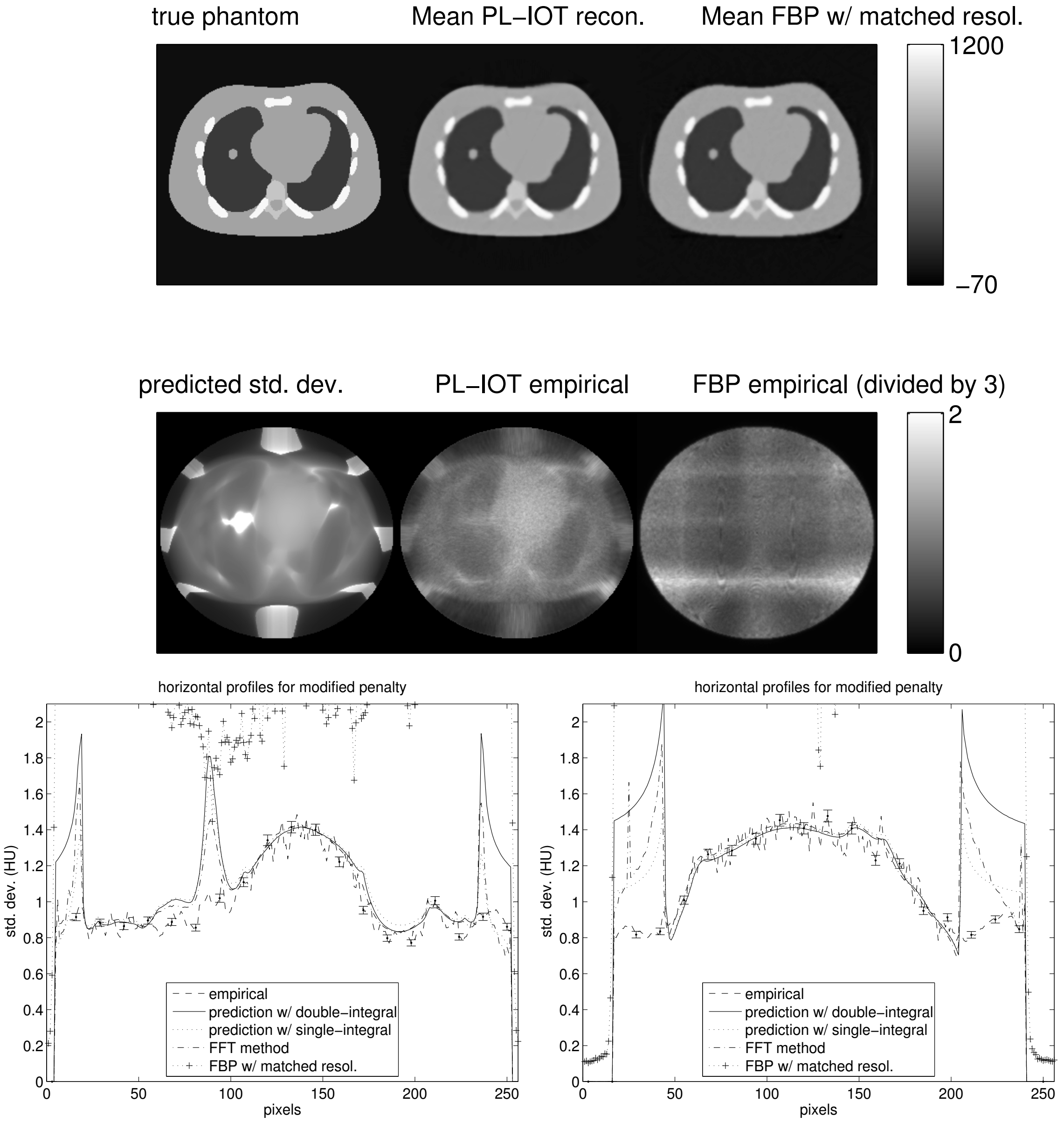

Figure 4.7: Predicted and empirical standard deviation images (in HU) and central profiles for NCAT phantom for PL fan-beam transmission image reconstruction using the modified quadratic penalty. Only 250 realizations are used in this case.

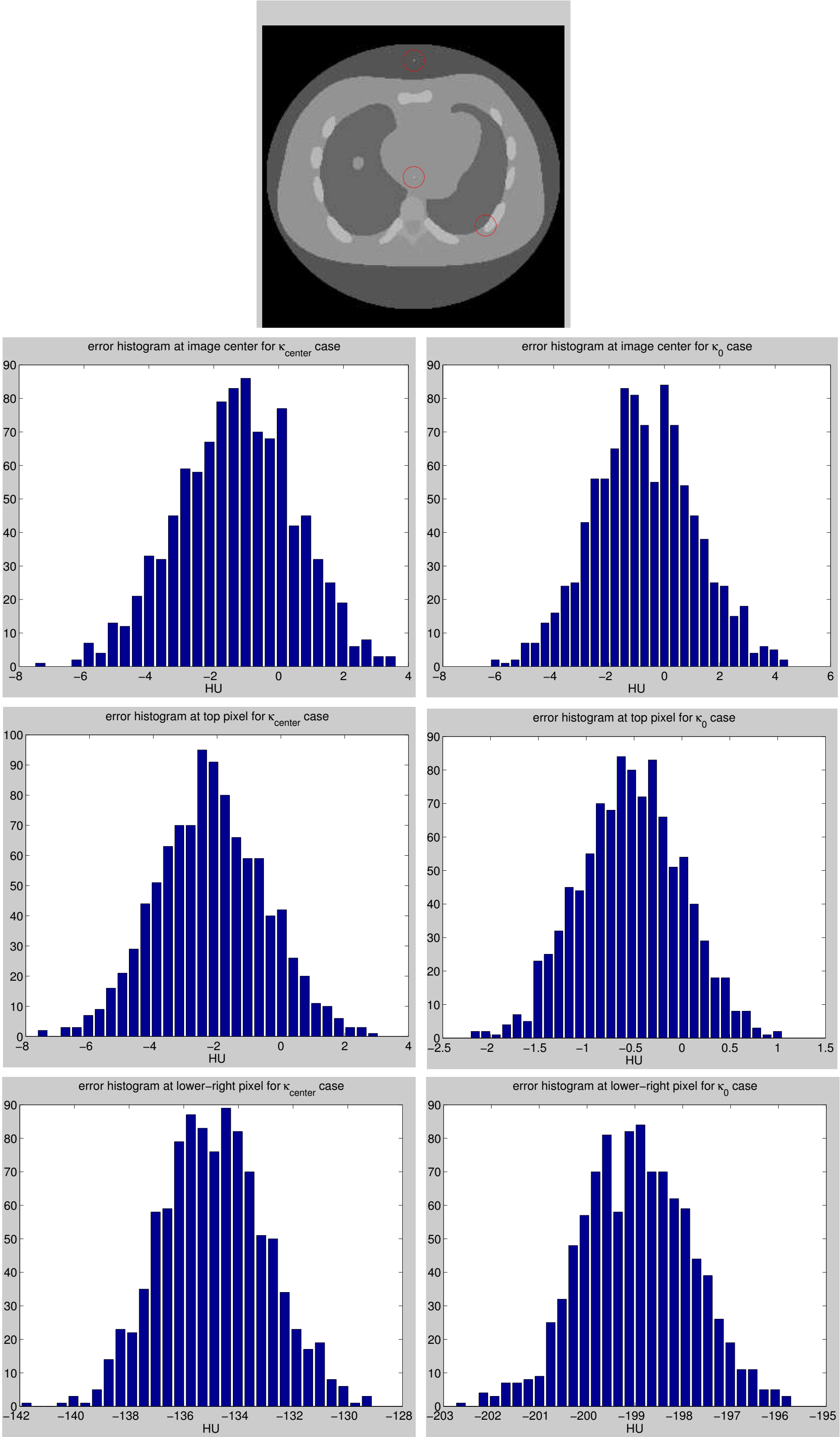

Figure 4.8: Histogram of $(\hat{\mu}[\vec{n}] - \mu[\vec{n}])$ for three pixel locations: a pixel at image center, a pixel outside of object and inside the finite support, and a pixel in a lower-right rib. Three figures on the left are for standard quadratic penalty case, and three figures on the right are for certainty-based quadratic penalty case.

CHAPTER 5

3D Variance Estimation for Quadratically Penalized-Likelihood Image Reconstruction

The analytical variance approximations for 2D tomography presented in the previous chapter have shown good accuracy while requiring much less computation than previous matrix-based and DFT-based methods. The advantages of these approaches should become more pronounced for larger set of data, such as axial and helical cone-beam geometries. This chapter generalizes the analytical 2D variance prediction methods into a 3D cylindrical cone-beam geometry.

The main challenge of 3D extension to the cone-beam variance approximations is the mismatch between the number of variables. There is no one-to-one explicit cone-to-parallel relationship in projection space. A two-dimensional area detector is used in 3D cone-beam tomography that is specified by coordinates (s, t). Both axial and helical cone-beam projection spaces are characterized by only three independent indices (s, t, β). The axial cone-beam geometry is a special case of helical cone-beam geometry with zero helical pitch. In 3D parallel-beam geometry projection space, there are four independent indices (u, v, φ, θ) for 3D X-ray transform. The ray direction is specified by (φ, θ) and the detector is specified by (u, v).

As an initial investigation of 3D CT, we circumvent this difficulty by assuming an idealized cylindrical cone-beam geometry by introducing an extra independent coordinate:

the elevation of the X-ray source, ζ. In this geometry, ideally the X-ray source can be at any location on an infinitely long cylinder along the z-axis. However, we develop approximations for the more realistic case where there is a finite set of ζ values, roughly corresponding to overlapping "step-and-shoot" axial scans.

5.1 3D X-Ray Transform

For 3D tomography with parallel rays, there are two projection angles: the *azimuthal angle* φ, and a *polar angle* θ. We use a coordinate system in which $\varphi \in [-\pi, \pi]$, and $\theta \in \mathcal{T} \subset [-\pi/2, \pi/2]$. Define $\vec{\gamma} = (\varphi, \theta)$ and define the following orthogonal unit vectors

(5.1)

$$\vec{e}_1(\vec{\gamma}) = \begin{bmatrix} \cos\varphi \\ \sin\varphi \\ 0 \end{bmatrix}, \qquad \vec{e}_2(\vec{\gamma}) = \begin{bmatrix} -\sin\varphi\sin\theta \\ \cos\varphi\sin\theta \\ \cos\theta \end{bmatrix}, \qquad \vec{e}_3(\vec{\gamma}) = \begin{bmatrix} \sin\varphi\cos\theta \\ -\cos\varphi\cos\theta \\ \sin\theta \end{bmatrix},$$

and the following point in $\mathbb{R}^3$:

(5.2)

$$\vec{p} = \vec{p}(u, v; \vec{\gamma}) = u\,\vec{e}_1 + v\,\vec{e}_2 = (u\cos\varphi - v\sin\varphi\sin\theta,\ u\sin\varphi + v\cos\varphi\sin\theta,\ v\cos\theta).$$

Letting (u, v) denote the coordinates on any 2D projection plane, we define the (X-ray) projection of a 3D object $f(\vec{\mathrm{x}})$ to be

$$p(u, v; \vec{\gamma}) = \int_{-\infty}^{\infty} f(\vec{p}(u, v; \vec{\gamma}) + \ell\,\vec{e}_3(\vec{\gamma}))\,\mathrm{d}\ell, \tag{5.3}$$

i.e., the line integrals along the lines $\{\vec{p} + \ell\,\vec{e} : \ell \in \mathbb{R}\}$, where $u, v \in \mathbb{R}$. Another way of writing this operation is

$$p(u, v; \vec{\gamma}) = \int f\left(\mathbf{T}_{\vec{\gamma}} \left[\begin{smallmatrix} u \\ \ell \\ v \end{smallmatrix} \right]\right) \mathrm{d}\ell, \tag{5.4}$$

where $\mathbf{T}_{\vec{\gamma}} = [\vec{e}_1(\vec{\gamma})\ \vec{e}_3(\vec{\gamma})\ \vec{e}_2(\vec{\gamma})]$ is a unitary matrix. So we have the following relation:

$$\mathbf{T}^{-1} = \mathbf{T}' = \begin{bmatrix} \cos\varphi & \sin\varphi & 0 \\ \sin\varphi\cos\theta & -\cos\varphi\cos\theta & \sin\theta \\ -\sin\varphi\sin\theta & \cos\varphi\sin\theta & \cos\theta \end{bmatrix}.$$

The matrix $\mathbf{T}$ is the product of two 3D rotation matrices [52, p. 100]:

(5.5)

$$\mathbf{T} = \boldsymbol{R}_{12}(\varphi)\boldsymbol{R}_{23}(\theta), \quad \boldsymbol{R}_{12}(\varphi) = \begin{bmatrix} \cos\varphi & \sin\varphi & 0 \\ \sin\varphi & -\cos\varphi & 0 \\ 0 & 0 & 1 \end{bmatrix}, \quad \boldsymbol{R}_{23}(\theta) = \begin{bmatrix} 1 & 0 & 0 \\ 0 & \cos\theta & -\sin\theta \\ 0 & \sin\theta & \cos\theta \end{bmatrix}.$$

A third way to write (5.3) or (5.4) is

$$p(u, v; \vec{\gamma}) = \iiint f(\vec{\mathrm{x}})\, \delta(\vec{x} \cdot \vec{e}_1(\vec{\gamma}) - u)\, \delta(\vec{x} \cdot \vec{e}_2(\vec{\gamma}) - v)\, \mathrm{d}\vec{x}\,. \tag{5.6}$$

5.1.1 Properties of 3D X-Ray Transform

3D X-ray transform satisfies many useful properties, among which shift and scaling properties are essential to us for deriving the variance approximations in 3D cylindrical cone-beam tomography.

Symmetry Property

Let $f(\vec{\mathrm{x}}) \overset{\text{3D Xray}}{\longleftrightarrow} p(u, v; \varphi, \theta)$. The 3D projection operation satisfies the following symmetry property:

$$p(-u, v; \varphi \pm \pi, \theta) = p(u, v; \varphi, \theta),$$

because $\vec{e}_1(\varphi \pm \pi, \theta) = -\,\vec{e}_1(\vec{\gamma})$ and $\vec{e}_2(\varphi \pm \pi, \theta) = -\,\vec{e}_2(\vec{\gamma})$.

Shift Property

The 3D projection operation also satisfies the following shift property:

$$f(\vec{\mathrm{x}}) \overset{\text{3D Xray}}{\longleftrightarrow} p(u, v; \varphi, \theta) \implies$$

$$f(\vec{\mathrm{x}} - \vec{z}) \overset{\text{3D Xray}}{\longleftrightarrow} p(u - \vec{z} \cdot \vec{e}_1(\vec{\gamma}), v - \vec{z} \cdot \vec{e}_2(\vec{\gamma}); \vec{\gamma}). \tag{5.7}$$

Scaling Property

Let $f(\vec{\mathrm{x}}) \overset{\text{3D Xray}}{\longleftrightarrow} p(u, v; \varphi, \theta)$. We would like to find the 3D projection $q(u, v; \varphi, \theta)$ of $f(x/a, y/a, z/b)$, where $a, b \neq 0$ are two nonzero scalars. Using the form (5.6), $q(u, v; \varphi, \theta)$ can be found as follows:

$$\begin{aligned} q(u, v; \varphi, \theta) = & \iiint f(x', y', z')\, \delta(ax' \cos\varphi + ay' \sin\varphi - u) \\ & \cdot \delta(ax' \sin\varphi \sin\theta - ay' \cos\varphi \sin\theta + bz' \cos\theta - v)\, \left|a^2 b\right| \mathrm{d}x'\, \mathrm{d}y'\, \mathrm{d}z', \end{aligned} \tag{5.8}$$

with change of variables $x' = x/a$, $y' = y/a$ and $z' = z/b$. Using Dirac impulse properties, we rewrite (5.8) as follows:

$$\begin{aligned} q(u, v; \varphi, \theta) = & \iiint f(x', y', z')\, \delta\Big(x' \cos\varphi + y' \sin\varphi - \frac{u}{a}\Big) \\ & \cdot \delta\Big(\frac{a \sin\theta}{c(\theta)} x' \sin\varphi - \frac{a \sin\theta}{c(\theta)} y' \cos\varphi + \frac{b \cos\theta}{c(\theta)} z' - \frac{v}{c(\theta)}\Big) \\ & \cdot \frac{|ab|}{c(\theta)}\, \mathrm{d}x'\, \mathrm{d}y'\, \mathrm{d}z' \\ = & \iiint f(x', y', z')\, \delta\Big(x' \cos\varphi + y' \sin\varphi - \frac{u}{a}\Big) \\ & \cdot \delta\Big(x' \sin\varphi \sin\theta' - y' \cos\varphi \sin\theta' + z' \cos\theta' - \frac{v}{c(\theta)}\Big) \\ & \cdot \frac{|ab|}{c(\theta)}\, \mathrm{d}x'\, \mathrm{d}y'\, \mathrm{d}z', \end{aligned}$$

where

$$\begin{aligned} \theta' & \triangleq \arctan\Big(\frac{a}{b} \tan\theta\Big) \\ c(\theta) & \triangleq \sqrt{a^2 \sin^2\theta + b^2 \cos^2\theta}. \end{aligned}$$

Then we have the following *scaling property*:

$$f\left(\frac{x}{a}, \frac{y}{a}, \frac{z}{b}\right) \overset{\text{3D Xray}}{\longleftrightarrow} \frac{|ab|}{c(\theta)}\, p\left(\frac{u}{a}, \frac{v}{c(\theta)}; \varphi, \arctan\left(\frac{a}{b}\tan\theta\right)\right). \tag{5.9}$$

In the special case where $a = b = \Delta$:

$$f\left(\frac{\vec{x}}{\Delta}\right) \overset{\text{3D Xray}}{\longleftrightarrow} \Delta\, p\left(\frac{u}{\Delta}, \frac{v}{\Delta}; \varphi, \theta\right).$$

5.2 Variance Predictions for 3D Cone-Beam Tomography

The covariance matrix in (4.7) for quadratically penalized likelihood estimators and the local shift-invariance approximations derived in section 4.2 are applicable for 3D tomography. For the completeness of this chapter, we briefly state the results here. The $p \times p$ covariance matrix is given as the following:

$$\boldsymbol{K} \triangleq \mathsf{Cov}\{\hat{\boldsymbol{\mu}}\} \approx (\boldsymbol{A}'\boldsymbol{W}\boldsymbol{A} + \alpha\boldsymbol{R})^{-1}\boldsymbol{A}'\boldsymbol{W}\boldsymbol{A}(\boldsymbol{A}'\boldsymbol{W}\boldsymbol{A} + \alpha\boldsymbol{R})^{-1}, \tag{5.10}$$

where $\boldsymbol{\mu} = [\mu_1, \ldots, \mu_p]'$, $\boldsymbol{A}$ is the system matrix, $\boldsymbol{Y} = [y_1, \ldots, y_n]'$ denotes the noisy measurements, $\boldsymbol{R}$ is the Hessian matrix of the roughness penalty and α is the regularization parameter controlling the noise and resolution trade-off.

In the spirit of the local shift-invariance approximations presented in section 4.2, we first approximate the covariance matrix in (5.10) near a given location $\vec{n}_0$ as follows:

$$\begin{aligned} \boldsymbol{K} &\approx \boldsymbol{K}_0 \triangleq \mathbf{T}'\breve{\boldsymbol{K}}_0\mathbf{T} \\ \breve{\boldsymbol{K}}_0 &\triangleq (\mathsf{F}_0 + \alpha\boldsymbol{R}_0)^{-1}\mathsf{F}_0(\mathsf{F}_0 + \alpha\boldsymbol{R}_0)^{-1}, \end{aligned}$$

where F_0 and $\boldsymbol{R}_0$ are the $N_1N_2N_3 \times N_1N_2N_3$ *block Toeplitz with Toeplitz blocks* (*BTTB*) approximations corresponding to $\boldsymbol{A}'\boldsymbol{W}\boldsymbol{A}$ and $\boldsymbol{R}$, respectively. In practical computation of predicting variances at a few image locations, circulant approximations and DFTs are usually used as follows [75, 91]:

$$\mathsf{Var}\{\hat{\mu}[\vec{n}_0]\} \approx \langle \boldsymbol{K}_0\mathbf{e}_{\vec{n}_0},\, \mathbf{e}_{\vec{n}_0}\rangle \approx \frac{1}{N_1N_2N_3}\sum_{\vec{k}=\vec{0}}^{\vec{N}-1} P_{d0}[\vec{k}], \tag{5.11}$$

where $\vec{N} = (N_1, N_2, N_3)$, $\mathbf{e}_{\vec{n}_0}$ corresponds to $\vec{n}_0$ and

$$P_{d0}[\vec{k}] \triangleq \frac{\Gamma_0[\vec{k}]}{(\Gamma_0[\vec{k}] + \alpha\Omega_0[\vec{k}])^2},$$

with

$$\begin{aligned} \mathsf{F}_0 &\approx \boldsymbol{Q}\boldsymbol{\Gamma}_0\boldsymbol{Q}' \\ \boldsymbol{R}_0 &\approx \boldsymbol{Q}\boldsymbol{\Omega}_0\boldsymbol{Q}', \end{aligned}$$

where $\boldsymbol{Q}$ is the 3D (N_1, N_2, N_3)-point orthonormal DFT matrix, and $\boldsymbol{\Gamma}_0$ and $\boldsymbol{\Omega}_0$ are diagonal matrices with diagonal elements $\Gamma_0[\vec{k}]$ and $\Omega_0[\vec{k}]$ that are the 3D DFT coefficients of the local impulse response of $\boldsymbol{A}'\boldsymbol{W}\boldsymbol{A}$ and $\boldsymbol{R}$ near $\vec{n}_0$, respectively. Computing this DFT approximation is still expensive for realistic image sizes when the variance is computed for all or many pixels, particularly for shift-variant systems like fan-beam CT and cone-beam CT.

We have discussed in Chapter 4 "analytical" approaches to predict the approximate variance maps of 2D images that are reconstructed by penalized-likelihood estimation with quadratic regularization in fan-beam geometries [105,107]. In this chapter, we extend these approaches to 3D cylindrical cone-beam CT by applying the same principles: *local shift invariance approximation* and *local Fourier analysis*.

We next approximate (5.11) by the 3D discrete-space Fourier transform (DSFT) as follows:

$$\mathsf{Var}\{\hat{\mu}[\vec{n}_0]\} \approx \int_{-\pi}^{\pi}\int_{-\pi}^{\pi}\int_{-\pi}^{\pi} P_{d0}(\vec{\omega}) \frac{\mathrm{d}\vec{\omega}}{(2\pi)^3}, \tag{5.12}$$

where $P_{d0}(\vec{\omega})$ is the local spectrum of the covariance matrix, given as follows:

$$P_{d0}(\vec{\omega}) \triangleq \frac{H_{\mathrm{d0}}(\vec{\omega})}{[H_{\mathrm{d0}}(\vec{\omega}) + \alpha R_{\mathrm{d0}}(\vec{\omega})]^2}, \tag{5.13}$$

where $H_{\mathrm{d0}}(\vec{\omega})$ is the local frequency response of the Gram matrix $\boldsymbol{A}'\boldsymbol{W}\boldsymbol{A}$ and $R_{\mathrm{d0}}(\vec{\omega})$ is the local frequency response of $\boldsymbol{R}$ near $\vec{n}_0$.

Let $\vec{\Delta} = (\Delta_\text{X}, \Delta_\text{Y}, \Delta_\text{Z})$ denote the sample spacings in the reconstructed image. Make the change of variable, $\vec{\omega} = (2\pi\varrho)\vec{\Delta}\odot\vec{e}_{\Phi,\Theta}$ where $\vec{e}_{\Phi,\Theta} = (\cos\Phi\cos\Theta, \sin\Phi\cos\Theta, \sin\Theta)$, and $\odot$ denotes element-by-element multiplication. We rewrite (5.12) in terms of spherical frequency coordinates (ϱ, Φ, Θ) as follows:

$$\text{(5.14)} \qquad \mathsf{Var}\{\hat{\mu}[\vec{n}_0]\} \approx \Delta_\text{X}\Delta_\text{Y}\Delta_\text{Z} \int_{-\frac{\pi}{2}}^{\frac{\pi}{2}} \int_0^{2\pi} \int_0^{\varrho_\text{max}(\Phi,\Theta)} P_0(\varrho, \Phi, \Theta)\varrho^2 \left|\cos\Theta\right| \mathrm{d}\varrho \,\mathrm{d}\Phi \,\mathrm{d}\Theta,$$

where $\varrho_\text{max}(\Phi, \Theta) = \frac{1}{2}\max\left(\frac{|\cos\Phi\cos\Theta|}{\Delta_\text{X}}, \frac{|\sin\Phi\cos\Theta|}{\Delta_\text{Y}}, \frac{|\sin\Theta|}{\Delta_\text{Z}}\right)$, and we define

$$\begin{aligned} P_0(\varrho, \Phi, \Theta) &\triangleq P_\text{d0}(2\pi\varrho\vec{\Delta}\odot\vec{e}_{\Phi,\Theta}) \\ &= \frac{H_0(\varrho, \Phi, \Theta)}{[H_0(\varrho, \Phi, \Theta) + \alpha R_0(\varrho, \Phi, \Theta)]^2}. \end{aligned} \qquad \text{(5.15)}$$

We define H_0 and R_0 similarly in terms of H_d0 and R_d0. By finding analytical expressions for H_0 and R_0, the approximation (5.14) can lead to faster alternatives to the DFT approach (5.11). The variance prediction in (5.14) is applicable to any 3D CT geometry. We focus on cylindrical 3D cone-beam CT here. To use (5.14), we need to find $H_0(\varrho, \Phi, \Theta)$ and $R_0(\varrho, \Phi, \Theta)$ first.

5.2.1 Cylindrical Cone-Beam Geometry

Consider an ideal "cylindrical" cone-beam tomography: the source can be at any point on a cylinder of radius D_s0 centered along the z-axis, see Figure 5.1. The step-and-shoot cone-beam CT and helical cone beam CT are two examples of cylindrical cone-beam geometry with different sampling patterns. The source position $\vec{p}_0$ can be parameterized by two variables (β, ζ) as follows:

$$\text{(5.16)} \qquad \vec{p}_0 = \begin{pmatrix} -D_\text{s0}\sin\beta \\ D_\text{s0}\cos\beta \\ \zeta \end{pmatrix},$$

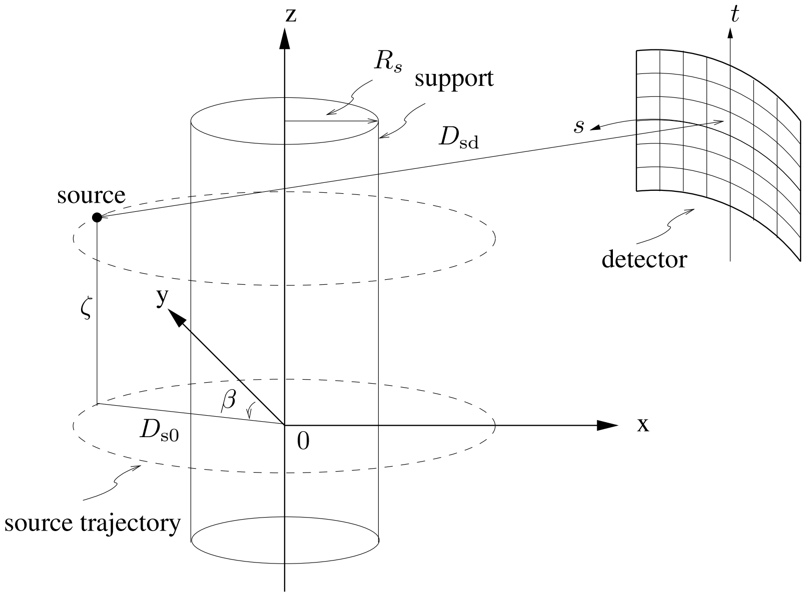

Figure 5.1: Cylindrical cone-beam geometry with 2D cylindrical detector that moves with the cone vertex.

where D_{s0} is the source to rotation center distance, β is the angle of the source relative to the y axis, and ζ is the z-axis position of source.

We focus on a 2D cylindrical detector that moves with the cone vertex here. We assume that the detector arc has the X-ray source as its focal point, as in a 3rd-generation CT system. We introduce local/relative coordinates (s, t) on the detector face, where s is the arc length along each row, and the t-axis is parallel to the z-axis. A point on the 2D detector can be expressed as

$$\vec{p}_1 = \begin{pmatrix} D_{\mathrm{sd}} \sin\gamma \cos\beta + (D_{\mathrm{sd}} \cos\gamma - D_{\mathrm{s0}}) \sin\beta \\ D_{\mathrm{sd}} \sin\gamma \sin\beta - (D_{\mathrm{sd}} \cos\gamma - D_{\mathrm{s0}}) \cos\beta \\ t + \zeta \end{pmatrix} = \begin{pmatrix} D_{\mathrm{sd}} \sin\varphi \\ -D_{\mathrm{sd}} \cos\varphi \\ t \end{pmatrix} + \vec{p}_0, \tag{5.17}$$

where $D_{\mathrm{0d}} = D_{\mathrm{sd}} - D_{\mathrm{s0}}$ is the isocenter to detector distance and

$$\gamma = \gamma(s) \triangleq \frac{s}{D_{\mathrm{sd}}} \tag{5.18}$$

$$\varphi = \varphi(s, \beta) \triangleq \gamma(s) + \beta. \tag{5.19}$$

The direction vector of a ray from $\vec{p}_0$ to $\vec{p}_1$ can then be expressed as

$$\begin{aligned} \vec{e}_3 &= \frac{\vec{p}_1 - \vec{p}_0}{\|\vec{p}_1 - \vec{p}_0\|} \\ &= \frac{1}{\sqrt{t^2 + D_{\mathrm{sd}}^2}} \begin{pmatrix} D_{\mathrm{sd}} \sin\varphi \\ -D_{\mathrm{sd}} \cos\varphi \\ t \end{pmatrix} = \begin{pmatrix} \sin\varphi \cos\theta \\ -\cos\varphi \cos\theta \\ \sin\theta \end{pmatrix}, \end{aligned} \tag{5.20}$$

where

$$\theta = \theta(t) \triangleq \arctan\left(\frac{t}{D_{\mathrm{sd}}}\right). \tag{5.21}$$

The parallel-beam projection plane is perpendicular to $\vec{e}_3$, specified by $\vec{e}_1$ and $\vec{e}_2$. The corresponding Cartesian coordinates (u, v) can be found by

$$\begin{aligned} u &= \vec{p}_1 \cdot \vec{e}_1 = D_{\mathrm{sd}} \sin\gamma \cos\gamma - (D_{\mathrm{sd}} \cos\gamma - D_{\mathrm{s0}}) \sin\gamma \\ &= D_{\mathrm{s0}} \sin\gamma(s) \end{aligned} \tag{5.22}$$

$$\begin{aligned} v &= \vec{p}_1 \cdot \vec{e}_2 = -D_{\mathrm{sd}} \sin\theta + D_{\mathrm{s0}} \cos\gamma \sin\theta + (t + \zeta) \cos\theta \\ &= D_{\mathrm{s0}} \cos\gamma(s) \sin\theta + \zeta \cos\theta, \end{aligned} \tag{5.23}$$

since $-D_{\mathrm{sd}} \sin\theta + t \cos\theta = 0$.

Combining (5.18), (5.19), (5.21), (5.22) and (5.23), we have the the following (cylindrical) cone-to-parallel rebinning relations:

$$\tilde{\gamma}(s) \triangleq \frac{s}{D_{\mathrm{sd}}} \tag{5.24}$$

$$\tilde{\varphi}(s, \beta) \triangleq \gamma(s) + \beta \tag{5.25}$$

$$\tilde{\theta}(t) \triangleq \arctan\left(\frac{t}{D_{\mathrm{sd}}}\right) \tag{5.26}$$

$$\tilde{u}(s) = D_{\mathrm{s0}} \sin\gamma(s) \tag{5.27}$$

$$\tilde{v}(s, t, \zeta) = D_{\mathrm{s0}} \cos\gamma(s) \sin\tilde{\theta}(t) + \zeta \cos\tilde{\theta}(t). \tag{5.28}$$

The inverse relations can be derived directly, given as follows:

$$\tilde{s}(u) \triangleq D_{\mathrm{sd}} \arcsin \frac{u}{D_{\mathrm{s0}}} \tag{5.29}$$

$$\tilde{t}(\theta) \triangleq D_{\mathrm{sd}} \tan\theta \tag{5.30}$$

$$\tilde{\beta}(\varphi, u) \triangleq \varphi - \arcsin \frac{u}{D_{\mathrm{s0}}} \tag{5.31}$$

$$\begin{aligned} \tilde{\zeta}(u, v, \theta) &\triangleq \frac{v}{\cos\theta} - D_{\mathrm{s0}} \cos\tilde{\gamma}(\tilde{s}(u)) \tan\theta \\ &= \frac{v}{\cos\theta} - \sqrt{{D_{\mathrm{s0}}}^2 - u^2} \tan\theta. \end{aligned} \tag{5.32}$$

5.2.2 Analysis for Cone-Beam Gram Matrix

To predict variance images using (5.12), we need to determine the local frequency response $H_0(\rho, \Phi, \Theta)$, or equivalently $H_{\mathrm{d0}}(\vec{\omega})$. We first find the local impulse response.

Local Impulse Response of Gram Matrix

Consider the 3D object model based on a common basis function $\chi(\vec{x})$ superimposed on a $N_1 \times N_2 \times N_3$ Cartesian grid as follows:

$$\mu(\vec{x}) = \sum_{\vec{n} \in \mathcal{S}} \mu[\vec{n}]\, \chi\left(\frac{1}{\vec{\Delta}} \odot (\vec{x} - \vec{x}_c[\vec{n}]) \right), \tag{5.33}$$

where $\mathcal{S} \triangleq \{\vec{n}_j : j = 1, \ldots, p\}$ denotes the subset of the $N_1 \times N_2 \times N_3$ lattice that is estimated and $\vec{x}_c[\vec{n}]$ denotes the center of the $\vec{n}$th basis function (see Figure 4.1). The grid spacing is $\vec{\Delta} = (\Delta_{\mathrm{X}}, \Delta_{\mathrm{Y}}, \Delta_{\mathrm{Z}})$. We consider the case $\Delta_{\mathrm{X}} = \Delta_{\mathrm{Y}}$ hereafter, but we allow $\Delta_{\mathrm{X}} \neq \Delta_{\mathrm{Z}}$. Typically

$$\begin{aligned} \vec{x}_c[\vec{n}] &= (\vec{n} - \vec{w}_{\vec{x}}) \odot \vec{\Delta}, \quad \vec{n} \in \mathcal{S} \\ \vec{w}_{\vec{x}} &= (\vec{N} - 1)/2 + \vec{c}_{\vec{x}}, \end{aligned}$$

where the user-selectable parameter $\vec{c}_{\vec{x}}$ denotes an optional spatial offset for the object center.

Assume that the detector blur $b(s,t)$ is shift invariant, independent of source position (β, ζ) and acts only along the s and t coordinates. (This could be generalized to the case of locally shift-invariant blur.) Then we model the mean projections as follows:

$$\bar{y}_\varphi[s_k, t_\ell; \beta, \zeta] = \iint b(s_k - s', t_\ell - t')\, p\Big(\tilde{u}(s'), \tilde{v}(s', t', \zeta); \tilde{\varphi}(s', \beta), \tilde{\theta}(t')\Big)\, \mathrm{d}s'\, \mathrm{d}t' \tag{5.34}$$

for

$$\begin{aligned} s_k &= (k - w_{\mathrm{S}})\Delta_{\mathrm{S}} \\ t_\ell &= (\ell - w_t)\Delta_t \end{aligned}$$

and $k = 0, \ldots, n_s - 1; \ell = 0, \ldots, n_t - 1$, where Δ_{S} is the sample spacing in s, Δ_t is the sample spacing in t, w_{S} and w_t are defined akin to $\vec{w}_{\vec{x}}$, and $p(u, v; \varphi, \theta)$ is the line integral of $\mu(\vec{x})$ defined in (5.3).

Let $g(u, v; \varphi, \theta)$ denote the Radon transform of $\chi(\vec{x})$ at angle (φ, θ). By shifting and scaling properties of Radon transform in (5.7) and (5.9), we have

$$\chi\left(\frac{1}{\vec{\Delta}} \odot (\vec{x} - \vec{x}_c[\vec{n}])\right) \xleftrightarrow{\text{3D Xray}} \frac{\Delta_{\mathrm{X}}\Delta_{\mathrm{Z}}}{c(\theta)}\, g\left(\frac{u - u_\varphi[\vec{n}]}{\Delta_{\mathrm{X}}}, \frac{v - v_{\varphi,\theta}[\vec{n}]}{c(\theta)}; \varphi, \arctan\left(\frac{\Delta_{\mathrm{X}}}{\Delta_{\mathrm{Z}}} \tan\theta\right)\right),$$

where $c(\theta) \triangleq \sqrt{\Delta_{\mathrm{X}}^2 \sin^2\theta + \Delta_{\mathrm{Z}}^2 \cos^2\theta}$ and

$$u_\varphi[\vec{n}] \triangleq \vec{x}_c[\vec{n}] \cdot \vec{e}_1(\varphi) \tag{5.35}$$

$$v_{\varphi,\theta}[\vec{n}] \triangleq \vec{x}_c[\vec{n}] \cdot \vec{e}_2(\varphi, \theta). \tag{5.36}$$

Substituting the basis expansion model in (5.33) for the object into the measurement model (5.34) and simplifying leads to the linear model

$$\bar{y}_\varphi[s_k, t_\ell; \beta, \zeta] = \sum_{\vec{n} \in \mathcal{S}} a(s_k, t_\ell; \beta, \zeta; \vec{n})\mu[\vec{n}],$$

where the cone-beam system matrix elements are samples of the following cone-beam projection of a single basis function centered at $\vec{x}_c[\vec{n}]$:

$$\begin{aligned} a(s,t;\beta,\zeta;\vec{n}) \;=\; & \iint b(s-s',t-t')\,\frac{\Delta_{\mathrm{X}}\Delta_{\mathrm{Z}}}{c(\tilde{\theta}(t'))} \\ \cdot\, g & \left(\frac{\tilde{u}(s') - u_{\tilde{\varphi}(s',\beta)}[\vec{n}]}{\Delta_{\mathrm{X}}}, \frac{\tilde{v}(s',t',\zeta) - v_{\tilde{\varphi}(s',\beta),\tilde{\theta}(t')}[\vec{n}]}{c(\tilde{\theta}(t'))}; \tilde{\varphi}(s',\beta), \tilde{\theta}\left(\frac{\Delta_{\mathrm{X}}}{\Delta_{\mathrm{Z}}}t'\right)\right) \mathrm{d}s'\,\mathrm{d}t', \end{aligned} \tag{5.37}$$

where

$$\arctan\left(\frac{\Delta_{\mathrm{X}}}{\Delta_{\mathrm{Z}}}\tan\tilde{\theta}(t')\right) = \arctan\left(\frac{\Delta_{\mathrm{X}}}{\Delta_{\mathrm{Z}}}\frac{t'}{D_{\mathrm{sd}}}\right) = \tilde{\theta}\left(\frac{\Delta_{\mathrm{X}}}{\Delta_{\mathrm{Z}}}t'\right). \tag{5.38}$$

To proceed, we rebin (5.37) into parallel coordinates by defining $a_p(u,v;\varphi,\theta;\vec{n})$ in terms of $a(s,t;\beta,\zeta;\vec{n})$ using (5.29) – (5.32).

Next we reparameterize variables s' and t' in (5.37) according to the inversion of cone-to-parallel rebinning as follows: $s' \to \tilde{s}(u'), t' \to \tilde{t}(\theta')$, and use first-order Taylor expansion to expand $s(u)$ around $s'(u')$ as follows:

$$s(u) - s(u') \approx m_s(u')(u-u'), \tag{5.39}$$

where we define the following magnification factor

$$m_s(u') \triangleq \left.\frac{\partial\tilde{s}}{\partial u}(u)\right|_{u=u'} = \frac{D_{\mathrm{sd}}}{D_{\mathrm{s0}}\cos\tilde{\gamma}(\tilde{s}(u'))} = \frac{D_{\mathrm{sd}}}{\sqrt{{D_{\mathrm{s0}}}^2 - u^2}}. \tag{5.40}$$

Similarly,

$$\tilde{t}(\theta) - \tilde{t}(\theta') \approx m_t(\theta')(\theta-\theta'), \tag{5.41}$$

where

$$m_t(\theta') \triangleq \left.\frac{\partial\tilde{t}}{\partial\theta}(\theta)\right|_{\theta=\theta'} = \frac{D_{\mathrm{sd}}}{\cos^2\theta'}. \tag{5.42}$$

Because the blur $b(s,t)$ is assumed to be about 1-2 detector pixels wide, we expect $\theta' \approx \theta$

within (5.37) , leading to the following equalities and approximations:

$$\begin{aligned}
\tilde{\theta}(\tilde{t}(\theta')) &= \theta' \\
\tilde{u}(\tilde{s}(u')) &= u' \\
\tilde{\varphi}(\tilde{s}(u'), \tilde{\beta}(\varphi, u)) &= \varphi + \arcsin \frac{u'}{D_{\mathrm{sd}}} - \arcsin \frac{u}{D_{\mathrm{sd}}} \approx \varphi \\
\tilde{\theta}\left(\frac{\Delta_{\mathrm{X}}}{\Delta_{\mathrm{Z}}} \tilde{t}(\theta')\right) &= \arctan\left(\frac{\Delta_{\mathrm{X}}}{\Delta_{\mathrm{Z}}} \tan\theta'\right) \triangleq \vartheta(\theta') \\
\tilde{v}(\tilde{s}(u'), \tilde{t}(\theta'), \tilde{\zeta}(u, v, \theta)) &= D_{\mathrm{s0}} \cos\tilde{\gamma}(\tilde{s}(u')) \sin\theta' + \left[\frac{v}{\cos\theta} - D_{\mathrm{s0}} \cos\tilde{\gamma}(\tilde{s}(u)) \tan\theta\right] \cos\theta' \\
&\approx \frac{v\cos\theta'}{\cos\theta} - D_{\mathrm{s0}} \cos\tilde{\gamma}(\tilde{s}(u')) \cos\theta' (\tan\theta - \tan\theta') \\
&\approx v - U(u', \theta')(\theta - \theta'), \qquad (5.43)
\end{aligned}$$

where

$$U(u', \theta') \triangleq D_{\mathrm{s0}} \cos\theta' \cos\tilde{\gamma}(\tilde{s}(u')) = (\cos\theta') \sqrt{{D_{\mathrm{s0}}}^2 - u^2}. \tag{5.44}$$

We assume these approximations hold for (s', t') sufficiently close to (s, t), *i.e.*, within the essential support of $b(s, t)$.

With (5.39), (5.41), (5.37) and the above, we approximate the parallel-rebinned system matrix elements as follows:

$$\begin{aligned}
a_p(u, v; \varphi, \theta; \vec{n}) \triangleq\, & a(\tilde{s}(u), \tilde{t}(\theta); \tilde{\beta}(u, \varphi), \tilde{\zeta}(u, v, \theta); \vec{n}) \\
&\approx \iint b(m_s(u')(u - u'), m_t(\theta')(\theta - \theta')) \, \frac{\Delta_{\mathrm{X}} \Delta_{\mathrm{Z}}}{c(\theta')} \\
&\quad \cdot g\left(\frac{u' - u_{\varphi}[\vec{n}]}{\Delta_{\mathrm{X}}}, \frac{v - U(u', \theta')(\theta - \theta') - v_{\varphi, \theta'}[\vec{n}]}{c(\theta')}; \varphi, \vartheta(\theta')\right) |m_s(u') m_t(\theta')| \, \mathrm{d}u' \, \mathrm{d}\theta' \\
&\approx \iint b(m_s(u)(u - u'), m_t(\theta)(\theta - \theta')) \, \frac{\Delta_{\mathrm{X}} \Delta_{\mathrm{Z}}}{c(\theta)} \\
&\quad \cdot g\left(\frac{u' - u_{\varphi}[\vec{n}]}{\Delta_{\mathrm{X}}}, \frac{v - U(u, \theta)(\theta - \theta') - v_{\varphi, \theta}[\vec{n}]}{c(\theta)}; \varphi, \vartheta(\theta)\right) |m_s(u) m_t(\theta)| \, \mathrm{d}u' \, \mathrm{d}\theta' \, . \qquad (5.45)
\end{aligned}$$

Making the change variable of $v' = v - U(u,\theta)(\theta - \theta')$ yields

$$\begin{aligned} a_p(u,v;\varphi,\theta;\vec{n}) \approx & \iint b(m_s(u)(u-u'), m_{s,t}(u,\theta)(v-v'))\, \frac{\Delta_{\mathrm{X}}\Delta_{\mathrm{Z}}}{c(\theta)} \\ & \cdot g\!\left(\frac{u'-u_\varphi[\vec{n}]}{\Delta_{\mathrm{X}}}, \frac{v'-v_{\varphi,\theta}[\vec{n}]}{c(\theta)}; \varphi, \vartheta(\theta)\right) |m_s(u) m_{s,t}(u,\theta)| \,\mathrm{d}u'\,\mathrm{d}v', \end{aligned} \tag{5.46}$$

where

$$m_{s,t}(u,\theta) \triangleq \frac{m_t(\theta)}{U(u,\theta)} = \frac{D_{\mathrm{sd}}}{D_{\mathrm{s0}} \cos\theta \cos\tilde{\gamma}(\tilde{s}(u))}. \tag{5.47}$$

Consider $\vec{n}$ and $\vec{n}'$ values that are sufficiently close to $\vec{n}_0$, the location of interest. Let $u_0(\varphi) \triangleq u_\varphi[\vec{n}_0], v_0(\varphi,\theta) \triangleq v_{\varphi,\theta}[\vec{n}_0]$. and $v_0(\varphi,\theta) \triangleq v_{\varphi,\theta}[\vec{n}_0]$. Because $m_s(u)$ and $m_{s,t}(u,\theta)$ are fairly smooth over (u,v), we approximate the local magnification factors by their values at the center of the voxel of interest $\vec{n}_0$:

$$m_s(u) \approx m_s(u_0(\varphi)) \triangleq m_{s,0}(\varphi) \tag{5.48}$$

$$m_{s,t}(u,\theta) \approx m_{s,t}(u_0(\varphi),\theta) \triangleq m_{s,t,0}(\varphi,\theta). \tag{5.49}$$

Therefore, we further approximate (5.46) using (5.48) and (5.49) as follows:

$$\begin{aligned} a_p(u,v;\varphi,\theta;\vec{n}) \approx & \, a_0(u-u_\varphi[\vec{n}], v-v_{\varphi,\theta}[\vec{n}];\varphi,\theta) \\ \triangleq & \iint b_0(u-u_\varphi[\vec{n}]-u'', v-v_{\varphi,\theta}[\vec{n}]-v'';\varphi,\theta) \\ & \cdot \frac{\Delta_{\mathrm{X}}\Delta_{\mathrm{Z}}}{c(\theta)}\, g\!\left(\frac{u''}{\Delta_{\mathrm{X}}}, \frac{v''}{c(\theta)}; \varphi, \vartheta(\theta)\right) \mathrm{d}u''\,\mathrm{d}v'', \end{aligned} \tag{5.50}$$

where

$$b_0(u,v;\varphi,\theta) \triangleq |m_{s,0}(\varphi) m_{s,t,0}(\varphi,\theta)|\, b(m_{s,0}(\varphi)\, u, m_{s,t,0}(\varphi,\theta) v) \tag{5.51}$$

$$a_0(u,v;\varphi,\theta) \triangleq \iint b_0(u-u', v-v')\, \frac{\Delta_{\mathrm{X}}\Delta_{\mathrm{Z}}}{c(\theta)}\, g\!\left(\frac{u'}{\Delta_{\mathrm{X}}}, \frac{v'}{c(\theta)}; \varphi, \vartheta(\theta)\right) \mathrm{d}u'\,\mathrm{d}v'\,. \tag{5.52}$$

The second line of (5.50) uses change of variables $u'' = u' - u_\varphi[\vec{n}], v'' = v' - v_{\varphi,\theta}[\vec{n}]$.

Now the elements of the *Gram matrix* are given exactly by

$$
\begin{aligned}
h_{\mathrm{d}}[\vec{n};\vec{n}'] &= \begin{cases} [\boldsymbol{A}'\boldsymbol{W}\boldsymbol{A}]_{jj'}, & \vec{n}=\vec{n}_j\in\mathcal{S}, \vec{n}'=\vec{n}_{j'}\in\mathcal{S} \\ 0, & \text{otherwise} \end{cases} \\
&= \breve{h}_{\mathrm{d}}[\vec{n};\vec{n}']\eta(\vec{x}_c[\vec{n}])\eta(\vec{x}_c[\vec{n}']) \qquad (5.53)
\end{aligned}
$$

where

$$
\breve{h}_{\mathrm{d}}[\vec{n};\vec{n}'] = \sum_{k=1}^{n_s}\sum_{l=1}^{n_t}\sum_{i=1}^{n_\beta}\sum_{j=1}^{n_\zeta} w(s_k,t_\ell;\beta_i,\zeta_j)\, a(s_k,t_\ell;\beta_i,\zeta_j;\vec{n})a(s_k,t_\ell;\beta_i,\zeta_j;\vec{n}'),
$$

and $\eta(\vec{x}_c[\vec{n}]) \triangleq 1_{\{\vec{n}\in\mathcal{S}\}}$, and $w(s,t;\beta,\zeta)$ denotes the statistical weighting associated with $\boldsymbol{W}$. We first use the *integrals* to approximate the summations in (5.53) as follows:

$$
\begin{aligned}
\breve{h}_{\mathrm{d}}[\vec{n};\vec{n}'] \approx \Pi \int_{-\infty}^{\infty}\int_{0}^{2\pi}\int_{-\infty}^{\infty}\int_{-\infty}^{\infty} & w(s,t;\beta,\zeta)\mathrm{rect}\left(\frac{s}{2s_{\max}}\right)\mathrm{rect}\left(\frac{t}{2t_{\max}}\right)\mathrm{rect}\left(\frac{\zeta}{2\zeta_{\max}}\right) \\
& \cdot a(s,t;\beta,\zeta;\vec{n})a(s,t;\beta,\zeta;\vec{n}')\,\mathrm{d}s\,\mathrm{d}t\,\mathrm{d}\beta\,\mathrm{d}\zeta, \qquad (5.54)
\end{aligned}
$$

where

$$
\Pi \triangleq \frac{1}{\Delta_{\mathrm{S}}}\frac{1}{\Delta_t}\frac{1}{\Delta_\beta}\frac{1}{\Delta_\zeta},
$$

and $\Delta_{\mathrm{S}}, \Delta_t, \Delta_\beta$ and Δ_ζ are the sampling intervals in s, t, β and ζ. Notice that $\breve{h}_{\mathrm{d}}[\vec{n};\vec{n}']$ in (5.54) is not shift invariant. Making a change of variables from cone-beam coordinates to parallel-beam coordinates, we rewrite (5.54) as

(5.55)

$$
\breve{h}_{\mathrm{d}}[\vec{n};\vec{n}'] \approx \Pi\int_{-\frac{\pi}{2}}^{\frac{\pi}{2}}\int_{0}^{2\pi}\int_{-\infty}^{\infty}\int_{-\infty}^{\infty}\bar{w}(u,v;\varphi,\theta)a_p(u,v;\varphi,\theta;\vec{n})a_p(u,v;\varphi,\theta;\vec{n}')J(u,\theta)\,\mathrm{d}u\,\mathrm{d}v\,\mathrm{d}\varphi\,\mathrm{d}\theta,
$$

where $\bar{w}(u,v;\varphi,\theta)$ is the rebinned statistical weighting defined as follows:

$$
\begin{aligned}
\bar{w}(u,v;\varphi,\theta) &\triangleq w(s(u),t(\theta);\beta(\varphi,u),\zeta(u,v,\theta))\,\mathrm{rect}_3\left(\frac{s(u)}{2s_{\max}},\frac{t(\theta)}{2t_{\max}},\frac{\zeta(u,v,\zeta)}{2\zeta_{\max}}\right) \\
&\approx w(s(u),t(\theta);\beta(\varphi,u),\zeta(u,v,\theta))\,\mathrm{rect}_3\left(\frac{u}{2u_{\max}},\frac{\theta}{2\theta_{\max}},\frac{v}{2\zeta_{\max}\cos\theta}\right), \qquad (5.56)
\end{aligned}
$$

for small θ, $\operatorname{rect}_3(\vec{x}) \triangleq \operatorname{rect}(x)\operatorname{rect}(y)\operatorname{rect}(z)$ and $u_{\text{max}} \triangleq \tilde{u}(s_{\text{max}}), \theta_{\text{max}} \triangleq \tilde{\theta}(t_{\text{max}})$. The absolute value of the determinant of the Jacobian matrix $J(u,\theta)$ is given by

$$\begin{aligned}
J(u,\theta) &= \begin{vmatrix} \frac{\partial\tilde{s}}{\partial u} & \frac{\partial\tilde{s}}{\partial v} & \frac{\partial\tilde{s}}{\partial\varphi} & \frac{\partial\tilde{s}}{\partial\theta} \\ \frac{\partial\tilde{t}}{\partial u} & \frac{\partial\tilde{t}}{\partial v} & \frac{\partial\tilde{t}}{\partial\varphi} & \frac{\partial\tilde{t}}{\partial\theta} \\ \frac{\partial\tilde{\beta}}{\partial u} & \frac{\partial\tilde{\beta}}{\partial v} & \frac{\partial\tilde{\beta}}{\partial\varphi} & \frac{\partial\tilde{\beta}}{\partial\theta} \\ \frac{\partial\tilde{\zeta}}{\partial u} & \frac{\partial\tilde{\zeta}}{\partial v} & \frac{\partial\tilde{\zeta}}{\partial\varphi} & \frac{\partial\tilde{\zeta}}{\partial\theta} \end{vmatrix} = \begin{vmatrix} \frac{\partial\tilde{s}}{\partial u} & 0 & 0 & 0 \\ 0 & 0 & 0 & \frac{\partial\tilde{t}}{\partial\theta} \\ \frac{\partial\tilde{\beta}}{\partial u} & 0 & \frac{\partial\tilde{\beta}}{\partial\varphi} & 0 \\ \frac{\partial\tilde{\zeta}}{\partial u} & \frac{\partial\tilde{\zeta}}{\partial v} & 0 & \frac{\partial\tilde{\zeta}}{\partial\theta} \end{vmatrix} \\
&= \left| \frac{\partial\tilde{s}}{\partial u}\frac{\partial\tilde{t}}{\partial\theta}\frac{\partial\tilde{\beta}}{\partial\varphi}\frac{\partial\tilde{\zeta}}{\partial v} \right| = \left| \frac{D_{\text{sd}}^2}{\cos^3\theta\sqrt{D_{\text{s0}}^2 - u^2}} \right|. \qquad (5.57)
\end{aligned}$$

We further simplify (5.55) as follows, by analogy with [40] and (4.43) in chapter 4:

$$\breve{h}_{\text{d}}[\vec{n};\vec{n}'] \approx \Pi \int_{-\frac{\pi}{2}}^{\frac{\pi}{2}}\int_0^{2\pi} \breve{w}(\varphi,\theta;\vec{n};\vec{n}')\breve{h}_{\varphi,\theta}[\vec{n};\vec{n}'] \,\mathrm{d}\varphi\,\mathrm{d}\theta, \qquad (5.58)$$

where

$$\breve{w}(\varphi,\theta;\vec{n};\vec{n}') \triangleq \frac{\int_{-\infty}^{\infty}\int_{-\infty}^{\infty} \bar{w}(u,v;\varphi,\theta)a_p(u,v;\varphi,\theta;\vec{n})a_p(u,v;\varphi,\theta;\vec{n}')J(u,\theta)\,\mathrm{d}u\,\mathrm{d}v}{\int_{-\infty}^{\infty}\int_{-\infty}^{\infty} a_p(u,v;\varphi,\theta;\vec{n})a_p(u,v;\varphi,\theta;\vec{n}')\,\mathrm{d}u\,\mathrm{d}v} \qquad (5.59)$$

$$\breve{h}_{\varphi,\theta}[\vec{n};\vec{n}'] \triangleq \int_{-\infty}^{\infty}\int_{-\infty}^{\infty} a_p(u,v;\varphi,\theta;\vec{n})a_p(u,v;\varphi,\theta;\vec{n}')\,\mathrm{d}u\,\mathrm{d}v\,. \qquad (5.60)$$

To further simply (5.58), we approximate (5.59) and (5.60) by using (5.50) and assuming that $\vec{n}$ and $\vec{n}'$ are sufficiently close to $\vec{n}_0$:

$$\begin{aligned}
\breve{w}(\varphi,\theta;\vec{n};\vec{n}') &\approx \frac{\int_{-\infty}^{\infty}\int_{-\infty}^{\infty} \bar{w}(u,v;\varphi,\theta)J(u,\theta)a_0^2(u - u_\varphi[\vec{n}_0], v - v_{\varphi,\theta}[\vec{n}_0])\,\mathrm{d}u\,\mathrm{d}v}{\int_{-\infty}^{\infty}\int_{-\infty}^{\infty} a_0^2(u - u_\varphi[\vec{n}_0], v - v_{\varphi,\theta}[\vec{n}_0])\,\mathrm{d}u\,\mathrm{d}v} \\
&\approx \frac{\int_{-\infty}^{\infty}\int_{-\infty}^{\infty} J_0(\varphi,\theta)\bar{w}(u,v;\varphi,\theta)a_0^2(u - u_0(\varphi), v - v_0(\varphi,\theta))\,\mathrm{d}u\,\mathrm{d}v}{\int_{-\infty}^{\infty}\int_{-\infty}^{\infty} a_0^2(u - u_0(\varphi), v - v_0(\varphi,\theta))\,\mathrm{d}u\,\mathrm{d}v} \\
&\approx J(u_0(\varphi),\theta)\bar{w}(u_0(\varphi), v_0(\varphi,\theta);\varphi,\theta) \\
&\approx J_0(\varphi,\theta)\bar{w}(u_0(\varphi), v_0(\varphi,\theta);\varphi,\theta) \triangleq w_0(\varphi,\theta), \qquad (5.61)
\end{aligned}$$

where the Jacobian determinant at the voxel center is

$$J_0(\varphi,\theta) \triangleq J(u_0(\varphi),\theta) \qquad (5.62)$$

and

$$\begin{aligned}\breve{h}_{\varphi,\theta}[\vec{n};\vec{n}'] &\approx \int_{-\infty}^{\infty}\int_{-\infty}^{\infty} a_0(u-u_\varphi[\vec{n}], v-v_{\varphi,\theta}[\vec{n}])a_0(u-u_\varphi[\vec{n}], v-v_{\varphi,\theta}[\vec{n}'])\,\mathrm{d}u\,\mathrm{d}v \\ &= \int_{-\infty}^{\infty}\int_{-\infty}^{\infty} a_0(u,v;\varphi,\theta)a_0(u+u_\varphi[\vec{n}-\vec{n}'], v+v_{\varphi,\theta}[\vec{n}-\vec{n}'];\varphi,\theta)\,\mathrm{d}u\,\mathrm{d}v \\ &= \breve{h}_0(\vec{\Delta}\odot(\vec{n}-\vec{n}')\cdot\vec{e}_1, \vec{\Delta}\odot(\vec{n}-\vec{n}')\cdot\vec{e}_2;\varphi,\theta), \end{aligned} \tag{5.63}$$

where the following 2D auto-correlation is w. r. t. (u, v):

$$\breve{h}_0(u,v;\varphi,\theta) \triangleq a_0(u,v;\varphi,\theta) \star\star\, a_0(u,v;\varphi,\theta). \tag{5.64}$$

Combining all the approximations above, we have the expression for the local impulse response:

$$h_{\mathrm{d}}[\vec{n};\vec{n}'] \approx \Pi \int_{-\frac{\pi}{2}}^{\frac{\pi}{2}}\int_0^{2\pi} w_0(\varphi,\theta)h_{\varphi,\theta}[\vec{n};\vec{n}']\,\mathrm{d}\varphi\,\mathrm{d}\theta, \tag{5.65}$$

where

$$h_{\varphi,\theta}[\vec{n};\vec{n}'] \triangleq \breve{h}_0(\vec{\Delta}\odot(\vec{n}-\vec{n}')\cdot\vec{e}_1, \vec{\Delta}\odot(\vec{n}-\vec{n}')\cdot\vec{e}_2;\varphi,\theta)\eta(\vec{x}_c[\vec{n}])\eta(\vec{x}_c[\vec{n}']). \tag{5.66}$$

Thus, we now have a form that is nearly shift-invariant (except for edge effects).

As shown in 2D fan-beam case, the edge effects in (5.53) or (5.66) are a main concern in accurate variance prediction. Here we use a similar approach to take the edge effects into account to find the local frequency response. As in 2D fan-beam case, we refer all displacements relative to the point $\vec{n}_0$ as follows:

$$\begin{aligned} h_{\varphi,\theta}[\vec{n};\vec{n}'] &\approx h_{\varphi,\theta}[\vec{n}_0+\vec{n}-\vec{n}';\vec{n}_0] \\ &= \breve{h}_0(\vec{\Delta}\odot(\vec{n}-\vec{n}')\cdot\vec{e}_1, \vec{\Delta}\odot(\vec{n}-\vec{n}')\cdot\vec{e}_2;\varphi,\theta)\eta_2(\vec{x}_c[\vec{n}-\vec{n}']) \\ &\triangleq \tilde{h}_{\varphi,\theta}[\vec{n}-\vec{n}';\vec{n}_0], \end{aligned} \tag{5.67}$$

where

$$\eta_2(\vec{x}) \triangleq \eta(\vec{x}_0+\vec{x})\eta(\vec{x}_0). \tag{5.68}$$

We approximate (5.68) as follows:

$$\eta_2(\vec{x}) \approx \eta_0(\vec{x}) \triangleq \eta(\vec{x})\eta(\vec{x}_0). \tag{5.69}$$

This choice also yields a local impulse response that is symmetric in $\vec{n}$ provided the support $\eta(\vec{x})$ is symmetric itself. We focus on a symmetric $\eta(\vec{x})$, such as elliptical cylinder or sphere hereafter. The final form of the local impulse response follows from (5.65), (5.68) and (5.69):

$$h_{\mathrm{d}}[\vec{n};\vec{n}'] \approx \Pi \int_{-\frac{\pi}{2}}^{\frac{\pi}{2}} \int_0^{2\pi} w_0(\varphi,\theta)\tilde{h}_{\varphi,\theta}[\vec{n}-\vec{n}';\vec{n}_0]\,\mathrm{d}\varphi\,\mathrm{d}\theta\,. \tag{5.70}$$

Local Frequency Response of Gram Matrix

To find the DSFT $H_{\mathrm{d0}}(\vec{\omega})$ of $h_{\mathrm{d}}[\vec{n}+\vec{n}_0;\vec{n}_0]$, we need $\tilde{H}_{\varphi,\theta}(\vec{\omega})$ first, the spectrum of $\tilde{h}_{\varphi,\theta}[\vec{n};\vec{n}_0]$. Applying the linearity of the DSFT to (5.70) yields:

$$H_{\mathrm{d0}}(\vec{\omega}) = \Pi \int_{-\frac{\pi}{2}}^{\frac{\pi}{2}} \int_0^{2\pi} w_0(\varphi,\theta)\tilde{H}_{\varphi,\theta}(\vec{\omega})\,\mathrm{d}\varphi\,\mathrm{d}\theta\,. \tag{5.71}$$

Define a “tube like” function

$$s_{\varphi,\theta}(\vec{x}) \triangleq \breve{h}_0(\vec{x}\cdot\vec{e}_1, \vec{x}\cdot\vec{e}_2;\varphi,\theta)\eta_0(\vec{x}). \tag{5.72}$$

Then from (5.67) and (5.69) we have $\tilde{h}_{\varphi,\theta}[\vec{n};\vec{n}_0] = s_{\varphi,\theta}(\vec{\Delta}\odot\vec{n})$. The spectrum of $\tilde{h}_{\varphi,\theta}[\vec{n};\vec{n}_0]$ can be found as follows:

$$\begin{aligned}
\tilde{H}_{\varphi,\theta}(\vec{\omega}) &= \sum_{\vec{n}} \tilde{h}_{\varphi,\theta}[\vec{n};\vec{n}_0]\,\mathrm{e}^{-\imath(\vec{\omega}\cdot\vec{n})} \\
&= \sum_{\vec{n}} s_{\varphi,\theta}(\vec{\Delta}\odot\vec{n})\,\mathrm{e}^{-\imath(\vec{\omega}\cdot\vec{n})} \\
&\approx \frac{1}{\Delta_{\mathrm{X}}^2\Delta_{\mathrm{Z}}} \iiint s_{\varphi,\theta}(\vec{x})\,\mathrm{e}^{-\imath\frac{1}{\vec{\Delta}}\odot(\vec{\omega}\cdot\vec{x})}\,\mathrm{d}\vec{x} \\
&= \frac{1}{\Delta_{\mathrm{X}}^2\Delta_{\mathrm{Z}}} S_{\varphi,\theta}\left(\frac{1}{2\pi\vec{\Delta}}\odot\vec{\omega}\right),
\end{aligned} \tag{5.73}$$

where $s_{\varphi,\theta}(\vec{x}) \overset{\text{3D FT}}{\longleftrightarrow} S_{\varphi,\theta}(\vec{\nu})$.

Because $s_{\varphi,\theta}(\vec{x})$ is narrow in both (u, v), we approximate $\eta_0(\vec{x})$ as follows:

$$\eta_0(\vec{x}) = \eta_s\left(\frac{\vec{x}\cdot\vec{e}_3}{d_0(\varphi, \vartheta(\theta))}\right), \tag{5.74}$$

where $d_0(\varphi, \vartheta(\theta))$ is the intersecting length of the profile passing though $\vec{n}_0$ and the finite support at direction $(\varphi+\pi/2, \vartheta(\theta))$. $\eta_s(\cdot)$ denotes the image support function. We propose two choices of this support function. To be consistent with FFT-based approach, we choose

$$\eta_s\left(\frac{\vec{x}\cdot\vec{e}_3}{d_0(\varphi, \vartheta(\theta))}\right) = \mathrm{rect}\left(\frac{\vec{x}\cdot\vec{e}_3}{d_0(\varphi, \vartheta(\theta))}\right). \tag{5.75}$$

To preserve the non-negative definiteness of the *Gram Matrix*, we choose

$$\eta_s\left(\frac{\vec{x}\cdot\vec{e}_3}{d_0(\varphi, \vartheta(\theta))}\right) = \mathrm{tri}\left(\frac{\vec{x}\cdot\vec{e}_3}{d_0(\varphi, \vartheta(\theta))}\right). \tag{5.76}$$

Regardless, the local frequency response $H_0(\varrho, \Phi, \Theta)$ of the cylindrical cone-beam Gram matrix around $\vec{n}_0$ is

$$H_0(\varrho, \Phi, \Theta) \approx \Upsilon \int_{-\theta_{\max}}^{\theta_{\max}} \int_0^{2\pi} w_0(\varphi, \theta) S_{\varphi,\theta}(\varrho, \Phi, \Theta)\, \mathrm{d}\varphi\, \mathrm{d}\theta, \tag{5.77}$$

where the constant $\Upsilon \triangleq \frac{\Pi}{\Delta_{\mathrm{X}}^2 \Delta_{\mathrm{Z}}}$.

- **The 3D Fourier Transform of** $s_{\varphi,\theta}(\vec{x})$

  The 3D FT of $s_{\varphi,\theta}(\vec{x})$ can be found by the rotation property of the 3D FT. Combining (5.72) and (5.74), we have

$$s_{\varphi,\theta}(\vec{x}) = \breve{h}_0(\vec{x}\cdot\vec{e}_1, \vec{x}\cdot\vec{e}_2; \varphi, \theta)\eta_s\left(\frac{\vec{x}\cdot\vec{e}_3}{d_0(\varphi, \vartheta(\theta))}\right).$$

  Let $\vec{x}' = \mathbf{T}^{-1}\vec{x}$, where $\mathbf{T}$ is defined in (5.5) in section 5.1, whose determinant $|\mathbf{T}| = 1$. Then we have a separable function s_r that is a rotated version of $s_{\varphi,\theta}(\vec{x})$:

$$s_r(\vec{x}'; \varphi, \theta) \triangleq s_{\varphi,\theta}(\mathbf{T}\vec{x}') = \breve{h}_0(x', z'; \varphi, \theta)\eta_s\left(\frac{y'}{d_0(\varphi, \vartheta(\theta))}\right). \tag{5.78}$$

Let $s_{\varphi,\theta}(\vec{x}) \overset{\text{3D FT}}{\longleftrightarrow} S_{\varphi,\theta}(\vec{\nu})$ and $s_r(\vec{x};\varphi,\theta) \overset{\text{3D FT}}{\longleftrightarrow} S_r(\vec{\nu};\varphi,\theta)$. The spectra of $s_r(\vec{x};\varphi,\theta)$ and $s_{\varphi,\theta}(\vec{x})$ can be related through the rotation property:

$$\begin{aligned} S_{\varphi,\theta}(\vec{\nu}) &= \iiint s_{\varphi,\theta}(\vec{x}) \exp(-i2\pi\vec{\nu}\cdot\vec{x})\,\mathrm{d}\vec{x} \\ &= \iiint s_r(\vec{x}';\varphi,\theta) \exp(-i2\pi\vec{\nu}\cdot\mathbf{T}\vec{x}')\,|\mathbf{T}|\,\mathrm{d}\vec{x}' \\ &= \iiint s_r(\vec{x}';\varphi,\theta) \exp(-i2\pi(\mathbf{T}'\vec{\nu})\cdot\vec{x}')\,\mathrm{d}\vec{x}' \\ &= S_r(\mathbf{T}'\vec{\nu};\varphi,\theta). \end{aligned} \tag{5.79}$$

The 3D FT of $s_r(\vec{x};\varphi,\theta)$ is easily found from (5.78)

$$S_r(\vec{\nu};\varphi,\theta) = \left|A_0(\nu_1,\nu_3;\varphi,\theta)\right|^2 d_0(\varphi,\vartheta(\theta)) M_s(d_0(\varphi,\vartheta(\theta))\nu_2), \tag{5.80}$$

where $\eta_s(y) \overset{\text{FT}}{\longleftrightarrow} M_s(\nu_y)$ and $A_0(\nu_u,\nu_v;\varphi,\theta)$ is the 2D FT of $a_0(u,v;\varphi,\theta)$ with respect to (u,v). Therefore, the 3D FT of $s_{\varphi,\theta}(\vec{x})$ has the following form according to the rotation property in (5.79):

$$S_{\varphi,\theta}(\vec{\nu}) = \left|A_0(\vec{\nu}\cdot\vec{e}_1(\vec{\gamma}),\vec{\nu}\cdot\vec{e}_2(\vec{\gamma});\varphi,\theta)\right|^2 d_0(\varphi,\vartheta(\theta)) M_s(d_0(\varphi,\vartheta(\theta))\vec{\nu}\cdot\vec{e}_3(\vec{\gamma})). \tag{5.81}$$

The next goal is to determine $A_0(\nu_u,\nu_v;\varphi,\theta)$. We start with the 3D Fourier Slice Theorem. Let $P(\nu_u,\nu_v;\varphi,\theta)$ denote the 2D FT of $p(u,v;\vec{\gamma})$ with respect to (u,v). The 3D Fourier Slice Theorem gives the following relation:

$$P(\nu_u,\nu_v;\varphi,\theta) = F(\nu_u\vec{e}_1(\vec{\gamma}) + \nu_v\vec{e}_2(\vec{\gamma})),$$

where $F(\vec{\nu})$ is the 3D FT of the basis function $\chi(\vec{x})$. Therefore, we have the following 2D FT with respect to (u,v):

$$\frac{\Delta_{\mathrm{X}}\Delta_{\mathrm{Z}}}{c(\theta)}\, p\!\left(\frac{u}{\Delta_{\mathrm{X}}},\frac{v}{c(\theta)};\varphi,\vartheta(\theta)\right) \overset{\text{2D FT}}{\longleftrightarrow} G(\nu_u,\nu_v;\varphi,\theta),$$

where

$$\begin{aligned} G(\nu_u,\nu_v;\varphi,\theta) &= \Delta_{\mathrm{X}}^2\Delta_{\mathrm{Z}} P(\Delta_{\mathrm{X}}\nu_u, c(\theta)\nu_v;\varphi,\vartheta(\theta)) \\ &= \Delta_{\mathrm{X}}^2\Delta_{\mathrm{Z}} F(\Delta_{\mathrm{X}}\nu_u\vec{e}_1(\varphi) + c(\theta)\nu_v\vec{e}_2(\varphi,\vartheta(\theta))). \end{aligned} \tag{5.82}$$

Therefore, $A_0(\nu_u, \nu_v; \varphi, \theta)$ includes the effects of basis function and detector blur:

$$A_0(\nu_u, \nu_v; \varphi, \theta) = B_0(\nu_u, \nu_v; \varphi, \theta) G(\nu_u, \nu_v; \varphi, \theta), \tag{5.83}$$

where $B_0(\nu_u, \nu_v; \varphi, \theta)$ is the 2D FT of $b_0(u, v; \varphi, \theta)$ with respect to (u,v).

- **For "ideal" cubic voxel basis function** $\chi(\vec{x}) = \mathrm{rect}_3(\vec{x})$

  None of the projectors available to us, such as ray-driven(RD), pixel-driven(PD), NUFFT-based and distance-driven(DD) projectors has this effect. However, we use this case as demonstration. In this case, we have $F(\vec{\nu}) = \mathrm{sinc}_3(\vec{\nu})$ that leads to

$$\begin{aligned} G(\nu_u, \nu_v; \varphi, \theta) = {} & \Delta_{\mathrm{X}}^2 \Delta_{\mathrm{Z}} \, \mathrm{sinc}(\Delta_{\mathrm{X}} \nu_u \cos\varphi - c(\theta)\nu_v \sin\varphi \sin\vartheta(\theta)) \\ & \cdot \mathrm{sinc}(\Delta_{\mathrm{X}} \nu_u \sin\varphi + c(\theta)\nu_v \cos\varphi \sin\vartheta(\theta)) \\ & \cdot \mathrm{sinc}(c(\theta)\nu_v \cos\vartheta(\theta)). \end{aligned} \tag{5.84}$$

- **For square area detector**

  Consider a cylindrical support for an object with radius $R_s < D_{\mathrm{s0}}$ and a square area detector response $b(s, t) = \frac{1}{\Delta_{\mathrm{S}}} \frac{1}{\Delta_t} \mathrm{rect}\left(\frac{s}{\Delta_{\mathrm{S}}}, \frac{t}{\Delta_t}\right)$. For this case, we have

$$\begin{aligned} d_0(\varphi, \vartheta(\theta)) &= \frac{2R_s}{\cos\vartheta(\theta)} \mathrm{rect}\left(\frac{\vartheta(\theta)}{2\theta_{\mathrm{max}}}\right) \\ B_0(\nu_u, \nu_v; \varphi, \theta) &= \mathrm{sinc}\left(\frac{\Delta_{\mathrm{S}} \nu_u}{m_{s,0}(\varphi)}\right) \mathrm{sinc}\left(\frac{\Delta_t \nu_v}{m_{s,t,0}(\varphi, \theta)}\right). \end{aligned} \tag{5.85}$$

For computation efficiency, we would like to predict variances in spherical frequency space coordinates in which we can finely sample ϱ and coarsely sample (Φ, Θ). Let $S_{\varphi,\theta}(\varrho, \Phi, \Theta) \triangleq S_{\varphi,\theta}(\varrho \vec{e}_{\Phi,\Theta})$, where $A_0(\varrho, \Phi, \Theta; \varphi, \theta) \triangleq A_0(\varrho \vec{e}_{\Phi,\Theta} \cdot \vec{e}_1(\vec{\gamma}), \varrho \vec{e}_{\Phi,\Theta} \cdot \vec{e}_2(\vec{\gamma}); \varphi, \theta)$. As $\theta \to 0$ and $d_0(\varphi, \vartheta(\theta)) \to \infty$, one can show that for large ϱ, the M_s (sinc or sinc^2) term is sharply peaked at near $\varphi = \Phi \pm \pi$:

$$d_0(\varphi, \vartheta(\theta)) M_s(d_0(\varphi, \vartheta(\theta)) \vec{\nu} \cdot \vec{e}_3(\vec{\gamma})) \to \delta(\vec{\nu} \cdot \vec{e}_3(\vec{\gamma})) = \delta(\varrho \sin(\varphi - \Phi) \cos\Theta). \tag{5.86}$$

We consider the following Type-I approximation to (5.77):

$$H_0(\varrho,\Phi,\Theta) \approx \Upsilon \int_{-\theta_{\max}}^{\theta_{\max}} w_0(\Phi,\theta) \int_0^{2\pi} S_{\varphi,\theta}(\varrho,\Phi,\Theta)\,\mathrm{d}\varphi\,\mathrm{d}\theta \triangleq H_{01}(\varrho,\Phi,\Theta)\,. \tag{5.87}$$

With (5.86), the FT of $s_{\varphi,\theta}$ approaches

$$S_{\varphi,\theta}(\varrho,\Phi,\Theta) \to |A_0(\varrho\cos\Theta\cos(\varphi-\Phi),\varrho\sin\Theta;\varphi,0)|^2\,\frac{\delta(\sin(\varphi-\Phi))}{|\varrho\cos\Theta|}. \tag{5.88}$$

We consider the following further approximations to (5.77):

$$\begin{aligned} H_0(\varrho,\Phi,\Theta) &\approx \frac{\Upsilon}{|\varrho\cos\Theta|}\int_{-\theta_{\max}}^{\theta_{\max}}\int_0^{2\pi} w_0(\varphi,\theta)\,|A_0(\varrho\cos\Theta\cos(\varphi-\Phi),\varrho\sin\Theta;\varphi,0)|^2 \\ &\qquad\qquad \cdot\,\delta(\sin(\varphi-\Phi))\,\mathrm{d}\varphi\,\mathrm{d}\theta \\ &= \frac{\Upsilon}{|\varrho\cos\Theta|}\,|A_0(\varrho\cos\Theta,\varrho\sin\Theta;\Phi,0)|^2 \int_{-\theta_{\max}}^{\theta_{\max}} [w_0(\Phi,\theta)+w_0(\Phi+\pi,\theta)]\,\mathrm{d}\theta \\ &\approx \frac{2\Upsilon\theta_{\max}}{|\varrho\cos\Theta|}\,|A_0(\varrho\cos\Theta,\varrho\sin\Theta;\Phi,0)|^2\,[w_0(\Phi,0)+w_0(\Phi+\pi,0)] \\ &\triangleq H_{02}(\varrho,\Phi,\Theta), \end{aligned} \tag{5.89}$$

where the last line exploits the fact $\theta_{\max} \approx 0$ and the approximation $\int_{-\theta_{\max}}^{\theta_{\max}} f(\theta)\,\mathrm{d}\theta \approx f(0)\cdot 2\theta_{\max}$. We can see (5.89) from that the frequency response is flat along ν_3 axis, implying that the local impulse response along z-direction is much narrower than in xy-directions. This observation agrees with our empirical experience. The Type-II approximation (5.89) leads to infinite DC value, but that does not alone prevent its use for variance predictions via (5.14).

Reduced 2D Fan-beam Case

For a sanity check, we consider the DC value of local frequency response, $H_0(\varrho,\Phi,\Theta)$ in the reduced 2D fan-beam case where $n_t = 1$ and $\Delta_t \to 0$. We start with (5.87):

$$\begin{aligned} H_0(\varrho,\Phi,\Theta) &\approx \Upsilon \int_{-\frac{\Delta_t}{2D_{\mathrm{sd}}}}^{\frac{\Delta_t}{2D_{\mathrm{sd}}}} w_0(\Phi,\theta) \int_0^{2\pi} S_{\varphi,\theta}(\varrho,\Phi,\Theta)\,\mathrm{d}\varphi\,\mathrm{d}\theta \\ &\to \Upsilon\frac{\Delta_t}{D_{\mathrm{sd}}}\,w_0(\Phi,0)\,|A_0(\rho,\varrho\sin\Theta;\Phi,0)|^2\,G_0^{\mathrm{2d}}(\rho,\Phi), \end{aligned} \tag{5.90}$$

where $\rho = \varrho \cos\Theta$ and

$$G_0^{\text{2d}}(\rho, \Phi) \triangleq \int_0^{2\pi} d_0(\varphi, 0) \operatorname{sinc}^2(d_0(\varphi, 0)\, \rho \sin(\varphi - \Phi))\, \mathrm{d}\varphi\,. \tag{5.91}$$

Therefore the DC value can be derived as the following expression for $\Delta_\zeta = \Delta_{\text{z}}$:

$$H_0(0, \Phi, \Theta) \approx \frac{D_{\text{sd}}}{D_{\text{s0}}} \frac{\Delta_{\text{X}}^2}{\Delta_{\text{S}} \Delta_\beta} G_0^{\text{2d}}(0, \Phi). \tag{5.92}$$

This expression agrees with Type I DC value, $H_0(0, \Phi)$, derived in (4.64) in previous chapter.

Implementation of $H_0(\varrho, \Phi, \Theta)$

The key to calculate $H_0(\varrho, \Phi, \Theta)$ correctly is $w_0(\varphi, \theta)$ in (5.87). We first need to find the proper cone-beam coordinates corresponding to $u_0(\varphi), v_0(\varphi, \theta), \varphi$, and θ. Let $\vec{x}_0 \triangleq \vec{x}_c[\vec{n}_0]$. Using (5.35) and (5.36),

$$\begin{aligned} u_0(\varphi) &= \vec{x}_0 \cdot \vec{e}_1(\varphi) \\ v_0(\varphi, \theta) &= \vec{x}_0 \cdot \vec{e}_2(\varphi, \theta). \end{aligned}$$

We then find (s, t, β, ζ) using (5.29) – (5.32).

5.2.3 Analysis of Local Frequency Response for 3D Quadratic Regularization

For a discrete-space 3D object $\mu[\vec{n}]$, a typical quadratic roughness penalty is given as

$$R(\boldsymbol{\mu}) = \sum_{\vec{n}} \sum_{l=1}^{L} r_{l,0} \frac{1}{2} \Big((c_l \ast\!\ast\!\ast \mu)[\vec{n}] \Big)^2,$$

where $r_{l,0}$ values are design parameters that affect the directionality of the regularization and hence the shape of the PSF. Each $c_l[\vec{n}]$ is a (typically) high-pass filter. For a first-order difference:

$$c_l[\vec{n}] = \xi_l \left(\delta_3[\vec{n}] - \delta_3[\vec{n} - \vec{m}_l] \right),$$

where $\xi_l = \|\vec{m}_l\|^{-\upsilon/2}$, $\vec{m}_l$ denotes the spatial offsets to the neighboring voxels, and υ is the power of weights for diagonal neighbors that can be chosen by the user. For example, common practice chooses $\upsilon = 1$ [30, 70].

Applying Parseval's theorem, the local frequency response of $\boldsymbol{R}$ for a Λ-order (where $\Lambda \in \mathbb{N}$) difference can be found in a similar form of 2D fan-beam case in Section 4.5.2 as follows:

$$R_0(\varrho, \Phi, \Theta) = \sum_{l=1}^{L} r_{l,0} \xi_l^{2\Lambda} 4 \sin^{2\Lambda}\Big(\pi\varrho(\vec{\Delta} \odot \vec{e}_{\Phi,\Theta}) \cdot \vec{m}_l\Big). \tag{5.93}$$

In 3D geometry, $L = 13$ for the second-order neighborhood.

5.3 Simulation Results for 3D Cylindrical Cone-Beam CT

We first use a small image and sinogram to validate the local frequency responses $H_0(\varrho, \Phi, \Theta)$ and $R_0(\varrho, \Phi, \Theta)$ at image center $\vec{n}_0 = (0, 0, 0)$ for cylindrical cone-beam CT with cubic voxels (5.84). Because the FFT-based approach provides very accurate approximations to the true empirical variances, we compare analytical $H_0(\varrho, \Phi, \Theta)$ and $R_0(\varrho, \Phi, \Theta)$ with FFT-based $H_0^{(f)}(\varrho, \Phi, \Theta)$ and $R_0^{(f)}(\varrho, \Phi, \Theta)$. We also compute the normalized root mean square (NRMS) difference between analytically and FFT predicted standard deviations at image center,

$$\text{NRMS difference} \triangleq \frac{\|\text{std}_0 - \text{std}_0^{(f)}\|_2}{\|\text{std}_0^{(f)}\|_2},$$

where std_0 and $\text{std}_0^{(f)}$ are analytically and FFT predicted standard deviations, respectively.

5.3.1 Simulation Setup

We simulated a cylindrical cone-beam CT system with a cylindrical 2D detector with zero detector offsets in s and t. The corresponding sinogram size is 111 samples in s, spaced by $\Delta_{\mathrm{S}} \approx 8$ mm, 32 samples in t, spaced by $\Delta_t \approx 8.8$ mm, 137 samples in ζ, spaced by $\Delta_\zeta \approx 1.3$ mm and 123 source angular positions over 360° for each ζ. The cone angle of X-ray beam is about 26.4°.

The image is of size $64 \times 62 \times 20$ and the object is an ellipsoid. The voxel size is of 7.8 mm, 7.8 mm and 5mm. A cylindrical support is used with radius $R_s = 164.1$ mm and height 80 mm. In this case, $d_0(\varphi, \vartheta(\theta)) \approx R_s / \cos\vartheta(\theta)$ at image center. To be consistent with the FFT-based method, we implemented the rect support function (5.75). For spectrum display and calculations of variance prediction, we use $\max(H_0(\varrho, \Phi, \Theta), 0)$.

Emulating Cubic Voxel Basis Using DD Projector

In our simulation studies, 3D distance-driven (DD) projector is used. Our derivation of (5.87) and (5.89) is based on the 3D basis-expansion object model in (5.33). Furthermore, our analytical $H_0(\varrho, \Phi, \Theta)$ is calculated based on the ideal cubic voxel basis. However, none of the projectors available has the cubic voxel effect, including the DD projector. Therefore, FFT-based $H_0^{(f)}(\varrho, \Phi, \Theta)$ does not have this cubic voxel effect while analytical $H_0(\varrho, \Phi, \Theta)$ has. A basis model mismatch occurs between analytical and FFT-based results. For a fair comparison, we need to emulate the cubic voxel basis using DD projector. We can emulate this cubic voxel basis by using smaller voxels. In computing the FFT-based $H_0^{(f)}(\varrho, \Phi, \Theta)$, we first oversample the image, forward and back project the oversampled image and then downsample the resultant Gram matrix $\boldsymbol{A}'\boldsymbol{W}\boldsymbol{A}$ before taking FFTs. All of the other parameters remain unchanged.

Because of small cone angle, the DD projector approximates the cubic voxel in z-direction fairly well. Poor approximation occurs in xy-planes due to the full 360° rotation. Due to memory constraints, we only oversample the image in transaxial planes by a factor 4.

Future work should be done in finding the appropriate basis function that corresponds to the realistic projectors. Replace the cubic voxel basis by this projector-dependent basis function to eliminate the basis mismatch.

5.3.2 Local Frequency Response of Gram Matrix

We consider the simplest case, where an unweighted least-squares cost function is used in (4.2). In this case $w(s,t;\beta,\zeta) = 1$. We compute the local frequency responses of Gram matrix at image center $\vec{n}_0$, by our analytical method (5.77) and by the FFT-based method (5.11).

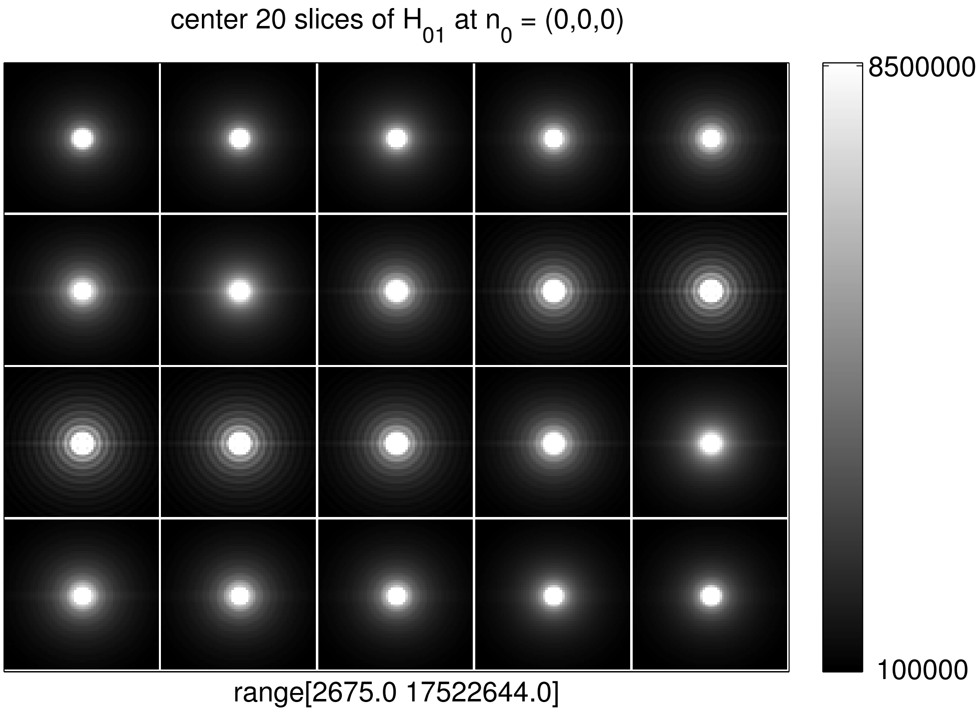

Figure 5.2: Center 20 slices of Type I local frequency response in unweighted case for $\vec{n}_0$ at image center.

Figure 5.2 and Figure 5.3 show the center 20 slices of local frequency responses of Gram matrix computed by analytical and FFT-based methods, respectively. Figure 5.4 shows the difference image $H_0(\varrho, \Phi, \Theta) - H_0^{(f)}(\varrho, \Phi, \Theta)$. Figure 5.5, Figure 5.6 and Figure 5.7 compare the profiles along three axes (ν_x, ν_y, ν_z). We can see that both the spectrum and its profiles match fairly well.

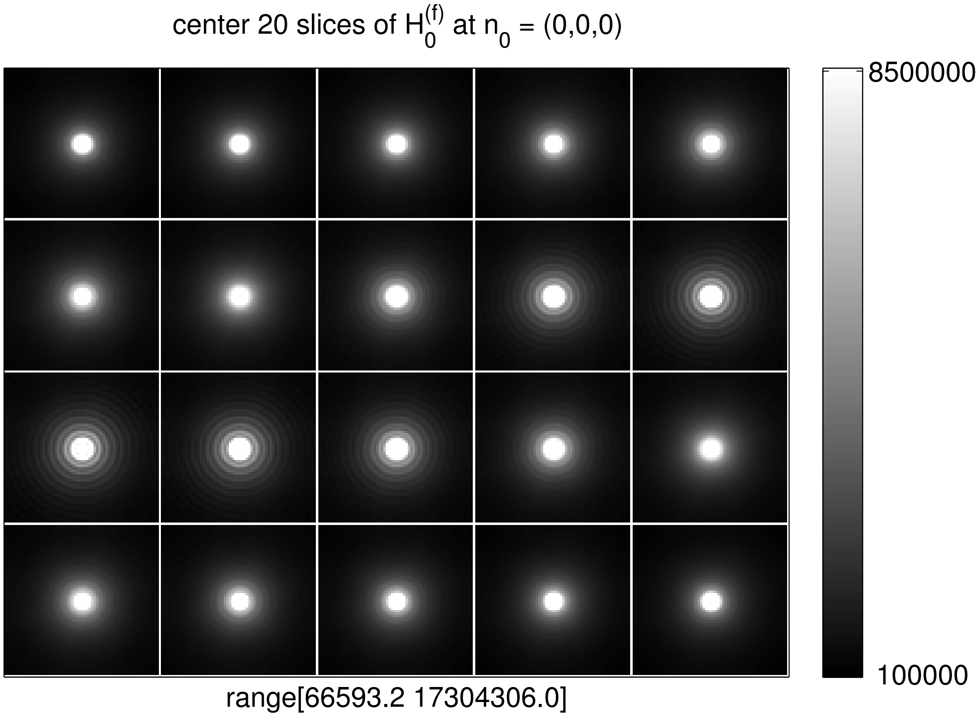

Figure 5.3: Center 20 slices of FFT-based local frequency response in unweighted case for $\vec{n}_0$ at image center.

5.3.3 Local Frequency Response of Standard Quadratic Regularization

We consider a standard quadratic penalty, where $r_{l,0}$ values are unity for all voxels in (5.93). We choose the global regularization parameter $\alpha = 2^{17.5}$ to give FWHM = 1.64 voxels, *i.e.*, 12.8 mm in transaxial plane and 1.21 voxels, *i.e.*, 6.1 mm, along axial axis at the center of the image.

Figure 5.8 shows the ν_x profiles of local frequency responses of standard quadratic regularizer calculated by analytical and FFT-based methods. We can see that the two profiles are almost identical. This result is not surprising because very few approximations are used to derive (5.93).

The NRMS difference of the predicted standard deviations for quadratically penalized unweighted least squares (QPULS) between analytical and FFT-based methods are about 5.7%.

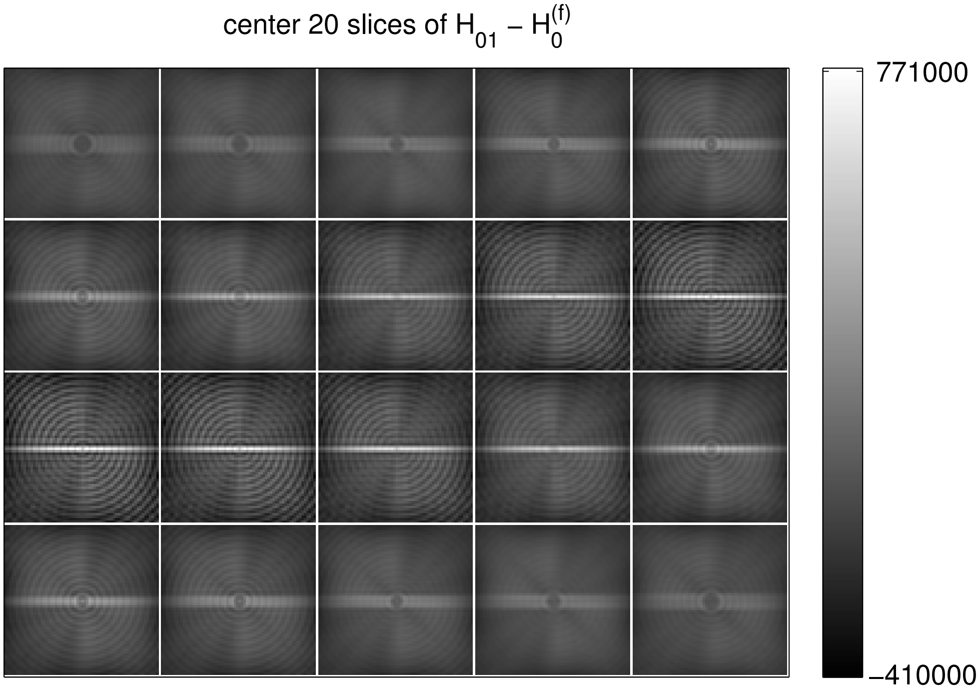

Figure 5.4: Center 20 slices of $H_{01} - H_0^{(f)}$ in unweighted case for $\vec{n}_0$ at image center for cylindrical cone-beam CT.

5.3.4 Investigations on The Effects of Basis Function Mismatch and Discretization

The simulation results in previous section show that the proposed analytical method provides accurate $H_0(\varrho, \Phi, \Theta)$ and $R_0(\varrho, \Phi, \Theta)$ at image center for a cylindrical cone-beam CT with cubic voxels. The standard deviation at image center predicted by the integrals in (5.14) is accurate compared to the FFT-predicted value.

However, cubic voxel projector is not available in practice. When operating in step-and-shoot mode, we often set the sample spacing in ζ equal to Δ_z. This sample spacing violates the assumption under (5.77) that X-ray source moves continuously in ζ direction. We next investigate the sensitivity of our proposed approach to these two effects.

The Effect of Basis Function Mismatch

To investigate the effect of the basis function mismatch, we do not use the oversampled image as proposed in Section 5.3.1 to obtain FFT-based $H_0^{(f)}(\varrho, \Phi, \Theta)$.

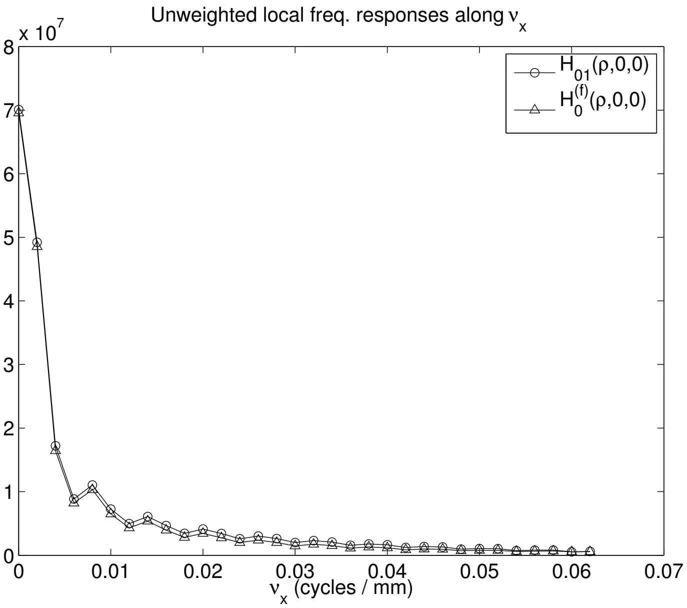

Figure 5.5: H_{01} and $H_0^{(f)}$ ν_x profiles in unweighted case for $\vec{n}_0$ at image center.

Figure 5.9 shows the difference image of analytical H_0 and the FFT-based $H_0^{(f)}$ that includes the basis model mismatch. Figure 5.10 shows their profiles along ν_z axis. Comparing Figure 5.9 and Figure 5.4, we can see that the basis function mismatch between cubic voxel and DD projector introduces larger discrepancy at $\Phi = 0°, \pm 45°$ and $\pm 135°$ directions. This phenomenon is due to the approximations that DD projector uses and likely to change with other projectors, such as ray-driven and Fourier-based projectors. The NRMS difference of the standard deviations increases to 9.5%.

The Effect of Discretization in Source Axial Trajectory ζ

Figure 5.11 shows the center 20 slices of $H_0^{(f)}$ calculated with $\Delta_\zeta = \Delta_\mathrm{z}$. The analytical local frequency response of Gram matrix (5.77) is derived based on an cylindrical cone-beam CT. The X-ray source can be placed at any point on the cylinder with radius $D_{\mathrm{s}0}$. Therefore, the assumption made under (5.77) is that X-ray source moves continuously along in ζ direction. When the sampling space in ζ is set as Δ_z, as is usual in step-and-shoot-mode, the discretization effect is fairly pronounced, as shown in Figure 5.12 and

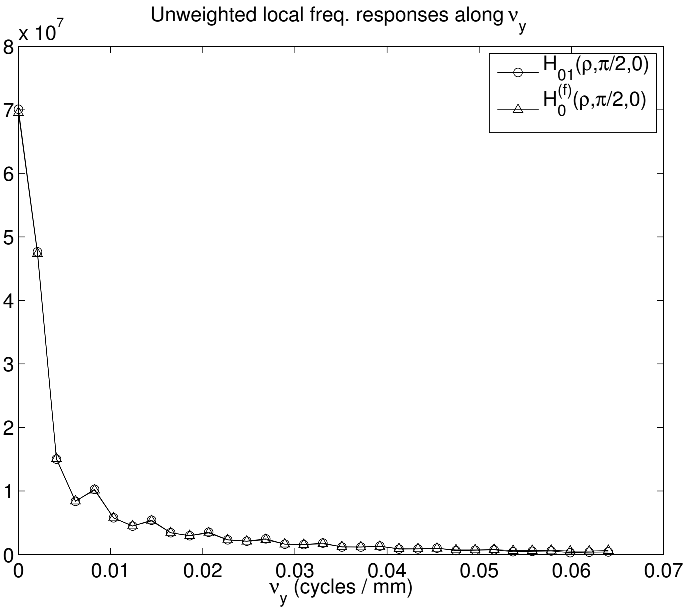

Figure 5.6: H_{01} and $H_0^{(f)}$ ν_y profiles in unweighted case for $\vec{n}_0$ at image center.

Figure 5.13. The discretization effect is mostly at high ν_z frequency components. The NRMS difference of predicted the standard deviations is about 10.3%.

5.4 Conclusion and Discussion

This chapter extends the analytical variance prediction approach to 3D cone-beam CT. The analysis is based on a "ideal" cylindrical cone-beam geometry and can be served as a starting point to the analysis in step-and-shoot or helical cone-beam CT.

The variance prediction integrals (5.14) for 3D cylindrical cone-beam CT provides an efficient approach to computing variances at many voxel locations with reasonable accuracy. However, our simulation studies in Section 5.3 show that the local frequency response of Gram matrix (5.87) can be affected by basis function mismatch and discretization in X-ray source axial positions. Basis function mismatch between cubic voxel basis and DD projector incur larger spectral discrepancy at diagonal directions. Realistic sample spacing in X-ray source axial positions incur larger spectral discrepancy at high ν_z

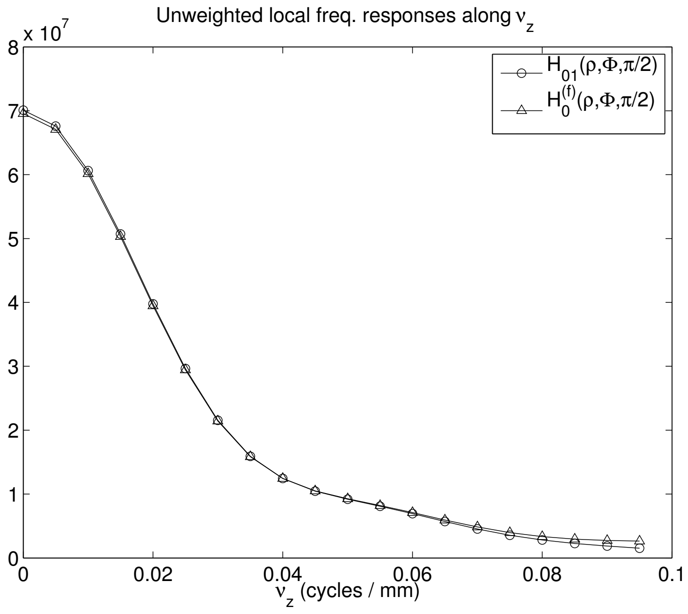

Figure 5.7: H_{01} and $H_0^{(f)}$ ν_z profiles in unweighted case for $\vec{n}_0$ at image center for cylindrical cone-beam CT.

frequency components. We found that variance prediction integrals (5.14) is most accurate for the "ideal" cylindrical cone-beam CT that is free of basis function mismatch. The NRMS difference between standard deviations is about 5.7%. It is least accurate when both voxel basis mismatch and the ζ discretization are present. The NRMS difference between standard deviations increases to about 13.2% in this case.

For helical cone-beam geometry, we conjecture that the proposed approach in this chapter can provide comparable accuracy as for cylindrical cone-beam geometry because Δ_ζ in X-ray helical trajectory is usually much smaller than Δ_{z}. For practical step-and-shoot geometry, the "semi-continuous" approach developed in Appendix A provides a potentially more accurate method. This "semi-continuous" variance prediction method keeps both t and ζ discrete. Preliminary simulation results in Appendix A show that the NRMS difference between standard deviations is about 6%.

Finally, all the simulation results are compared to FFT-based results that are not the ground truth.

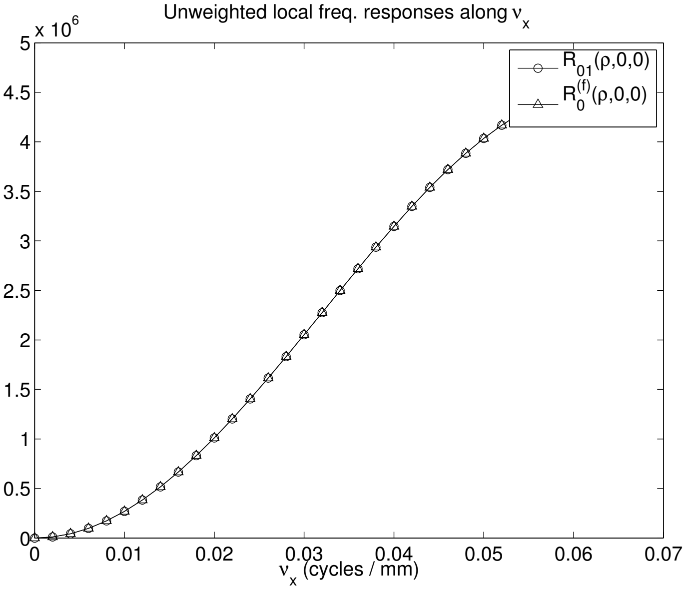

Figure 5.8: R_0 and $R_0^{(f)}$ profiles along ν_x for standard quadratic regularizer for $\vec{n}_0$ at image center.

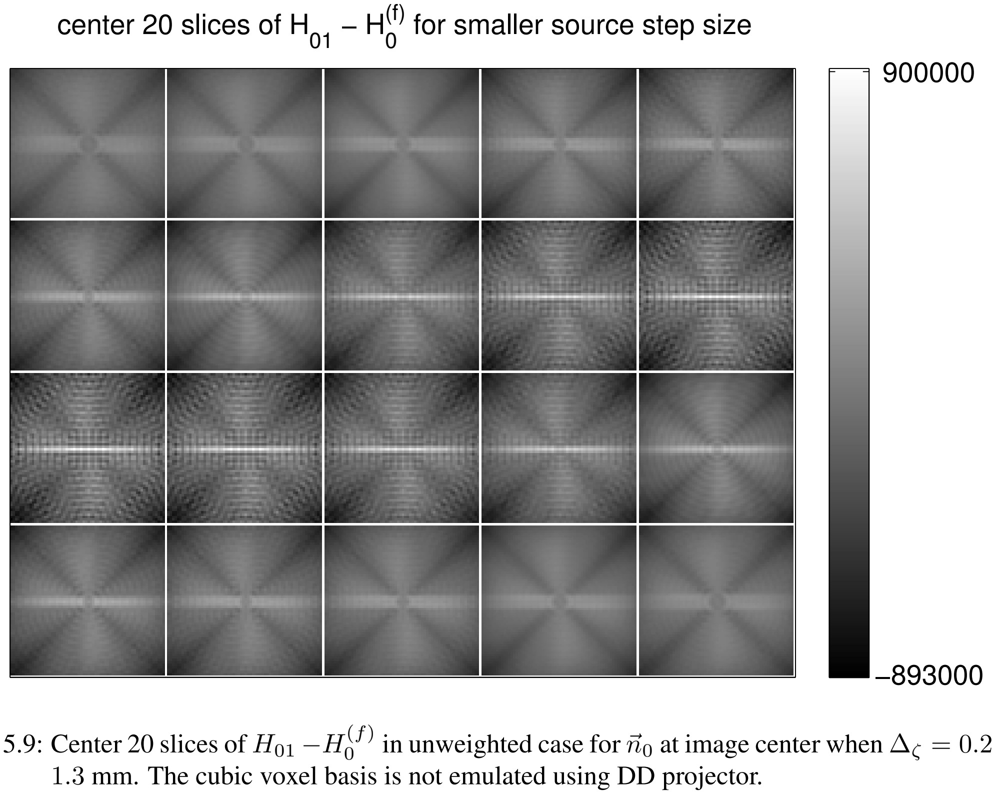

Figure 5.9: Center 20 slices of $H_{01} - H_0^{(f)}$ in unweighted case for $\vec{n}_0$ at image center when $\Delta_\zeta = 0.25\Delta_z = 1.3$ mm. The cubic voxel basis is not emulated using DD projector.

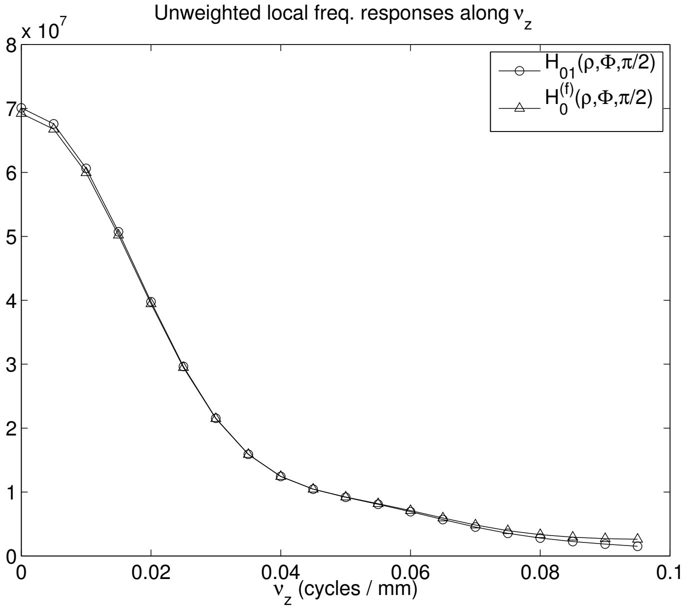

Figure 5.10: H_{01} and $H_0^{(f)}$ ν_z profiles in unweighted case for $\vec{n}_0$ at image center when $\Delta_\zeta = 0.25\Delta_z = 1.3$ mm. The cubic voxel basis is not emulated using DD projector.

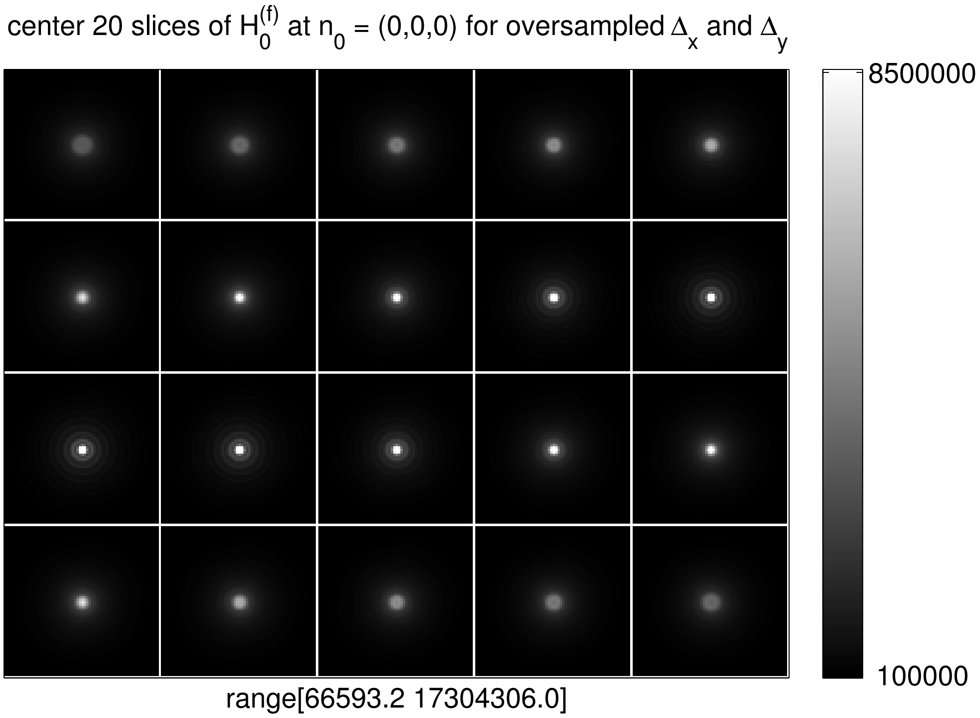

Figure 5.11: Center 20 slices of $H_0^{(f)}$ in unweighted case for $\vec{n}_0$ at image center when $\Delta_\zeta = \Delta_z$. The cubic voxel basis is emulated using DD projector.

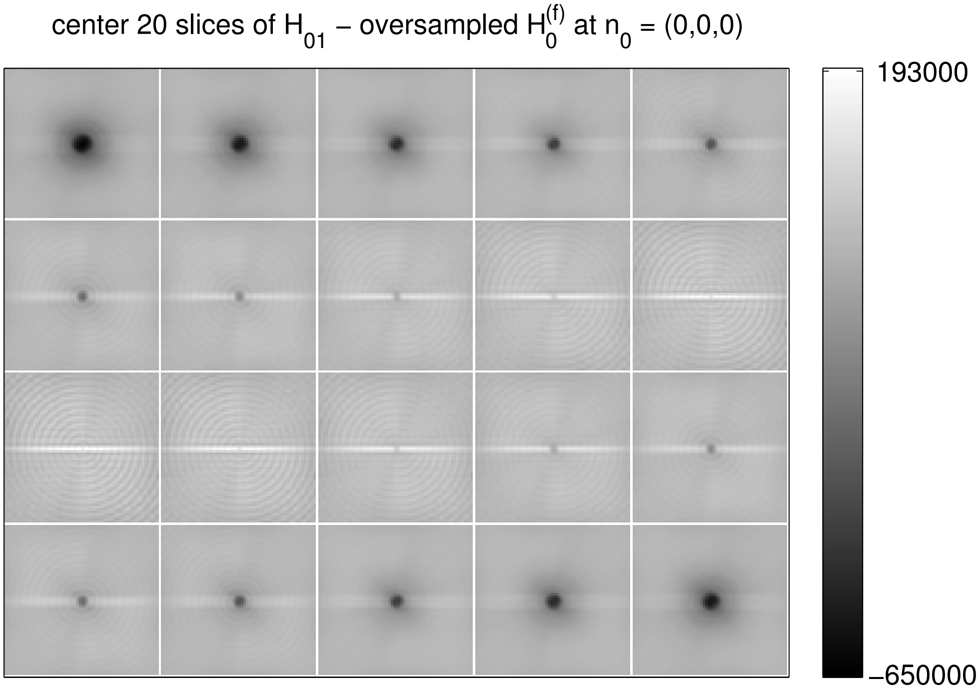

Figure 5.12: Center 20 slices of $H_{01} - H_0^{(f)}$ in unweighted case for $\vec{n}_0$ at image center when $\Delta_\zeta = \Delta_\mathrm{z}$. The cubic voxel basis is emulated using DD projector.

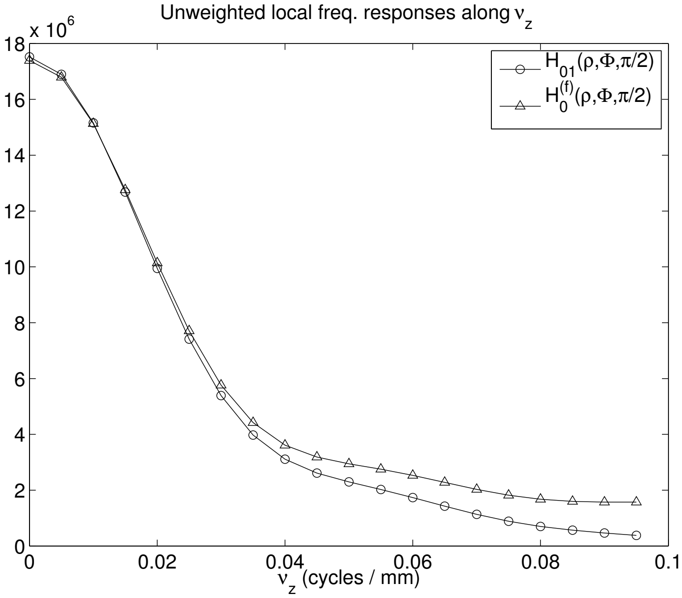

Figure 5.13: H_{01} and $H_0^{(f)}$ ν_z profiles in unweighted case for $\vec{n}_0$ at image center when $\Delta_\zeta = \Delta_\mathrm{z}$. The cubic voxel basis is emulated using DD projector.

CHAPTER 6

Summary and Future Work

6.1 Summary

The forward and back-projections are the primary computation bottleneck in X-ray CT image reconstruction. One can use conventional reconstruction methods, such as FBP by applying only back-projection once. However, conventional methods usually ignore energy-dependence of the X-ray source and cause beam-hardening errors that must be compensated for quantitatively accurate CT values. The low signal-to-noise ratio in FBP reconstructed images usually requires higher dose to patient. These disadvantages of FBP give rise to the popular research in Statistical image reconstruction methods that usually need to use iterative algorithms to minimize certain cost function. In those iterative algorithms, one forward and one back projections are needed for each iteration. Faster and more accurate forward and back-projectors are always feasible.

We developed a fast Fourier-based forward and back projectors for fan-beam transmission CT. The projectors are based on Fourier-slice theorem, the fan-to-parallel rebinning relationship and the non-uniform Fourier transform (NUFFT) that utilizes a min-max optimized Kaiser-Bessel interpolation kernel. We also incorporate the effect of shift-variant detector response in frequency domain by a simple shift-invariant detector response.

Simulation and real data results show that the NUFFT-based forward and back projectors can provide comparable accuracy as the existing approach. The computation time of forward and back-projections is equivalent to that of distance-driven (DD) projectors for modest image sizes. For larger image size, the NUFFT approach outperforms the distance-driven (DD) projectors. However this method is poorly suited for "ordered-subsets" algorithms since it must compute an oversampled 2D FFT even if only a few projection views are needed. This property limits its application to algorithms where ordered-subsets are not needed. Existing $O(N^2 \log N)$ methods also have this limitation [99].

Variance image predictions can be useful in understanding the trade-off between resolution and noise of statistical image reconstruction methods and aiding the selection of regularization parameters. Matrix-based and DFT-based prediction methods are convenient for computing variances at a few locations but is not practical when variances are needed at many or all pixels/voxels. We propose analytical variance prediction approaches that are based on local shift-invariance approximations and Parseval's theorem and derive closed-form approximations for fan-beam and cone-beam tomography.

Simulation results confirm the accuracy of these approaches. Therefore the analytical variance approximations provide a practical tool for efficiently predicting variances at large number of locations. Although not deeply investigated, we also provide an expression for computing covariances of an small region of interest (ROI) within which the local approximations are still valid. The proposed analytical variance approximations can also be extended to the cases with shift-variant detector blur where the local shift-invariance approximation is applicable, *e.g.*, for varifocal collimators in SPECT.

6.2 Future work

The work in this thesis is merely the tip of the iceberg in statistical image reconstruction research area. In this section, we propose the following suggestions for future work:

- The computation time of statistical image reconstruction becomes much longer in 3D cone-beam CT due to the larger data size. Extension of the NUFFT-based forward and back-projectors in Chapter 3 to 3D cone beam CT might provide speed acceleration for certain algorithms.
- The analytical variance prediction approaches in Chapter 5 and Appendix A are only validated for local frequency responses of unweighted Gram matrix and standard quadratic regularizer. Variances are only computed and compared for one voxel of interest at image center, using analytical and FFT-based methods. Comparison with empirical estimation results for a real systems is useful in assessing raw data noise properties.
- Chapter 5 and Appendix A developed fully-continuous and semi-continuous variance prediction approaches for ideal cylindrical cone-beam CT and step-and-shoot cone-beam CT. Generalization to axial cone-beam CT and helical cone-beam CT for quadratic PL reconstruction can be done based on the analysis in Chapter 5 and Appendix A.
- The behavior of quadratic penalty function has been investigated and understood. It has a very nice property that the Hessian matrix is independent of the object. However, it might over-smooth the fine details such as edges and small bone structures in the reconstructed image. In reality, one might prefer to use non-quadratic regularization to achieve better noise and resolution trade-off. The properties of non-quadratic regularization has not been thoroughly analyzed yet. Further research in this area will be very useful. The analysis in [5, 6] may be a useful starting point.
- The variance analysis in Chapter 4 and Chapter 5 is based on a basic Poisson statistics with mono-energetic X-ray source. Although the matrix-based approximations [32] are general for any statistical models, further investigations are needed on the effects of photon-counting detectors that collect polyenergetic X-ray photons.
- The analytical variance prediction philosophy can be also applied to predict the co-

variance matrix which is useful in many detection tasks. However, the local Fourier transform is not applied with respect to the same image location any more. Further investigation is needed to evaluate the validity of "local stationarity".

- The discussion of covariance and variance approximations in this dissertation is only focused on the second-order moments. Further analysis on bias and skewness will be helpful in understanding CT data statistics.
- The idea behind the analytical variance prediction approach is to bridge discrete and continuous frequency spaces by Discrete Space Fourier Transform (DSFT) and Parseval's theorem. In the derivation of local frequency response of Gram matrix, summations are approximated by integrals. A possible alternative is to consider the unknown image $\mu(x, y)$ to be an infinite dimensional parameter and estimate it from discrete observations [86].
- Apply variance predictions for regularization design. This is one reason that motivated us to develop analytical variance prediction approach. How to select appropriate shape parameter based on predicted noise level remains an open question.
- Study analytical variance formulas as a function of pixelization $(n_{\mathrm{p}}, \Delta_{\mathrm{x}})$ and spatial resolution to develop resolution/noise tradeoff rules. Similar results are known for FBP [62].
- Generalize analytical variance formulas to account for the non-negativity constraints. A "truncated Gaussian" model was proposed for PET in [77] to compensate for this effect and improve the accuracy in low activity area.

APPENDIX

APPENDIX A

Semi-Continuous Approach for 3D Variance Predictions

A.1 Local Impulse Response of Gram Matrix

We previously discussed a (fully) continuous variance prediction approach for 3D cylindrical cone-beam CT in Chapter 5. We proceeded by approximating the discrete summations in the elements of the *Gram matrix* (5.53) as (continuous) integrals. The NRMS difference between analytically and FFT-predicted standard deviations at image center is about 5.7% for unweighted case. However, the simulation studies in Chapter 5 also showed that the discretization in X-ray source ζ axial trajectory decreases the accuracy to 10.3%.

In this appendix, we propose a semi-continuous approach that can overcome this discretization effect and potentially provide more accurate results for step-and-shoot cone-beam CT. Instead of (5.54), we approximate (5.53) as follows:

$$\begin{aligned}\breve{h}_{\mathrm{d}}[\vec{n};\vec{n}'] \approx \Pi' \sum_{l=1}^{n_t}\sum_{j=1}^{n_\zeta} \int_{-\infty}^{\infty}\int_{-\infty}^{\infty}\int_{0}^{2\pi}\int_{-\infty}^{\infty} & w(s,t;\beta,\zeta)\,\mathrm{rect}\left(\frac{s}{2s_{\mathrm{max}}}\right)\delta(t-t_\ell) \\ & \cdot\delta(\zeta-\zeta_j)a(s,t;\beta,\zeta;\vec{n})a(s,t;\beta,\zeta;\vec{n}')\,\mathrm{d}s\,\mathrm{d}t\,\mathrm{d}\beta\,\mathrm{d}\zeta, \qquad \text{(A.1)}\end{aligned}$$

where $\Pi' \triangleq \frac{1}{\Delta_{\mathrm{S}}\Delta_\beta}$. Making change of variables from cone-beam coordinates to parallel-beam coordinates, we rewrite (A.1) as

$$\begin{aligned}\breve{h}_{\mathrm{d}}[\vec{n};\vec{n}'] \approx{} & \Pi' \sum_{l=1}^{n_t}\sum_{j=1}^{n_\zeta} \int_{-\frac{\pi}{2}}^{\frac{\pi}{2}}\int_{0}^{2\pi}\int_{-\infty}^{\infty}\int_{-\infty}^{\infty} \bar{w}(u,v;\varphi,\theta)a_p(u,v;\varphi,\theta;\vec{n})a_p(u,v;\varphi,\theta;\vec{n}') \\ & \cdot\delta(\tilde{t}(\theta)-\tilde{t}(\theta_l))\delta(\tilde{\zeta}(u,v,\theta)-\zeta_j)J(u,\theta)\,\mathrm{d}u\,\mathrm{d}v\,\mathrm{d}\varphi\,\mathrm{d}\theta, \qquad \text{(A.2)}\end{aligned}$$

where $J(u,\theta)$ is the absolute value of the determinant of the Jacobian matrix given in (5.57) and $\bar{w}(u,v;\varphi,\theta)$ is the rebinned weighting defined as follows:

$$\bar{w}(u,v;\varphi,\theta) \triangleq w(s(u),t(\theta);\beta(\varphi,u),\zeta(u,v,\theta))\,\mathrm{rect}\left(\frac{s(u)}{2s_{\mathrm{max}}}\right). \tag{A.3}$$

By using the properties of Dirac impulse and the relationship in (5.32) , we obtain the following results:

$$\begin{aligned}
\delta(\tilde{t}(\theta)-\tilde{t}(\theta_l)) &\approx \frac{\cos^2\theta_l}{D_{\mathrm{sd}}}\delta(\theta-\theta_l) \\
\delta(\tilde{\zeta}(u,v,\theta)-\zeta_j) &= |\cos\theta|\,\delta(v-\hat{v}_j(u,\theta)),
\end{aligned}$$

where

$$\hat{v}_j(u,\theta) \triangleq D_{\mathrm{s0}}\cos\tilde{\gamma}(\tilde{s}(u))\sin\theta+\zeta_j\cos\theta. \tag{A.4}$$

Therefore, we can first carry out the integrations in (A.2) with respect to θ and v as follows:

$$\begin{aligned}
\breve{h}_{\mathrm{d}}[\vec{n};\vec{n}'] \approx\ & \Pi'\sum_{l=1}^{n_t}\sum_{j=1}^{n_\zeta}\int_0^{2\pi}\int_{-\infty}^{\infty}\bar{w}(u,\hat{v}_{j,l}(u);\varphi,\theta)J_{\mathrm{2D}}(u) \\
& \cdot a_p(u,\hat{v}_{j,l}(u);\varphi,\theta;\vec{n})a_p(u,\hat{v}_{j,l}(u);\varphi,\theta;\vec{n}')\,\mathrm{d}u\,\mathrm{d}\varphi,
\end{aligned} \tag{A.5}$$

where $\hat{v}_{j,l}(u) \triangleq \hat{v}_j(u,\theta_l)$, the absolute value of 2D fan-beam Jacobian determinant $J_{\mathrm{2D}}(u) \triangleq D_{\mathrm{sd}}/\sqrt{D_{\mathrm{s0}}^2-u^2}$, and $a_p(u,\hat{v}_j(u,\theta_l);\varphi,\theta;\vec{n})$ is the rebinned cone-beam system matrix elements $a_p(u,v;\varphi,\theta;\vec{n})$ in (5.46), evaluating at $v=\hat{v}_{j,l}(u)$.

We further simplify (A.5) as follows:

$$\breve{h}_{\mathrm{d}}[\vec{n};\vec{n}'] \approx \Pi'\sum_{l=1}^{n_t}\int_0^{2\pi}\breve{w}(\varphi,\theta_l;\vec{n};\vec{n}')\breve{h}_{\varphi,\theta_l}[\vec{n};\vec{n}']\,\mathrm{d}\varphi, \tag{A.6}$$

where we define $\hat{w}(\varphi,\theta;\vec{n};\vec{n}') \triangleq \bar{w}(u,\hat{v}_{j,l}(u);\varphi,\theta)J_{\mathrm{2D}}(u)$ and

(A.7)

$$\breve{w}(\varphi,\theta;\vec{n};\vec{n}') \triangleq \frac{\sum_{j=1}^{n_\zeta}\int_{-\infty}^{\infty}\hat{w}(u,\hat{v}_{j,l}(u);\varphi,\theta)a_p(u,\hat{v}_{j,l}(u);\varphi,\theta;\vec{n})a_p(u,\hat{v}_{j,l}(u);\varphi,\theta;\vec{n}')\,\mathrm{d}u}{\sum_{j=1}^{n_\zeta}\int_{-\infty}^{\infty}a_p(u,\hat{v}_{j,l}(u);\varphi,\theta;\vec{n})a_p(u,\hat{v}_{j,l}(u);\varphi,\theta;\vec{n}')\,\mathrm{d}u}$$

$$\breve{h}_{\varphi,\theta}[\vec{n};\vec{n}'] \triangleq \sum_{j=1}^{n_\zeta} \int_{-\infty}^{\infty} a_p(u,\hat{v}_{j,l}(u);\varphi,\theta;\vec{n})a_p(u,\hat{v}_{j,l}(u);\varphi,\theta;\vec{n}')J_{\mathrm{2D}}(u)\,\mathrm{d}u\,. \tag{A.8}$$

We make further approximations to (A.7) and (A.8) by using (5.50) and assuming that $\vec{n}$ and $\vec{n}'$ are sufficiently close to $\vec{n}_0$:

$$\breve{w}(\varphi,\theta_l;\vec{n};\vec{n}') \approx J_0(\varphi)\bar{w}(u_0(\varphi),\hat{v}_{j,l}(u);\varphi,\theta_l) \triangleq w_0(\varphi,\theta_l) \tag{A.9}$$

and

$$\begin{aligned}
\breve{h}_{\varphi,\theta_l}[\vec{n};\vec{n}'] &\approx \sum_{j=1}^{n_\zeta}\int_{-\infty}^{\infty} a_0(u-u_\varphi[\vec{n}],\hat{v}_{j,l}(u)-v_{\varphi,\theta}[\vec{n}])a_0(u-u_\varphi[\vec{n}],\hat{v}_{j,l}(u)-v_{\varphi,\theta}[\vec{n}'])\,\mathrm{d}u \\
&= \sum_{j=1}^{n_\zeta} \breve{h}_0^{(j)}(\vec{\Delta}\odot(\vec{n}-\vec{n}')\cdot\vec{e}_1,\hat{v}_{j,l}(u)-v_{\varphi,\theta}[\vec{n}],\hat{v}_{j,l}(u)-v_{\varphi,\theta}[\vec{n}'];\varphi,\theta_l),
\end{aligned} \tag{A.10}$$

where the following 1D cross-correlation is w. r. t. u:

$$\breve{h}_0^{(j)}(u,v_1,v_2;\varphi,\theta) \triangleq a_0(u,v_1;\varphi,\theta)\star a_0(u,v_2;\varphi,\theta). \tag{A.11}$$

Combining all the approximations above, we have the expression for the local impulse response:

$$h_{\mathrm{d}}[\vec{n};\vec{n}'] \approx \Pi' \sum_{l=1}^{n_t}\int_0^{2\pi} w_0(\varphi,\theta_l)h_{\varphi,\theta_l}[\vec{n};\vec{n}']\,\mathrm{d}\varphi, \tag{A.12}$$

where

$$\begin{aligned}
h_{\varphi,\theta_l}[\vec{n};\vec{n}'] &\triangleq \eta(\vec{x}_c[\vec{n}])\eta(\vec{x}_c[\vec{n}']) \\
&\quad \cdot\sum_{j=1}^{n_\zeta} \breve{h}_0^{(j)}(\vec{\Delta}\odot(\vec{n}-\vec{n}')\cdot\vec{e}_1,\hat{v}_{j,l}(u)-v_{\varphi,\theta}[\vec{n}],\hat{v}_{j,l}(u)-v_{\varphi,\theta}[\vec{n}'];\varphi,\theta_l).
\end{aligned} \tag{A.13}$$

Using local shift-invariance approximation, we refer all displacements relative to the point $\vec{n}_0$ as follows:

$$\begin{aligned}
h_{\varphi,\theta_l}[\vec{n};\vec{n}'] &\approx h_{\varphi,\theta_l}[\vec{n}_0+\vec{n}-\vec{n}';\vec{n}_0]\\
&= \eta(\vec{x}_c[\vec{n}_0]+\vec{x}_c[\vec{n}-\vec{n}'])\\
&\cdot \sum_{j=1}^{n_\zeta} \breve{h}_0^{(j)}(\vec{\Delta}\odot(\vec{n}-\vec{n}')\cdot\vec{e}_1(\varphi), \hat{v}_{j,l}(u)-v_{\varphi,\theta}[\vec{n}_0+\vec{n}-\vec{n}'], \hat{v}_{j,l}(u)-v_{\varphi,\theta}[\vec{n}_0];\varphi,\theta_l)\\
&= \eta_0(\vec{x}_c[\vec{n}-\vec{n}'])\\
&\cdot \sum_{j=1}^{n_\zeta} \breve{h}_0^{(j)}(\vec{\Delta}\odot(\vec{n}-\vec{n}')\cdot\vec{e}_1(\varphi), \hat{v}_{j,l}(u)-v_{\varphi,\theta}[\vec{n}_0]-v_{\varphi,\theta}[\vec{n}-\vec{n}'], \hat{v}_{j,l}(u)-v_{\varphi,\theta}[\vec{n}_0];\varphi,\theta_l)\\
&= \eta_0(\vec{\Delta}\odot(\vec{n}-\vec{n}'))\\
&\cdot \sum_{j=1}^{n_\zeta} \breve{h}_0^{(j)}(\vec{\Delta}\odot(\vec{n}-\vec{n}')\cdot\vec{e}_1(\varphi), c_0^{j,l}(\varphi)-\vec{\Delta}\odot(\vec{n}-\vec{n}')\cdot\vec{e}_2(\varphi,\theta_l), c_0^{j,l}(\varphi);\varphi,\theta_l)\\
&\triangleq \tilde{h}_{\varphi,\theta_l}[\vec{n}-\vec{n}';\vec{n}_0],
\end{aligned}$$

where $c_0^{j,l}(\varphi) \triangleq \hat{v}_{j,l}(u) - v_{\varphi,\theta}[\vec{n}_0]$. Therefore, the local impulse response has the following nearly shift-invariant form:

$$h_{\mathrm{d}}[\vec{n};\vec{n}'] \approx \Pi' \sum_{l=1}^{n_t} \int_0^{2\pi} w_0(\varphi,\theta_l)\tilde{h}_{\varphi,\theta_l}[\vec{n}-\vec{n}';\vec{n}_0]\,\mathrm{d}\varphi\,. \tag{A.14}$$

A.2 Local Frequency Response of Gram Matrix

To find the DSFT $H_{\mathrm{d}0}(\vec{\omega})$ of $h_{\mathrm{d}}[\vec{n};\vec{n}']$, we need $H_{\varphi,\theta_l}(\vec{\omega};\vec{n}_0)$ first, the spectrum of $\tilde{h}_{\varphi,\theta_l}[\vec{n};\vec{n}_0]$, by applying the linearity of the DSFT to (5.70) yields:

$$H_{\mathrm{d}0}(\vec{\omega}) = \Pi' \sum_{l=1}^{n_t} \int_0^{2\pi} w_0(\varphi,\theta) H_{\varphi,\theta_l}(\vec{\omega};\vec{n}_0)\,\mathrm{d}\varphi\,. \tag{A.15}$$

Define a “tube like” function

$$s_{\varphi,\theta_l}(\vec{x}) \triangleq \sum_{j=1}^{n_\zeta} \breve{h}_0^{(j)}(\vec{x}\cdot\vec{e}_1(\varphi), c_0^{j,l}(\varphi)-\vec{x}\cdot\vec{e}_2(\varphi,\theta_l), c_0^{j,l}(\varphi);\varphi,\theta_l)\eta_0(\vec{x}). \tag{A.16}$$

By an analysis analogous to (5.73), we can rewrite $H_{\mathrm{d}0}(\vec{\omega})$ as follows:

$$H_{\mathrm{d}0}(\vec{\omega}) = \frac{\Pi'}{\Delta_{\mathrm{X}}^2\Delta_{\mathrm{Z}}} \sum_{l=1}^{n_t} \int_0^{2\pi} w_0(\varphi,\theta) S_{\varphi,\theta_l}\left(\frac{1}{2\pi\vec{\Delta}}\odot\vec{\omega}\right), \tag{A.17}$$

where $s_{\varphi,\theta_l}(\vec{x}) \overset{\text{3D FT}}{\longleftrightarrow} S_{\varphi,\theta_l}(\vec{\nu})$.

A.2.1 The 3D Fourier Transform of $s_{\varphi,\theta_l}(\vec{x})$

An analogous analysis as in Section 5.2.2 on the 3D Fourier transform of $s_{\varphi,\theta}(\vec{x})$ shows that the key is to find the 3D FT of $s_r(\vec{x}';\varphi,\theta_l)$, rotated version of $s_{\varphi,\theta}(\vec{x})$ that is defined as follows:

$$\begin{aligned} s_r(\vec{x}';\varphi,\theta_l) &\triangleq s_{\varphi,\theta_l}(\mathbf{T}\vec{x}') \\ &= \sum_{j=1}^{n_\zeta} \breve{h}_0^{(j)}(x', c_0^{j,l}(\varphi) - z', c_0^{j,l}(\varphi);\varphi,\theta_l)\eta_s\left(\frac{y'}{d_0(\varphi,\vartheta(\theta_l))}\right). \end{aligned} \tag{A.18}$$

The spectra of $s_r(\vec{x};\varphi,\theta_l)$ and $s_{\varphi,\theta_l}(\vec{x})$ can be related through the rotation property:

$$S_{\varphi,\theta_l}(\vec{\nu}) = S_r(\mathbf{T}'\vec{\nu};\varphi,\theta_l) \tag{A.19}$$

The 2D Fourier transform of $\breve{h}_0^{(j)}(x, c_0^{j,l}(\varphi) - z, c_0^{j,l}(\varphi);\varphi,\theta_l)$ with respect to (x,z) is given as:

$$\begin{aligned} \breve{H}_0^{(j)}(\nu_x,\nu_z) &\triangleq \int_{-\infty}^{\infty}\int_{-\infty}^{\infty} \breve{h}_0^{(j)}(x, c_0^{j,l}(\varphi) - z, c_0^{j,l}(\varphi);\varphi,\theta_l)\,\mathrm{e}^{-i2\pi\nu_x x}\,\mathrm{e}^{-i2\pi\nu_z z}\,\mathrm{d}x\,\mathrm{d}z \\ &= A_0^{(1)^*}(\nu_x, c_0^{j,l}(\varphi);\varphi,\theta_l)\int_{-\infty}^{\infty} A_0^{(1)}(\nu_x, c_0^{j,l}(\varphi) - z;\varphi,\theta_l)\,\mathrm{e}^{-i2\pi\nu_z z}\,\mathrm{d}z \\ &= A_0^{(1)^*}(\nu_x, c_0^{j,l}(\varphi);\varphi,\theta_l)\,\mathrm{e}^{-i2\pi\nu_z c_0^{j,l}(\varphi)}\,A_0(\nu_x,-\nu_z;\varphi,\theta_l), \end{aligned} \tag{A.20}$$

where $A_0(\nu_u,\nu_v;\varphi,\theta)$ is the 2D FT of $a_0(u,v;\varphi,\theta)$ with respect to (u,v) and $A_0^{(1)}(\nu_u,v;\varphi,\theta)$ is the 1D FT of $a_0(u,v;\varphi,\theta)$ with respect to u only. * denotes Hermitian conjugate. Combining (A.18), (A.20) and (A.24), we have

$$S_r(\vec{x}';\varphi,\theta_l) = A_0(\nu_x,-\nu_z;\varphi,\theta_l)\tilde{M}_s\left(\nu_y\right)\sum_{j=1}^{n_\zeta} A_0^{(1)^*}(\nu_x, c_0^{j,l}(\varphi);\varphi,\theta_l)\,\mathrm{e}^{-i2\pi\nu_z c_0^{j,l}(\varphi)}\,, \tag{A.21}$$

where $\tilde{M}_s\left(\nu_y\right)$ is the 1D FT of $\eta_s\left(\frac{y}{d_0(\varphi,\vartheta(\theta_l))}\right)$. Therefore, the 3D FT of $s_{\varphi,\theta_l}(\vec{x})$ has the following form:

$$\begin{aligned} S_{\varphi,\theta_l}(\vec{\nu}) &= A_0(\vec{\nu}\cdot\vec{e}_1(\varphi), -\vec{\nu}\cdot\vec{e}_2(\varphi,\theta_l);\varphi,\theta_l)\tilde{M}_s\left(\vec{\nu}\cdot\vec{e}_3(\varphi,\theta_l)\right) \\ &\quad\cdot\sum_{j=1}^{n_\zeta} A_0^{(1)^*}(\vec{\nu}\cdot\vec{e}_1(\varphi), c_0^{j,l}(\varphi);\varphi,\theta_l)\,\mathrm{e}^{-i2\pi c_0^{j,l}(\varphi)\vec{\nu}\cdot\vec{e}_2(\varphi,\theta_l)}\,. \end{aligned} \tag{A.22}$$

“Ideal” cubic voxel

Direct computation of $A_0^{(1)}(\nu_u, v; \varphi, \theta)$ from $a_0(u, v; \varphi, \theta)$ in (5.52) is not feasible because $g(t, \varphi)$ is generally non-separable. Therefore for ideal cubic voxel basis, we find $A_0^{(1)}(\nu_u, v; \varphi, \theta)$ by taking the 1D IFT of $A_0(\nu_u, \nu_v; \varphi, \theta)$ given in (5.83), with respect to ν_v. This leads to a sequence of convolutions:

(A.23)

$$A_0^{(1)}(\nu_u, v; \varphi, \theta) = \Delta_{\mathrm{X}}^2 \Delta_{\mathrm{Z}} \operatorname{sinc}\left(\frac{\Delta_{\mathrm{S}} \nu_u}{m_{s,0}(\varphi)}\right) \tau_1(v; \varphi, \theta) * \tau_2(v; \varphi, \theta) * \tau_3(v; \theta) * \tau_4(v; \varphi, \theta),$$

where

$$\begin{aligned}
\tau_1(v; \varphi, \theta) &= \frac{1}{c(\theta) \sin\varphi \sin\vartheta(\theta)} \, \mathrm{e}^{iv \frac{2\pi \Delta_{\mathrm{X}} \nu_u \cos\varphi}{c(\theta) \sin\varphi \sin\vartheta(\theta)}} \operatorname{rect}\left(\frac{v}{c(\theta) \sin\varphi \sin\vartheta(\theta)}\right) \\
\tau_2(v; \varphi, \theta) &= \frac{1}{c(\theta) \cos\varphi \sin\vartheta(\theta)} \, \mathrm{e}^{iv \frac{2\pi \Delta_{\mathrm{X}} \nu_u \sin\varphi}{c(\theta) \cos\varphi \sin\vartheta(\theta)}} \operatorname{rect}\left(\frac{v}{c(\theta) \cos\varphi \sin\vartheta(\theta)}\right) \\
\tau_3(v; \varphi) &= \frac{1}{c(\theta) \cos\vartheta(\theta)} \operatorname{rect}\left(\frac{v}{c(\theta) \cos\vartheta(\theta)}\right) \\
\tau_4(v; \varphi, \theta) &= \frac{m_{s,t,0}(\varphi, \theta)}{\Delta_t} \operatorname{rect}\left(\frac{m_{s,t,0}(\varphi, \theta) v}{\Delta_t}\right).
\end{aligned}$$

The convolution in (A.23) can be analytically calculated. However, we approximate it as follows. For small cone angle such that $\sin\vartheta(\theta) \approx 0$, both $\tau_1(v; \varphi, \theta)$ and $\tau_2(v; \varphi, \theta)$ tends to behave as Dirac impulses. Therefore, we approximate (A.23) as follows:

$$A_0^{(1)}(\nu_u, v; \varphi, \theta) \approx \Delta_{\mathrm{X}}^2 \Delta_{\mathrm{Z}} \operatorname{sinc}\left(\frac{\Delta_{\mathrm{S}} \nu_u}{m_{s,0}(\varphi)}\right) t_0(v; \varphi, \theta), \tag{A.24}$$

where $t_0(v; \varphi, \theta)$ is a trapezoid function shown in Figure A.1, where $w_1 = |c(\theta) \cos\vartheta(\theta)|$ and $w_2 = \frac{|m_{s,t,0}(\varphi, \theta)|}{\Delta_t}$.

A.3 Simulation Results

We tested the proposed semi-continuous approach in unweighted case by simulating the same cylindrical cone-beam systems as in Section 5.3. We compare the analytical

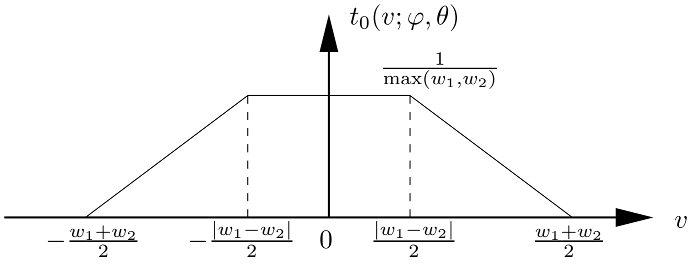

Figure A.1: Trapezoid function as the result of $\tau_3(v;\varphi) * \tau_4(v;\varphi,\theta)$, where $w_1 = |c(\theta)\cos\vartheta(\theta)|$ and $w_2 = \frac{|m_{s,t,0}(\varphi,\theta)|}{\Delta_t}$.

local frequency response of Gram matrix $H_{\text{d0}}(\vec{\omega})$ in (A.17) with (A.22) to the FFT-based $H_0^{(f)}(\vec{\omega})$ in Figure 5.11 for 3D cone-beam CT in step-and-shoot mode.

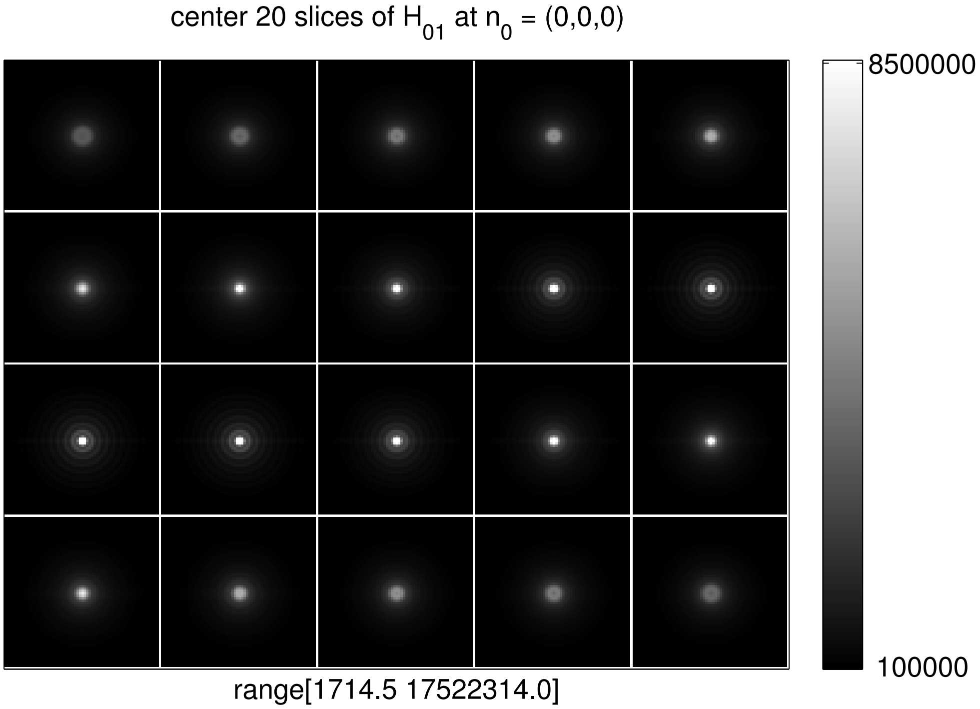

Figure A.2: Center 20 slices of local frequency response in unweighted case for $\vec{n}_0$ at image center for step-and-shoot cone-beam CT: $H_{\text{d0}}(\vec{\omega})$ is computed using semi-continuous approach.

Figure A.2 shows the center 20 slices of local frequency responses of Gram matrix computed by the semi-continuous approach. Figure A.3 shows the difference image $H_0 - H_0^{(f)}$. Figure A.4, Figure A.5 and Figure A.6 compare the profiles along three axes (ν_x, ν_y, ν_z). We can see that both the image and the profiles match fairly well. The NRMS difference of predicted the standard deviations is about 6%.

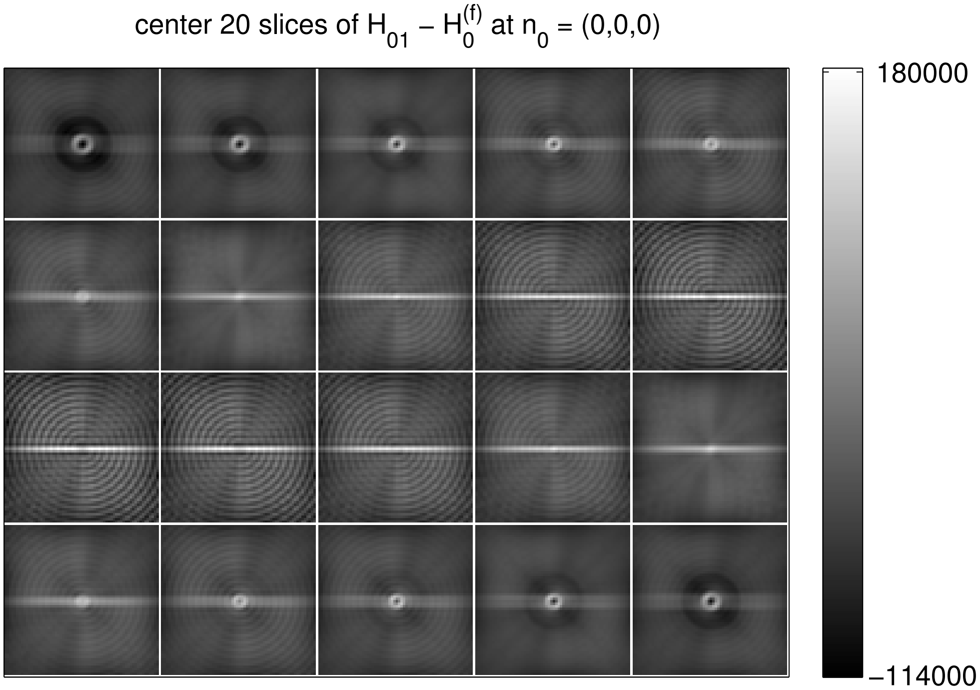

Figure A.3: Center 20 slices of $H_0 - H_0^{(f)}$ in unweighted case for $\vec{n}_0$ at image center for step-and-shoot cone-beam CT.

A.4 Discussion

This appendix proposed a semi-continuous approach to compute local frequency response of Gram matrix, $H_{\mathrm{d0}}(\vec{\omega})$ or $H_0(\boldsymbol{\rho}, \Phi, \Phi)$ for discrete ζ step size. Simulation results in Section 5.3.4 show that when discretization effect in ζ can not be ignored, the accuracy of the (fully) continuous approach proposed in Chapter 5 decreases. The NRMS difference between (fully) continuous $H_0(\boldsymbol{\rho}, \Phi, \Phi)$ and the FFT-based $H_0^{(f)}(\boldsymbol{\rho}, \Phi, \Phi)$ increases from 5.7% to 10.3%.

The semi-continuous approach is potentially more accurate than the (fully) continuous approach in the case of discrete ζ because both ζ and t remain discrete. Preliminary simulation results show that the NRMS difference between semi- continuous $H_0(\boldsymbol{\rho}, \Phi, \Phi)$ and the FFT-based $H_0^{(f)}(\boldsymbol{\rho}, \Phi, \Phi)$ is about 6%.

We conjecture that the (fully) continuous approach can provide comparable accuracy

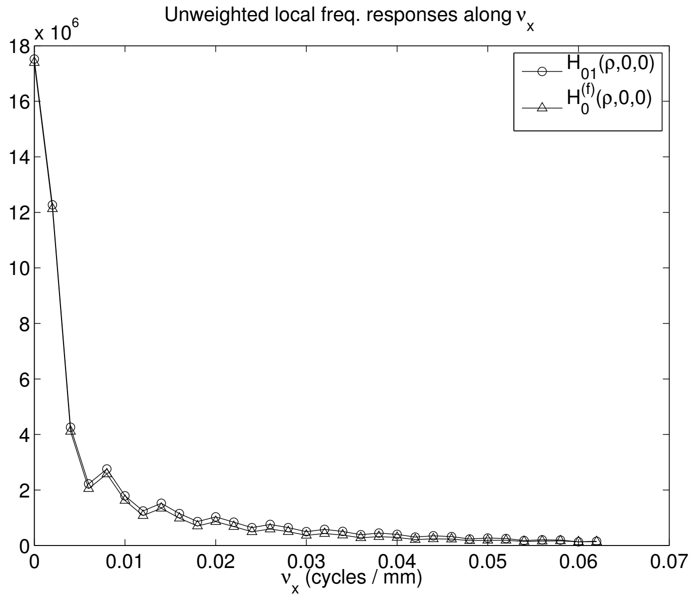

Figure A.4: H_0 and $H_0^{(f)}$ ν_x profiles in unweighted case for $\vec{n}_0$ at image center for step-and-shoot cone-beam CT.

for helical cone-beam CT as for cylindrical cone-beam CT because Δ_ζ in X-ray helical trajectory is usually much smaller than Δ_{z}.

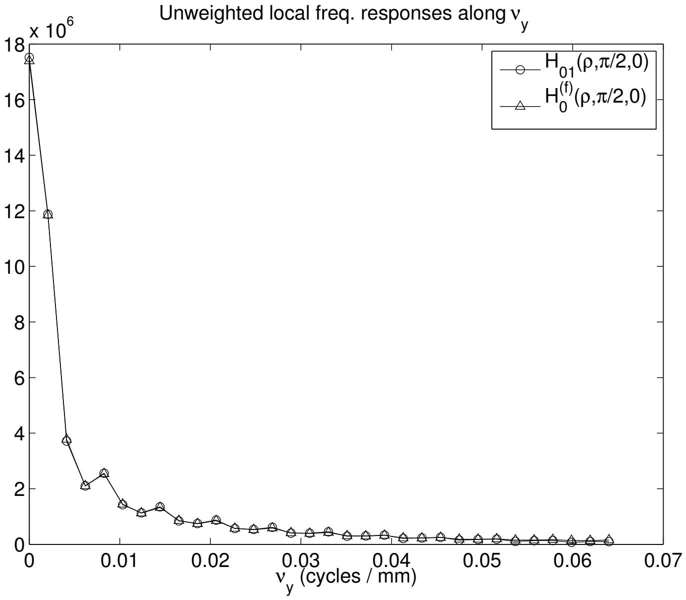

Figure A.5: H_0 and $H_0^{(f)}$ ν_y profiles in unweighted case for $\vec{n}_0$ at image center for step-and-shoot cone-beam CT.

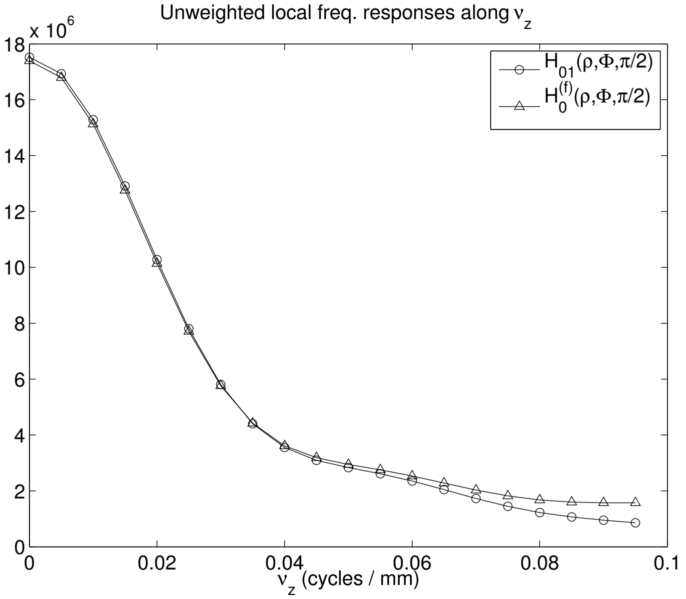

Figure A.6: H_0 and $H_0^{(f)}$ ν_z profiles in unweighted case for $\vec{n}_0$ at image center for step-and-shoot cone-beam CT.

BIBLIOGRAPHY

BIBLIOGRAPHY

[1] H. Erdoğan and J. A. Fessler. Monotonic algorithms for transmission tomography. *IEEE Trans. Med. Imag.*, 18(9):801–14, September 1999.

[2] H. Erdoğan and J. A. Fessler. Ordered subsets algorithms for transmission tomography. *Phys. Med. Biol.*, 44(11):2835–51, November 1999.

[3] M. A. Abidi and P. B. Davis. Radial noise filtering in positron emission tomography. *Optical Engineering*, 29(5):567–74, May 1990.

[4] S. Ahn, J. A. Fessler, D. Blatt, and A. O. Hero. Convergent incremental optimization transfer algorithms: Application to tomography. *IEEE Trans. Med. Imag.*, 25(3):283–96, March 2006.

[5] S. Ahn and R. M. Leahy. Spatial resolution properties of nonquadratically regularized image reconstruction for PET. In *Proc. IEEE Intl. Symp. Biomed. Imag.*, pages 287–90, 2006.

[6] S. Ahn and R. M. Leahy. Analysis of resolution and noise properties of nonquadratically regularized image reconstruction methods for PET. *IEEE Trans. Med. Imag.*, 2007. submitted.

[7] R. E. Alvarez and A. Macovski. Energy-selective reconstructions in X-ray computed tomography. *Phys. Med. Biol.*, 21(5):733–44, September 1976.

[8] James Ambrose. Computerized transverse axial scanning (tomography): Part 2. clinical application. *British Journal of Radiology*, 46:1023–1047, December 1973.

[9] A. H. Andersen. Algebraic reconstruction in CT from limited views. *IEEE Trans. Med. Imag.*, 8(1):50–5, March 1989.

[10] P. M. Anselone and P. J. Laurent. A general method for the construction of interpolating or smoothing spline-functions. *Numerische Mathematik*, 12(1):66–82, August 1968.

[11] A. Averbuch and Y. Shkolnisky. 3D Fourier based discrete Radon transform. *Applied and Computational Harmonic Analysis*, 15(1):33–69, July 2003.

[12] S. Bagchi and S. Mitra. *The nonuniform discrete Fourier transform and its applications in signal processing*. Kluwer, Boston, 1999.

[13] G. Bal and P. Moireau. Fast numerical inversion of the attenuated Radon transform with full and partial measurements. *Inverse Prob.*, 20(4):1137–1164, August 2004.

[14] H. H. Barrett and K. J. Myers. *Foundations of image science*. Wiley, New York, 2003.

[15] H. H. Barrett, D. W. Wilson, and B. M. W. Tsui. Noise properties of the EM algorithm: I. Theory. *Phys. Med. Biol.*, 39(5):833–46, May 1994.

[16] S. Basu and Y. Bresler. Error analysis and performance optimization of fast hierarchical backprojection algorithms. *IEEE Trans. Im. Proc.*, 10(7):1103–17, July 2001.

[17] P. L. Bellon and S. Lanzavecchia. Fast direct Fourier methods, based on one- and two-pass coordinate transformations, yield accurate reconstructions of x-ray CT clinical images. *Phys. Med. Biol.*, 42(3):443–64, March 1997.

[18] G. Besson. CT fan-beam parametrizations leading to shift-invariant filtering. *Inverse Prob.*, 12(6):815–33, December 1996.

[19] J. M. Boone. X-ray production, interaction, and detection in diagnostic imaging. In J. Beutel, H. L. Kundel, and R. L. Van Metter, editors, *Handbook of Medical Imaging, Volume 1. Physics and Psychophysics*, pages 1–78. SPIE, Bellingham, 2000.

[20] R. H. Chan and M. K. Ng. Conjugate gradient methods for Toeplitz systems. *SIAM Review*, 38(3):427–82, September 1996.

[21] G-H. Chen, S. Leng, and C. A. Mistretta. A novel extension of the parallel-beam projection-slice theorem to divergent fan-beam and cone-beam projections. *Med. Phys.*, 32(3):654–65, March 2005.

[22] N. H. Clinthorne. A constrained dual-energy reconstruction method for material-selective transmission tomography. *Nucl. Instr. Meth. Phys. Res. A.*, 353(1):347–8, December 1994.

[23] S. De Francesco and A. M. Ferreira da Silva. Efficient NUFFT-based direct Fourier algorithm for fan beam CT reconstruction. In *Proc. SPIE 5370, Medical Imaging 2004: Image Proc.*, pages 666–77, 2004.

[24] B. De Man and S. Basu. Distance-driven projection and backprojection in three dimensions. *Phys. Med. Biol.*, 49(11):2463–75, June 2004.

[25] A. R. De Pierro. On the relation between the ISRA and the EM algorithm for positron emission tomography. *IEEE Trans. Med. Imag.*, 12(2):328–33, June 1993.

[26] A. J. Duerinckx and A. Mackovski. Polychromatic streak artifacts in CT scanning. *J. Comp. Assisted Tomo.*, 2(4):481–7, September 1978.

[27] I. A. Elbakri and J. A. Fessler. Statistical image reconstruction for polyenergetic X-ray computed tomography. *IEEE Trans. Med. Imag.*, 21(2):89–99, February 2002.

[28] I. A. Elbakri and J. A. Fessler. Efficient and accurate likelihood for iterative image reconstruction in X-ray computed tomography. In *Proc. SPIE 5032, Medical Imaging 2003: Image Proc.*, pages 1839–50, 2003.

[29] J. A. Fessler. Tomographic reconstruction using information weighted smoothing splines. In H H Barrett and A F Gmitro, editors, *Information Processing in Medical Im.*, volume 687 of *Lecture Notes in Computer Science*, pages 372–86. Springer-Verlag, Berlin, 1993.

[30] J. A. Fessler. Penalized weighted least-squares image reconstruction for positron emission tomography. *IEEE Trans. Med. Imag.*, 13(2):290–300, June 1994.

[31] J. A. Fessler. Hybrid Poisson/polynomial objective functions for tomographic image reconstruction from transmission scans. *IEEE Trans. Im. Proc.*, 4(10):1439–50, October 1995.

[32] J. A. Fessler. Mean and variance of implicitly defined biased estimators (such as penalized maximum likelihood): Applications to tomography. *IEEE Trans. Im. Proc.*, 5(3):493–506, March 1996.

[33] J. A. Fessler. Spatial resolution properties of penalized weighted least-squares image reconstruction with model mismatch. Technical Report 308, Comm. and Sign. Proc. Lab., Dept. of EECS, Univ. of Michigan, Ann Arbor, MI, 48109-2122, March 1997. Available from `http://www.eecs.umich.edu/~fessler`.

[34] J. A. Fessler. Iterative tomographic image reconstruction using nonuniform fast Fourier transforms. Technical report, Comm. and Sign. Proc. Lab., Dept. of EECS, Univ. of Michigan, Ann Arbor, MI, 48109-2122, December 2001. Technical report available from `http://www.eecs.umich.edu/∼fessler`.

[35] J. A. Fessler. Analytical approach to regularization design for isotropic spatial resolution. In *Proc. IEEE Nuc. Sci. Symp. Med. Im. Conf.*, volume 3, pages 2022–6, 2003.

[36] J. A. Fessler. Matlab tomography toolbox, 2004. Available from `http://www.eecs.umich.edu/∼fessler`.

[37] J. A. Fessler and S. D. Booth. Conjugate-gradient preconditioning methods for shift-variant PET image reconstruction. *IEEE Trans. Im. Proc.*, 8(5):688–99, May 1999.

[38] J. A. Fessler, I. Elbakri, P. Sukovic, and N. H. Clinthorne. Maximum-likelihood dual-energy tomographic image reconstruction. In *Proc. SPIE 4684, Medical Imaging 2002: Image Proc.*, volume 1, pages 38–49, 2002.

[39] J. A. Fessler, E. P. Ficaro, N. H. Clinthorne, and K. Lange. Grouped-coordinate ascent algorithms for penalized-likelihood transmission image reconstruction. *IEEE Trans. Med. Imag.*, 16(2):166–75, April 1997.

[40] J. A. Fessler and W. L. Rogers. Spatial resolution properties of penalized-likelihood image reconstruction methods: Space-invariant tomographs. *IEEE Trans. Im. Proc.*, 5(9):1346–58, September 1996.

[41] J. A. Fessler and B. P. Sutton. A min-max approach to the multidimensional nonuniform FFT: Application to tomographic image reconstruction. In *Proc. IEEE Intl. Conf. on Image Processing*, volume 1, pages 706–9, 2001.

[42] J. A. Fessler and B. P. Sutton. Nonuniform fast Fourier transforms using min-max interpolation. *IEEE Trans. Sig. Proc.*, 51(2):560–74, February 2003.

[43] K. Fourmont. Non-equispaced fast Fourier transforms with applications to tomography. *J. Fourier Anal. and Appl.*, 9(5):431–50, September 2003.

[44] D. Fraser. Interpolation by the FFT revisited. An experimental investigation. *IEEE Trans. Acoust. Sp. Sig. Proc.*, 37(5):665–76, May 1989.

[45] J. Hsieh. *Computed tomography: Principles, design, artifacts, and recent advances*. SPIE, Bellingham, 2003.

[46] G. D. Hutchins, W. L. Rogers, P. Chiao, R. Raylman, and B. W. Murphy. Constrained least-squares projection filtering in high resolution PET and SPECT imaging. *IEEE Trans. Nuc. Sci.*, 37(2):647–51, April 1990.

[47] J. I. Jackson, C. H. Meyer, D. G. Nishimura, and A. Macovski. Selection of a convolution function for Fourier inversion using gridding. *IEEE Trans. Med. Imag.*, 10(3):473–8, September 1991.

[48] X. Jiye and O. H. Kapp. Three dimensional algebraic reconstruction from projections of multiple grey level objects. *Optik*, 72(3):87–94, 1986.

[49] P. M. Joseph and C. Ruth. A method for simultaneous correction of spectrum hardening artifacts in CT images containing both bone and iodine. *Med. Phys.*, 24(10):1629–34, October 1997.

[50] P. M. Joseph and R. D. Spital. A method for correcting bone induced artifacts in computed tomography scanners. *J. Comp. Assisted Tomo.*, 2(1):100–8, January 1978.

[51] P. M. Joseph and R. D. Spital. The exponential edge-gradient effect in x-ray computed tomography. *Phys. Med. Biol.*, 26(3):473–87, May 1981.

[52] A. C. Kak and M. Slaney. *Principles of computerized tomographic imaging*. IEEE Press, New York, 1988.

[53] P. Khurd and G. Gindi. Fast LROC analysis of Bayesian reconstructed emission tomographic images using model observers. *Phys. Med. Biol.*, 50(7):1519–32, April 2005.

[54] P. Khurd and G. Gindi. Rapid computation of LROC figures of merit using numerical observers (for SPECT/PET reconstruction). *IEEE Trans. Nuc. Sci.*, 52(3):618–26, June 2005.

[55] P. K. Khurd and G. R. Gindi. LROC model observers for emission tomographic reconstruction. In *Proc. SPIE 5372, Medical Imaging 2004: Image Perception, Observer Performance, and Technology Assessment*, pages 509–20, 2004.

[56] P. K. Kijewski and B. E. Bjarngard. Correction for beam hardening in CT. *Med. Phys.*, 5(3):209–14, May 1978.

[57] M. Knaup, M. Kachelriess, and W. A. Kalender. 3D and 4D imaging from multi-threaded cone-beam CT scans. In *Proc. IEEE Nuc. Sci. Symp. Med. Im. Conf.*, volume 4, pages 1881–5, 2005.

[58] P. J. La Riviere and X. Pan. Nonparametric regression sinogram smoothing using a roughness-penalized Poisson likelihood objective function. *IEEE Trans. Med. Imag.*, 19(8):773–86, August 2000.

[59] W. Lawton. A new polar Fourier transform for computer-aided tomography and spotlight synthetic aperture radar. *IEEE Trans. Acoust. Sp. Sig. Proc.*, 36(6):931–3, June 1988.

[60] R. M. Lewitt. Multidimensional digital image representations using generalized Kaiser-Bessel window functions. *J. Opt. Soc. Am. A*, 7(10):1834–46, October 1990.

[61] Q. Li, E. Asma, J. Qi, J. R. Bading, and R. M. Leahy. Accurate estimation of the Fisher information matrix for the PET image reconstruction problem. *IEEE Trans. Med. Imag.*, 23(9):1057–64, September 2004.

[62] A. Macovski. *Medical imaging systems*. Prentice-Hall, New Jersey, 1983.

[63] Bruno De Man, Samit Basu, Dirk Bequ, Bernhard Claus, Peter Edic, Maria Iatrou, James LeBlanc, Bob Senzig, Richard Thompson, Mark Vermilyea, Colin Wilson, Zhye Yin, and Norbert Pelc. Multi-source inverse geometry ct: a new system concept for x-ray computed tomography. In *Proc. SPIE 6510, Medical Imaging 2007: Phys. Med. Im.*, page 65100H, 2007.

[64] S. Matej, J. A. Fessler, and I. G. Kazantsev. Fourier-based forward and back-projectors for iterative image reconstruction. Technical Report MIPG303, MIPG Technical Report, University of Pennsylvania, May 2003.

[65] S. Matej, J. A. Fessler, and I. G. Kazantsev. Iterative tomographic image reconstruction using Fourier-based forward and back- projectors. *IEEE Trans. Med. Imag.*, 23(4):401–12, April 2004.

[66] S. Matej and R. M. Lewitt. Practical considerations for 3-D image reconstruction using spherically symmetric volume elements. *IEEE Trans. Med. Imag.*, 15(1):68–78, February 1996.

[67] Samuel Mazin and Norbert Pelc. Motion artifacts from an inverse-geometry ct system with multiple detector arrays. In *Proc. SPIE 6142, Medical Imaging 2006: Phys. Med. Im.*, page 61420G, 2006.

[68] O. Nalcioglu and R. Y. Lou. Post-reconstruction method for beam hardening in computerised tomography. *Phys. Med. Biol.*, 24(2):330–40, March 1979.

[69] N. Nguyen and Q. H. Liu. The regular Fourier matrices and nonuniform fast Fourier transforms. *SIAM J. Sci. Comp.*, 21(1):283–93, 1999.

[70] J. Nuyts and J. A. Fessler. A penalized-likelihood image reconstruction method for emission tomography, compared to post-smoothed maximum-likelihood with matched spatial resolution. *IEEE Trans. Med. Imag.*, 22(9):1042–52, September 2003.

[71] J. K. Older and P. C. Johns. Matrix formulation of computed tomogram reconstruction. *Phys. Med. Biol.*, 38(8):1051–64, August 1993.

[72] J. D. O'Sullivan. A fast sinc function gridding algorithm for Fourier inversion in computer tomography. *IEEE Trans. Med. Imag.*, 4(4):200–7, December 1985.

[73] H. Peng and H. Stark. Direct Fourier reconstruction in fan-beam tomography. *IEEE Trans. Med. Imag.*, 6(3):209–19, September 1987.

[74] D. Potts and G. Steidl. A new linogram algorithm for computerized tomography. *IMA J. Numer. Anal.*, 21(3):769–82, July 2001.

[75] J. Qi and R. H. Huesman. Theoretical study of lesion detectability of MAP reconstruction using computer observers. *IEEE Trans. Med. Imag.*, 20(8):815–22, August 2001.

[76] J. Qi and R. H. Huesman. Fast approach to evaluate MAP reconstruction for lesion detection and localization. In *Proc. SPIE 5372, Medical Imaging 2004: Image Perception, Observer Performance, and Technology Assessment*, pages 273–82, 2004.

[77] J. Qi and R. M. Leahy. Fast computation of the covariance of MAP reconstructions of PET images. In *Proc. SPIE 3661, Medical Imaging 1999: Image. Proc.*, pages 344–55, 1999.

[78] J. Qi and R. M. Leahy. A theoretical study of the contrast recovery and variance of MAP reconstructions from PET data. *IEEE Trans. Med. Imag.*, 18(4):293–305, April 1999.

[79] J. Qi and R. M. Leahy. Resolution and noise properties of MAP reconstruction for fully 3D PET. *IEEE Trans. Med. Imag.*, 19(5):493–506, May 2000.

[80] P. J. L. Riviere and D. M. Billmire. Reduction of noise-induced streak artifacts in X-ray computed tomography through spline-based penalized-likelihood sinogram smoothing. *IEEE Trans. Med. Imag.*, 24(1):105–11, January 2005.

[81] K. Sauer and C. Bouman. A local update strategy for iterative reconstruction from projections. *IEEE Trans. Sig. Proc.*, 41(2):534–48, February 1993.

[82] K. Sauer and B. Liu. Nonstationary filtering of transmission tomograms in high photon counting noise. *IEEE Trans. Med. Imag.*, 10(3):445–52, September 1991.

[83] T. G. Schmidt, R. Fahrig, N. J. Pelc, and E. G. Solomon. An inverse-geometry volumetric CT system with a large-area scanned source: A feasibility study. *Med. Phys.*, 31(9):2623–7, September 2004.

[84] H. Shi and J. A. Fessler. Quadratic regularization design for fan beam transmission tomography. In *Proc. SPIE 5747, Medical Imaging 2005: Image Proc.*, pages 2023–33, 2005.

[85] D. L. Snyder, C. W. Helstrom, A. D. Lanterman, M. Faisal, and R. L. White. Compensation for readout noise in CCD images. *J. Opt. Soc. Am. A*, 12(2):272–83, February 1995.

[86] Victor Solo. Transfer function estimation as an inverse problem. In *Proc. 33rd IEEE Conference on Decision and Control*, volume 4, pages 3354–58, 1994.

[87] K. Sourbelle, M. Kachelriess, and W. A. Kalender. Empirical water precorrection for cone-beam computed tomography. In *Proc. IEEE Nuc. Sci. Symp. Med. Im. Conf.*, volume 4, pages 1871–5, 2005.

[88] J. A. Stamos, N. H. Clinthorne, J. A. Fessler, and W. L. Rogers. Object and algorithm dependence of bias and variance for ART, MART, and the EM algorithm. *J. Nuc. Med. (Abs. Book)*, 32(5):986, May 1991.

[89] H. Stark and E. T. Olsen. Projection-based image restoration. *J. Opt. Soc. Am. A*, 9(11):1914–9, November 1992.

[90] J. W. Stayman and J. A. Fessler. Regularization for uniform spatial resolution properties in penalized-likelihood image reconstruction. *IEEE Trans. Med. Imag.*, 19(6):601–15, June 2000.

[91] J. W. Stayman and J. A. Fessler. Efficient calculation of resolution and covariance for fully-3D SPECT. *IEEE Trans. Med. Imag.*, 23(12):1543–56, December 2004.

[92] P. Sukovic and N. H. Clinthorne. Basis material decomposition using triple-energy X-ray computed tomography. In *IEEE Instrumentation and Measurement Technology Conference, Venice*, volume 3, pages 1615–8, 1999.

[93] P. Sukovic and N. H. Clinthorne. Penalized weighted least-squares image reconstruction for dual energy X-ray transmission tomography. *IEEE Trans. Med. Imag.*, 19(11):1075–81, November 2000.

[94] M. Unser, A. Aldroubi, and M. Eden. Recursive regularization filters: design, properties, and applications. *IEEE Trans. Patt. Anal. Mach. Int.*, 13(3):272–7, March 1991.

[95] G. Wahba. *Spline models for observational data*. SIAM CBMS-NSF, Philadelphia, 1990.

[96] J. Waldén. Analysis of the direct Fourier method for computer tomography. *IEEE Trans. Med. Imag.*, 19(3):211–22, March 2000.

[97] B. R. Whiting. Signal statistics in x-ray computed tomography. In *Proc. SPIE 4682, Medical Imaging 2002: Med. Phys.*, pages 53–60, 2002.

[98] D. W. Wilson, B. M. W. Tsui, and H. H. Barrett. Noise properties of the EM algorithm: II. Monte Carlo simulations. *Phys. Med. Biol.*, 39(5):847–72, May 1994.

[99] S. Xiao, Y. Bresler, and D. Munson. $O(N^2 \log(N))$ native fan-beam tomographic reconstruction. In *Proc. IEEE Intl. Symp. Biomed. Imag.*, pages 824–7, 2002.

[100] T. Yamaya, T. Obi, M. Yamaguchi, K. Kita, N. Ohyama, and H. Murayama. Algebraic PET image reconstruction with pre-computed reconstruction operators using subsets of sensitivity functions. *IEEE Trans. Nuc. Sci.*, 47(4-2):1670–5, August 2000.

[101] C. H. Yan, R. T. Whalen, G. S. Beaupré, S. Y. Yen, and S. Napel. Reconstruction algorithm for polychromatic CT imaging: Application to beam hardening correction. *IEEE Trans. Med. Imag.*, 19(1):1–11, January 2000.

[102] M. Yavuz and J. A. Fessler. Penalized-likelihood estimators and noise analysis for randoms-precorrected PET transmission scans. *IEEE Trans. Med. Imag.*, 18(8):665–74, August 1999.

[103] A. Yendiki and J. A. Fessler. Analysis of unknown-location signal detectability for regularized tomographic image reconstruction. In *Proc. IEEE Intl. Symp. Biomed. Imag.*, pages 279–83, 2006.

[104] Y. Zhang and J. A. Fessler. Fourier-based forward and back-projectors in iterative fan-beam tomographic image reconstruction. In *Proc. IEEE Intl. Symp. Biomed. Imag.*, pages 364–7, 2004.

[105] Y. Zhang, J. A. Fessler, and J. Hsieh. Fast variance image predictions for quadratically regularized statistical image reconstruction in fan-beam tomography. In *Proc. IEEE Nuc. Sci. Symp. Med. Im. Conf.*, volume 4, pages 1929–33, 2005.

[106] Y. Zhang-O'Connor and J. A. Fessler. Fourier-based forward and back-projectors in iterative fan-beam tomographic image reconstruction. *IEEE Trans. Med. Imag.*, 25(5):582–9, May 2006.

[107] Y. Zhang-O'Connor and J. A. Fessler. Fast predictions of variance images for fan-beam transmission tomography with quadratic regularization. *IEEE Trans. Med. Imag.*, 26(3):335–46, March 2007.

[108] Y. Zhang-O'Connor and J. A. Fessler. Fast variance predictions for 3D cone-beam CT with quadratic regularization. In *Proc. SPIE 6510, Medical Imaging 2007: Phys. Med. Im.*, page 65105W, 2007.